UNIVERSIDAD NACIONAL DEL LITORAL

On the Rozovskii method to isolate secondary circulation from skewed flow

Mariana Inés Morell

FICH
FACULTAD DE INGENIERIA
Y CIENCIAS HIDRICAS

INTEC
INSTITUTO DE DESARROLLO TECNOLOGICO
PARA LA INDUSTRIA QUIMICA

Tesis de Doctorado **2015**

UNIVERSIDAD NACIONAL DEL LITORAL

Facultad de Ingeniería y Ciencias Hídricas

Instituto de Desarrollo Tecnológico para la Industria Química

On the Rozovskii method to isolate secondary circulation from skewed flow

Mariana Inés Morell

Tesis remitida al Comité Académico del Doctorado
como parte de los requisitos para la obtención
del grado de
DOCTOR EN INGENIERIA
Mención Recursos Hídricos
de la
UNIVERSIDAD NACIONAL DEL LITORAL

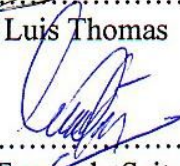## 2015

Santa Fe, 24 de noviembre de 2015.

Como miembros del Jurado Evaluador de la Tesis de Doctorado en Ingeniería titulada *"On the Rozovskii method to isolate secondary circulation from skewed flow"*, desarrollada por la Ing. Mariana Inés MORELL en el marco de la Mención "Recursos Hídricos", certificamos que hemos evaluado la Tesis y recomendamos que sea aceptada como parte de los requisitos para la obtención del título de Doctor en Ingeniería.

La aprobación final de esta disertación estará condicionada a la presentación de dos copias encuadernadas de la versión final de la Tesis ante el Comité Académico del Doctorado en Ingeniería.

Dr. Gerardo Perillo   (x)

Dr. Luis Thomas
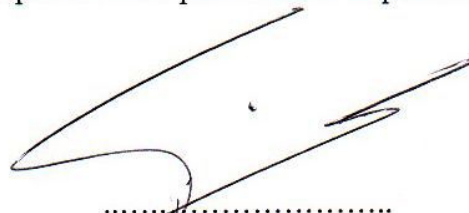
Dr. Carlos Marcelo García

Dr. Fernando Saita

Santa Fe, 24 de noviembre de 2015.

Certifico haber leído la Tesis, preparada bajo mi dirección en el marco de la Mención "Recursos Hídricos" y recomiendo que sea aceptada como parte de los requisitos para la obtención del título de Doctor en Ingeniería.

Dr. Carlos Vionnet
Director de Tesis

(x) Firma el Secretario de Posgrado por el Dr. Perillo, quien participó mediante videoconferencia

Abstract

Captured 2DV patterns (bidimensional vertical) of river flow velocities in a cross-plane provide the basis for inferring the existence of helical flow in open-channel bends and stream confluences as well. Researchers usually refer to the procedure named after Rozovskii, which computes the cross-stream component with respect to the mean flow direction at each vertical, forcing by definition a zero net discharge in outward and inward directions. As a consequence, the secondary flow strength is determined locally by each vertical velocity profile instead of defining it on the entire cross-section. Nevertheless, some ambiguities still arise when deciding the orientation of the cross-channel plane that defines the downstream and the cross-stream component.

Rhoads and Kenworthy (1998a) assumed that part of the method shortcomings could be circumvented by projecting their field data onto fixed cross-sections. However, their contribution ignited a controversy that continues to the present days. For that reason, the questioning of the Rozovskii method is of substantial interest.

It is, therefore, the purpose of this thesis to contribute to the elucidation of the controversy from both analytical and experimental points of view. Two rather simple analytical flow solutions that exhibits helical behavior were developed without any attempt to capture the precise complex flow-pattern that set in curved open-channels. They should be considered as semi-heuristic models built from past and probed descriptions of the process. Then, massive field works were undertaken at river bends nearby the Santa Fe city to test the previous theoretical findings.

The author establishes that despite the apparent capability of the Rozovskii procedure to extract the helicoidal component, the cross-flow has distortion by an error source term entirely attributed to the streamwise velocity. Thus, even though the Rozosvskii method delivers crosswise-looking velocity distributions, the profile indeed blends the sought secondary flow component with the unwanted streamwise velocity component. Despite these disadvantages, the method can identify secondary currents if any, at extremely low cost (in terms of the computing power required) and within the order of magnitude of the actual phenomena.

Finally, the thesis closes by proposing an engineering intervention downstream of the studied bifurcation at the entrance channel to the Santa Fe city harbor. It is possible to set up a self-dredging flow reversal along the access channel, turning the actual diffluence of the studied node into a stable confluence.

Resumen Extendido

Introducción

En las últimas décadas han surgido numerosas investigaciones en curvas de canales abiertos con la esperanza de descubrir parte de los mecanismos responsables de la generación de meandros en cauces aluviales (Figura 1). No obstante, la forma en planta continuamente cambiante y la variabilidad topográfica del lecho hacen que la hidrodinámica de un flujo natural meandriforme sea sumamente compleja (Blanckaert et al., 2009). El campo de flujo es fuertemente tridimensional (3D), y en cada sección transversal del meandro se desarrolla un flujo cruzado o secundario.

Por tanto, el flujo base en una curva de río resulta de superponer dos componentes fácilmente identificables: uno longitudinal debido al transporte neto de la masa de agua y otro transversal debido al desbalance mecánico que se establece entre el gradiente lateral de presión hidrostática y la aceleración centrífuga inducida por la curvatura del canal. La acción combinada de ambos da lugar a las conocidas corrientes helicoidales en flujos curvos a cielo abierto (Figura 2), las que modifican los patrones de erosión y transporte de sedimentos y con ello, la evolución morfológica de la sección transversal a escala local (Engelund, 1974).
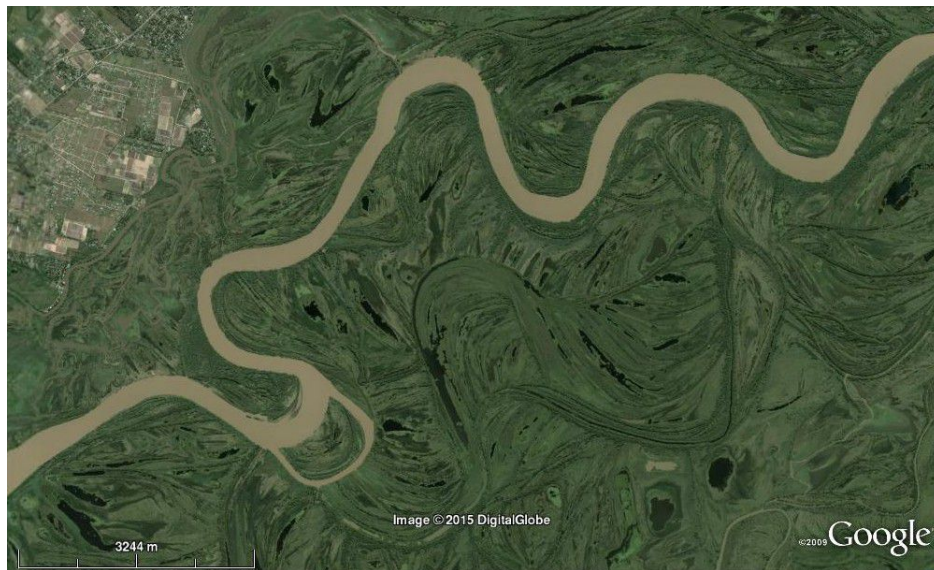

FIGURE 1: Meandros del Río Colastiné, en la planicie aluvial del Río Paraná en las cercanías de la ciudad de Santa Fe, Argentina

Paralelamente, en los últimos años hubo progresos significativos en la tecnología disponible para medir el flujo a cielo abierto en canales y cauces naturales. Es así que hoy se cuenta con la posibilidad de medir con extrema precisión las 4 incógnitas básicas de la hidrodinámica a superficie libre, esto es (h, u, v, w), tanto en el espacio como en el tiempo (en este último caso, si es posible ignorar las complejidades propias de la turbulencia,

invocando por ejemplo la hipótesis de flujos poco profundos (Carrasco and Vionnet, 2004)). Aquí h representa la profundidad local del agua, y (u, v, w) los componentes de la velocidad del flujo con respecto a un sistema de referencia cartesiano (x, y, z) supuestamente inercial, usualmente definido en la pared del canal en un laboratorio o la margen del río en campo.

La precisión espacial en el muestreo de las variables mencionadas se obtiene al combinar un posicionador satelital con corrección diferencial trabajando en modo cinemático (dGPS RTK) con perfiladores acústicos basados en el principio Doppler (ADCP - acoustic Doppler current profiler). El trabajo en "simultáneo" de estos equipos permite disponer entonces de series de valores de las incógnitas hidrodinámicas promediadas en un intervalo de tiempo dado (lo que filtra ciertos efectos turbulentos en el sentido de Reynolds) y a lo largo, ancho y profundidad de un cierto volumen o "tramo" de río. Sin embargo, la escasa disponibilidad de software específico para procesar los datos de ADCPs complica sobremanera la posibilidad de aislar en forma apropiada las corrientes secundarias (Muste et al., 2004; Parsons et al., 2013).

Más aún, últimamente se desató una agria disputa en la comunidad científica sobre aspectos técnicos vinculados a la medición experimental de las corrientes secundarias. Esta controversia involucra desacuerdos sobre la presencia o ausencia de corrientes secundarias en una curva de un río, y sobre el método utilizado para procesar las mediciones y su capacidad para aislar el flujo cruzado (Lane et al., 1999; Rhoads and Kenworthy, 1999; Lane et al., 2000; Rhoads and Sukhodolov, 2001; Richardson and Thorne, 2001; Parsons et al., 2007; Szupiany et al., 2009; Parsons et al., 2013). Uno de los métodos más populares, y objeto de la controversia, es el llamado descomposición de Rozovskii (1957). Este método calcula la componente del flujo cruzado en relación al flujo promedio de cada vertical o perfil medido.

Es justamente esa forma de proyectar -o aislar- las corrientes secundarias lo que la presente tesis pretendió discutir, dilucidando de una vez y en forma concluyente la mencionada controversia. Como resultado, el cuerpo principal de la Tesis se organizó en tres Capítulos independientes, aunque estrechamente vinculados entre sí. Con la excepción del Capítulo 1 (estado del arte), y del 5 y 6 (conclusiones y material suplementario, respectivamente), los Capítulos 2, 3, y 4 pretenden ser autocontenidos y susceptibles de constituir cada uno *per se* una potencial publicación en una revista internacional de la especialidad. En consencuencia, parte del material de un Capítulo está repetido en otro al solo efecto de garantizar la autocontención del material presentado.

El Capítulo 2 revisa y critica el método de Rozosvskii sobre la base de dos modelos teóricos de flujo helicoidal, uno el conocido modelo de Engelund (1974) y otro desarrollado específicamente durante esta Tesis. El Capítulo 3 hace lo propio pero con

datos de campo -en lugar de teóricos- para lo cual se desarrolló un código para procesar información captada por ADCPs. Finalmente, el Capítulo 4 (el más ingenieril de todos) intenta comparar dicha información de campo, procesada con códigos de distinta procedencia, con resultados generados por la herramienta numérica Telemac-3d (Telemac-Mascaret Modelling System, 2014).
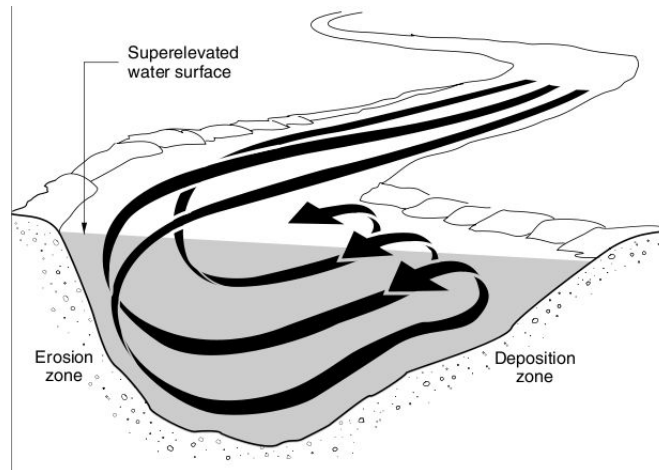

FIGURE 2: Corrientes helicoidales en una curva de un cauce aluvial

Hipótesis

A partir de los desacuerdos y controversias planteadas en base al método de Rozovskii, se asumé como hipótesis de la tesis la premisa que el método postulado por Rozovskii, utilizado para extraer la componente lateral de un flujo helicoidal asimétrico de datos de campo, presenta un sesgo intrínsecamente erróneo que afecta su resultado. En otras palabras, se asume que las corrientes secundarias computadas con Rozovskii contienen un error intrínseco.

Objetivos

Entonces, en función de la hipótesis, se fija como objetivo último de la tesis analizar el tratamiento de las observaciones de campo captadas con ADCP con el fin de aislar la circulación secundaria de la componente primaria de flujos curvos. Para ello primeramente se analizó exhaustivamente el método de Rozovskii con datos sintéticos generados con modelos teóricos, luego se procesaron datos de campo filtrados sobre la base de la crítica previa, y finalmente se llevó a cabo una comparación cualitativa con resultados numéricos producidos por un código 3D reconocido. En resumen, la tesis buscó satisfacer tres objetivos diferenciados, y agrupados en tres capítulos relacionados:

i Analizar críticamente el procedimiento de Rozosvskii para aislar la circulación secundaria de un flujo primario curvo desde un aspecto teórico(Cap. 2),

ii Verificar las predicciones teóricas con datos experimentales e implementar un método de proyección alternativo para el tratamiento de los datos de campo (Cap. 3),

iii Caracterizar el patrón del flujo en una difluencia de un río del sistema aluvial del Paraná mediante una comparación entre datos de campo y simulaciones numéricas (Cap. 4).

Metodología y Resultados

El Capítulo 2 presenta una revisión crítica del popular método de Rozosvskii, el cual es ampliamente utilizado por científicos y profesionales para la obtención de datos de circulación secundaria de flujos medidos en campo o en laboratorios (Bathurst et al. (1977); Dietrich and Smith (1983); Szupiany et al. (2009); Parsons et al. (2013)).

El procedimiento de Rozovskii (1957), reintroducido por Bathurst et al. (1977), supuestamente proporciona un criterio para determinar si las celdas de circulación secundaria pueden estar presentes a lo largo de una trayectoria de flujo curvo mediante el cálculo de una secuencia de planos discretos, y orientados perpendicularmente a la dirección local de la velocidad media en la vertical (Dietrich and Smith, 1983). Sin embargo, la celda de recirculación transversal no está necesariamente orientada en la perpendicular a la dirección del vector medio en cada plano del perfil vertical.

Para el análisis del método de Rozovskii se recurrió entonces a dos modelos teóricos simplificados que producen corrientes secundarias: la clásica solución de Engelund (1974), modificada para admitir una deriva lateral, y un modelo de flujo potencial motorizado por una capa de vórtices (*vortex sheet*) a partir de una aproximación conocida en teoría de lubricación (Vionnet, 1995). Las soluciones exactas fueron empleadas para la generación de datos sintéticos, y a la usanza de los datos de campo tal como son capturados con un ADCP.

El procedimiento adoptado posibilitó identificar el error sistemático introducido por el método de Rozovskii, el cual ha sido ignorado hasta el presente en la literatura especializada. Se establece entonces que una aplicación directa del método de Rozosvskii puede enmascarar la correcta magnitud de las estructuras de circulación secundarias tanto en curvas como en confluencias.

El Capítulo 3 incluye una detallada descripción de los datos de campo capturados durante el desarrollo de la Tesis. Se realizaron mediciones en dos sitios diferentes sobre el Río Colastiné; en el tramo exterior del Canal de Acceso al puerto de Santa Fe, donde si bien el río presenta una bifurcación en forma de Y, su hidrodinámica responde a un flujo curvo a superficie libre (Morell et al., 2014), y en una confluencia ubicada a pocos cientos de metros aguas arriba. Las mediciones no sólo incluyeron determinaciones precisas de la topografía del lecho sino también de las estructuras 3D del campo de velocidades.

Se propuso en consecuencia un procedimiento de proyección alternativo a Rozovskii, basado en eliminar la deriva lateral del campo de velocidades en cada vertical, y proyectar el campo resultante sobre una trayectoria media recorrida por la embarcación. Esta última se obtiene a través de un ajuste ortogonal por mínimos cuadrados. A diferencia de Rozosvskii, que es un método de proyección estrictamente local (el ángulo de proyección depende de los valores del flujo en cada vertical), el aquí presentado se basa en coordenadas geográficas o globales (*ENU: East-North-Up*).

La metodología adoptada involucra dos pasos: primeramente se exportan los datos de campo en archivos de formato ASCII con los programas provistos por el fabricante del ADCP (Sontek y TRDI), y posteriormente se filtran con un paquete de software escrito en fortran 95, llamado *read-aDcp* para su posterior procesamiento y visualización. El procedimiento *after-read-aDcp* permite a los usuarios integrar las velocidades primaria y secundaria de una o más secciones transversales con el modelo digital del terreno, generado previamente con las rutinas descritas en Vionnet (2010).

El procedimiento *read-aDcp* proyecta los datos de velocidad 3D con una metodología similar a la utilizada por Dinehart and Burau (2005). Las corrientes secundarias se calculan con (o sin) la condición de caudal neto nulo del flujo trasversal. El código descompone tanto el campo de velocidades 2D-horizontal (2DH), promediado en la vertical, como los componentes de velocidades tangenciales (a lo largo del plano trasversal al flujo) y normales (a lo largo del plano definido por la dirección del flujo principal), con la adición del componente vertical (*Up*) para el caso 3D. Los componentes tangenciales y verticales definen el plano 2D-vertical (2DV), representando el campo de velocidades a lo largo del plano transversal proyectado, y ubicado a través de un ajuste de mínimos cuadrados ortogonales de todas las trayectorias navegadas.

El procedimiento seguido se aplicó tanto a datos obtenidos con ADCPs de distintos fabricantes (Sontek y TRDI) como a datos capturados en diferentes ocasiones. En todos los casos se detectaron corrientes secundarias de estructura casi idéntica. Esto habla, en principio, de la independencia de los resultados respecto del dispositivo utilizado, de su posterior tratamiento, y de la estabilidad o "persistencia" de las corrientes secundarias desde el punto de vista hidrodinámico. Y por último, el análisis realizado a los datos de campo confirman las predicciones teóricas realizadas en el Capítulo 2. La proyección de Rozovskii definitivamente enmascara la correcta magnitud de las corrientes secundarias con un error proporcional al déficit (o exceso) de la componente longitudinal de velocidad con respecto a su valor medio.

Finalmente, el Capítulo 4, el único publicado hasta el presente (Morell et al., 2014), compara el flujo secundario tal como fuera relevado en la zona de estudio, y aislado acorde a los procedimientos del Capítulo 3, con simulaciones numéricas producidas por

Telemac-3D. La zona de estudio presenta una rama donde el flujo entrante experimenta un giro agudo que lo hace propenso a efectos inerciales de las fuerzas centrífugas. En rigor, los resultados numéricos confirman que ambas ramas de la difluencia actúan como verdaderas curvas de un cauce aluvial, y por tanto, son propensas a acomodar corrientes secundarias (Dargahi, 2004). Todas las características observadas en campo son capturadas por las soluciones numéricas 2D y 3D: flujo helicoidal, zonas de separación, y formación de un vórtice de eje vertical, incluyendo la deflección de la superficie libre observada a lo largo del llamado "tramo exterior" del canal de acceso al Puerto de Santa Fe.

Podría decirse que al Capítulo 4 le faltó el desarrollo de un algoritmo unificado para aislar el flujo transversal de flujos curvos tanto de datos de campo como de resultados numéricos (el algoritmo debe ser independiente de la procedencia o génesis del dato, más allá del formato propio de cada uno). En este caso, la interface de pre- y post-procesamiento de Telemac-3d no fue de ayuda.

Conclusiones

La captura de celdas de recirculación, a partir de patrones de velocidades 2DV en un plano que representa una determinada sección transversal de un cauce aluvial, proporciona la base para inferir la existencia de un flujo helicoidal tanto en tramos curvos como en confluencias. Sin embargo, ciertas ambigüedades persisten a la hora de decidir la orientación del plano medio transversal que define las componentes en sentido de la corriente y la transversal (Lane et al., 2000).

Profesionales e investigadores recurren por igual al procedimiento de Rozovskii, donde la componente transversal de la corriente se calcula con respecto a la dirección media del flujo en cada vertical. Esta condición impone un flujo neto cero en dirección a la normal al plano de velocidad media 2DH, dirección que rota continuamente a medida que el dato captado se aproxima (o aleja) de las márgenes de la curva de un canal abierto. Como consecuencia, la supuesta intensidad del flujo secundario se determina localmente en cada perfil vertical de velocidad, en lugar de definirse globalmente en toda la sección transversal.

Rhoads and Kenworthy (1998a) supuestamente eludían en parte estas restricciones del procedimiento proyectando sus datos de campo en secciones fijas. Sin embargo, su contribución desató una polémica que aún persiste. Por esta razón, el cuestinamiento al método de Rozovskii fue y aún es, de sustancial interés tanto desde un punto de vista práctico como teórico.

En esta tesis se propuso contribuir al esclarecimiento de la controversia mediante el uso de dos modelos, producto de diferentes aproximaciones a las ecuaciones de movimiento.

Ambos asumen el establecimiento de un flujo base "normal" en dirección de la corriente, que es cuando gravedad y fricción están en perfecto equilibrio. Mientras el modelo de Engelund (1974) resuelve una ecuación de cantidad de movimiento simplificada en dirección lateral, el modelo de capa vortical resuelve la ecuación de continuidad 2DV en el plano transversal en forma exacta. Ambos predicen información helicoidal útil para evaluar cualquier método de captura y proyección de los resultados (o datos). En rigor, uno de los modelos es incompleto puesto que no resuelve el componente vertical (Up), responsable de "cerrar" la celda de recirculación en el plano 2DV.

No obstante, ambos modelos alcanzan para demostrar que el procedimiento de Rozovskii es equivalente a disociar el campo de flujo en el componente helicoidal más un término de error, nulo en promedio (en profundidad). Esto produce perfiles de circulación erróneos, puesto que el verdadero componente transversal es afectado por la adición de un error, que es función del exceso (o déficit) del componente de velocidad longitudinal respecto de su valor medio. Este componente en nada contribuye al mantenimiento de la celda de circulación secundaria, con excepción de su acción puramente advectiva. En definitiva, si bien el método de Rozovskii produce "vistosas" distribuciones verticales de corrientes secundarias, sus resultados enmascaran la hidrodinámica real del río en la sección transversal medida.

Fue necesario entonces desarrollar un método alternativo para tratar los datos de campo, y fundamentalmente, para proyectar el flujo trasversal. El tratamiento realizado a los datos de campo, acorde a la metodología descripta en el Capítulo 3, fue consistente con las conclusiones teóricas del Capítulo 2, es decir, Rozovskii produce un perfil trasversal erróneo, mientras que el algoritmo basado en coordenadas ENU aisla correctamente la circulación secundaria.

Finalmente, el Capítulo 4 retoma la zona de estudio del Canal de Acceso. Aquí se comparan datos de campo con numéricos a fin de capturar el patrón de flujo dominante en una difluencia del río Colastiné, donde uno de los brazos accede al puerto local. El puerto ha estado en declive desde los 70 debido a los excesivos costos del dragado de mantenimiento del canal de acceso. El objetivo del capítulo fue, por tanto, doble: demostrar la persistencia del patrón de flujo desarrollado en la difluencia a pesar de los cambios morfológicos de reciente aparición, y probar una posible solución al casi centenario problema de sedimentación que presenta el tramo exterior del canal de acceso.

Los conocimientos adquiridos durante la ejecución del estudio ayudaron a validar el código desarrollado para procesar los datos de campo capturados con dos ADCPs. Los resultados confirmaron que los dos brazos de la bifurcación son propensos a desarrollar corrientes secundarias. Por otra parte, las simulaciones demostraron que una intervención ingenieril aguas abajo de la bifurcación, a fin de invertir la dirección de la

corriente, puede establecer un flujo capaz de auto-dragar el tramo exterior del canal de acceso, convirtiendo la difluencia existente en una confluencia estable.

En síntesis, esta tesis reúne cuatro contribuciones novedosas:

i) la extensión de la clásica solución de Engelund,

ii) el análisis teórico que demuestra que Rozosvskii es, de hecho, un método mal condicionado,

iii) el desarrollo de un método alternativo de proyección para el tratamiento de datos de ADCP (en consonancia con el marco teórico discutido aquí), y

iv) la solución ingenieril alternativa que establece que bajo ningún aspecto es necesario reubicar el puerto de Santa Fe a un costo estimado en USD 180 millones.

Contents

List of Figures

List of Tables

Chapter 1

Introduction

1.1 Motivation

The bed topography along river bends is partially shaped by the action of secondary flows that sets in the transversal direction to the primary longitudinal flow, an effect known as helical flow (Rozovskii, 1957; Dietrich and Smith, 1983). This coherent flow structure is the result of a local competition between the curvature-induced centrifugal acceleration and the counteracting pressure force associated with the lateral gradient of the water surface along the curved channel (Engelund, 1974).

It turns out that the cross-flow, where turbulence plays a minor role (Blanckaert and de Vriend, 2004), contributes to the local scour of the outer bank modifying the bed topography of the cross sections observed in river bends. Thus, on the basic flow there is a superimposed flow in the transverse direction, termed "secondary flow", which occupies the large part of the cross section and thereby named the centre-region cell to differentiate it from the outer cell that is often observed near the outer bank (Blanckaert and de Vriend, 2004).

Secondary currents represents a local process that scales with channel width (B), water depth (H) and radius of curvature (R), and exhibit different behaviors depending on the aspect ratio $\beta = B/H$ and $\alpha = R/B$ (Rozovskii, 1957; Yalin, 1992; Kashyap et al., 2012). Whereas Hickin (1978) cited the range $1.4 \leq \alpha \leq 4.0$ for many alluvial rivers, apparently the vast majority of known field data about secondary currents lie in the range $1.0 \leq \alpha \leq 6.0$ and $10 \leq \beta \leq 15$ (Table 1.1). These cross-stream circulations driven by centrifugal forces are important on their own right (Engelund, 1974; Leschziner and Rodi, 1979; de Vriend, 1981), despite some authors believed their role in shaping the bed topography has been over-emphasized over the years (Hooke, 1980).
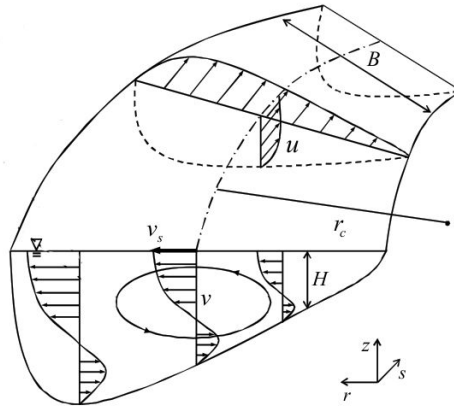
FIGURE 1.1: Velocity profile in curved channels

TABLE 1.1: Some field data from rivers around the world

River	B(m)	H(m)	β	α
Desna, Ukraine (Rozovskii, 1957)	150.0	3.5	43.0	2.3
Squamish, Canada (Hickin, 1978)	77.0	6.9	11.2	1.9
Severn, UK (Bathurst et al., 1979)	12.0	0.90	13.3	5.9
Dommel, The Netherlands (de Vriend and Geldof, 1983)	7.0	0.58	12.0	2.8
Muddy Creek, USA (Dietrich and Smith, 1983)	5.5	0.5	11.0	1.5
Brahmaputra, Bangladesh (Richardson and Thorne, 2001)*	450.0	6.0	75.0	6.3
Sacramento, USA (Dinehart and Burau, 2005)	130.0	12.0	10.8	4.3
Klarälven, Sweden (Dargahi, 2004)	75.0	5.0	15.0	1.9
Spree, Germany (Sukhodolov, 2012)	26.0	2.2	11.8	6.0
bifurc. Colastiné, Argentina(Morell et al., 2014)	130.0	10.0	13.0	1.1
Lower Paraná, Argentina (Szupiany et al., 2009)*	850.0	15.00	57.0	3.0
Colastiné, Argentina (Morell et al., 2014)	130.0	10.00	13.0	1.1

* *confluences*, whose hydrodynamics is not necessarily equivalent to those observed on river bends (Rhoads and Kenworthy, 1998a)

As pointed out by Leschziner and Rodi (1979), knowledge of the mechanics of three-dimensional 3D helical flows facilitates the prevention of silting, the location of navigation channels and water intakes, and the stabilization of riverbanks. Nevertheless, in spite of the large body of experimental data on curved flows available nowadays, notably the works of Rozovskii (1957), Shiono et al. (1999) and Blanckaert and de Vriend (2004), who studied bends with central angles and aspect ratios of 180° and 13.33; 60°-180° and 2.83, and 120° with 3.6, respectively, there are few field studies to date detailing the structure of helical flows driven by centrifugal forces.

On the other hand, and despite repeated assurances given by the research community that ADCP (acoustic Doppler current profiler) measurements are appropriate to capture 3D flow patterns in rivers, no single issue in contemporary meander research, and stream confluence research as well, is perhaps more controversial than the debate surrounding the role of helical motion (Rhoads and Sukhodolov, 2001). The controversy involves

disagreement about the presence or absence of helical motion, and about the method used to detect it from field data (Rhoads and Kenworthy, 1998a; Lane et al., 1999; Rhoads and Kenworthy, 1999; Lane et al., 2000; Richardson and Thorne, 2001; Parsons et al., 2007; Szupiany et al., 2009). Part of the main concern of this thesis is therefore related with the manner in which secondary circulation is defined, measured, and isolated from the primary flow, whose strength and orientation must be independent of observer point of view.

One of the most popular method to isolated the secondary flow from the primary flow is based upon a velocity rotation scheme originally developed by Rozovskii (1957), and later reintroduced by Bathurst et al. (1977). The Rozovskii procedure computes the cross-stream component in relation to the mean flow direction for each individual vertical velocity profile. This method identifies the primary velocity direction for each profile as the depth-integrated flow vector, and the secondary currents are then obtained by an orthonormal projection against this average vector within each vertical profile (Dietrich and Smith, 1983).

The present thesis takes an extra step in analyzing the appropriateness of the Rozovskii method to isolate secondary currents. The work relies on field data collected over a span of almost 10 years (Table 1.2). From that period, most field data were collected during the execution of the present thesis (2008-2013).

TABLE 1.2: Summary of ADCP surveys with discharge reported either at the entrance channel to Santa Fe harbour or at main channel of the Colastiné river surrounding Las Gallinetas Island. Fieldwork parameter: z_w^* : water stage measured at Santa Fe's harbour, Q : mean discharge, V : mean-vessel velocity, Δz : cell (bin) size, and Δt : sampling or averaging interval.

Date	z_w^* [m]	Q [m^3/s]	V [m/s]	Δz[m]	Δt[s]
2004[a],[1]	11.23	856±98	0.72	0.90	20
2006[a],[1]	11.51	917±101	0.62	0.50	5, 10
2007[a],[1]	12.16	663±116	1.36	1.10	10
2008[a],[1]	10.78	622±119	1.15	0.75	10
2009[a],[1]	13.27	1083±126	0.65	0.90	10
2010[b],[1]	12.78	1085±63	1.52	0.25	0.59
2012[b],[1],[2]	10.57	595±14	1.15	0.25	0.59
2012[b],[2]	10.56	1419±16	1.23	0.25	0.59
2013[b],[1]	11.24	863±43	1.25-1.79	0.25	0.59

[a]Sontek River Surveyor 1000kHz, [1] entrance channel to Santa Fe harbour
[b]TRDI Río Grande 1200 kHz, [2] Colastiné river, "Las Gallinetas" confluence

1.2 Hipothesis

From disagreements and disputes that was arise from the Rozovskii method is assumed as thesis hypothesis the premise that Rozovskii method used to extract the lateral component of an asymmetric helical flow field data, presents an inherently bias wrong affecting its outcome.

In other words, it is assumed that the secondary currents computed with Rozovskii contain an intrinsic error

1.3 Objetives

A considerable part of the present work involved the collection of highly accurate field data that supposedly contains helical flow behavior. It was therefore of paramount importance to verify the capability of available methods to filter the sought behavior from raw data.

Consequently, the thesis concerns with several issues: firstly, with the field-based observations captured with an ADCP treatment in order to isolate secondary circulation from a primarily skewed flow; secondly, with the Rozovskii method to project secondary currents, and finally, with the comparison between results generated by the well-known 3D numerical engine Telemac and field data.

Briefly speaking, the thesis content divides in three separate albeit related objectives, each one constituting a potential publication:

i. to question the Rozosvskii procedure to isolate secondary circulation from a skewed primary flow from a theoretical point of view,

ii. to verify the theoretical predictions with field, experimental, data and eventually, to propose an alternative procedure to project the secondary currents,

iii. characterize the flow pattern in a difluence an alluvial river Paraná system by a comparison of field data and numerical simulations.

To that aim, river bottom surveying with an echo-sounder and 3D velocity measurements with an ADCP were undertaken at several cross sections of two study sites located within the alluvial floodplain of the Paraná River (Figure 2.1).
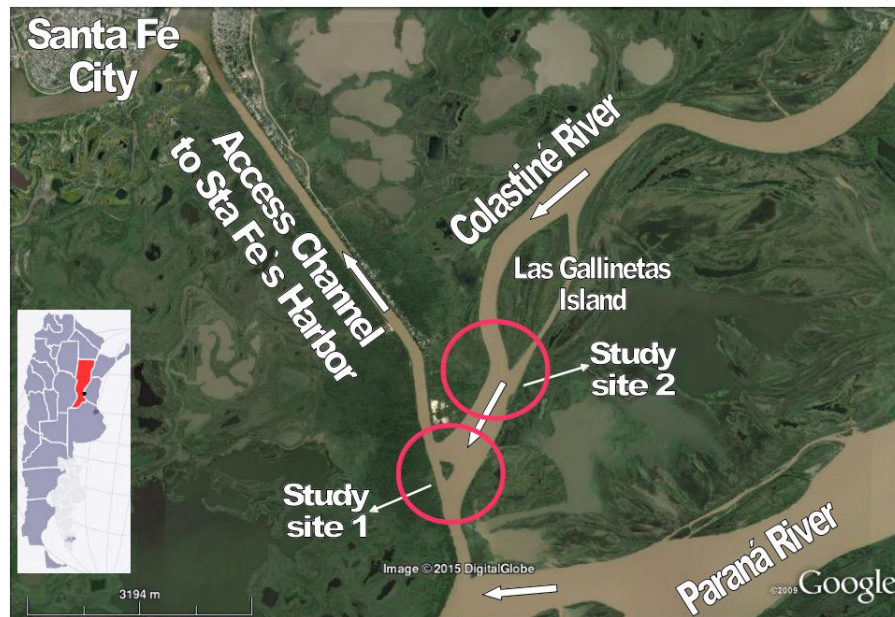
FIGURE 1.2: Study sites within the aluvial system of the Paraná River

1.4   State of the Art

Besides the contributions mentioned before, it is well worth to cite the pioneer work of Thomson (1876), who was one of the first to describe the formation of cells of secondary currents in curved open-channels. Even earlier, Boussinesq (1868) had solved theoretically the problem of a viscous fluid flowing freely in a prismatic and curved open channel of slowly varying curvature, obtaining the classical two layers solution flowing in opposite directions. The Bousssinesq's solution was revised years later by Rozovskii (1957) in the context of the Russian school contributions onto the mechanics of river bends, and revisited by Engelund (1974) and Johannesson and Parker (1989a) among others. Therefore, most of the available contributions on the subject can be grouped in three different categories:

1.4.1   Theoretical Contributions

Besides Boussinesq (1868) contribution, most theoretical advances has been set forth by the Rozovskii (1957) monograph, and years later by the work of Engelund (1974) and Johannesson and Parker (1989a). Their contributions were later improved by Kikkawa et al. (1976), and then reviewed by Falcon (1984).

Kitanidis and Kennedy (1984) proposed a non-conservative 3D phenomenological model to estimate the phase-lag between the flow velocity fluctuation and meander wavelength, a mechanism believe to be partially responsible of the meander formation process. Their

contribution was later revisited by Johannesson and Parker (1989a), who developed a river bend model from the depth-averaged form of the conservation laws.

1.4.2 Modelling Contributions

There are many contributions based upon numerical computation of the process, ranging from 2D averaged over depth (2DH) to full 3D simulations. Among all, it is worthwhile to cite the pioneer contribution of Leschziner and Rodi (1979) and the work of Blanckaert and de Vriend (2003).

More recently, modifications and validation of 3D models were introduced by Boxall et al. (2003) and Blanckaert and Graf (2004). Dargahi (2004) applied a 3D flow model to study the flow behavior in a river bifucation. By the same token, Kashyap et al. (2012) employed a 3D model to investigate the effects of curvature ratio and aspect ratio on channel bend.

1.4.3 Field & Laboratory-based Contributions

Most researchers resort to the Rozovskii procedure to isolate the secondary currents from the primary flow component on their field and laboratory studies, regardless of the problem under analysis. The method is based upon identifying the direction of the depth-averaged velocity at an individual vertical, and then decomposing the flow orientation at every elevation in that vertical into one component parallel to the direction of the depth-averaged velocity (assumed to be the primary flow component), and one component perpendicular to it (assumed to be the secondary flow component (Lane et al., 1999).

The application of the method and others as well can be repeatedly found in many applications, which can be classified according to the following problem-oriented situations: a)*streams confluences*, b)*river bends*, c)*submarine canyons*, and d)*tidal forcing and river discharge.*

a) ***Streams confluence***: field studies of streams confluences have mainly focused on fluvial dynamics at or immediately downstream of the location where the confluent flows enter the downstream channel. It was the work of Rhoads and Kenworthy (1998a) that sparked the controversy about the capability of the Rozovskii method to isolate secondary currents from skewed flows in streams confluence (Lane et al., 1999; Rhoads and Kenworthy, 1999; Lane et al., 2000; Rhoads and Sukhodolov, 2001; Parsons et al., 2007; Szupiany et al., 2009; Parsons et al., 2013)

b) ***River bends***: Bathurst et al. (1977) reintroduced the Rozovskii procedure to treat field measurements of long-stream and cross-stream velocities by sampling the Severn river in UK with an electromagnetic flow-meter. Later on site investigations of secondary currents in river bends were conducted by Dietrich and Smith (1983) in the Muddy Creak (USA), and more recently by Dinehart and Burau (2005) in the Sacramento River (USA), who tested a suite of methods for resolving cross-stream velocity distributions from data collected using ADCP. Daniels and Rhoads (2006) reported the results of three-dimensional flow structure from a meander bend along a low-energy stream in the Midwestern United States. Measurements of three-dimensional velocities were obtained with acoustic Doppler velocimeters (ADVs). In 2012 Sukhodolov (2012) examined the flow structure using results of field measurements carried out in a bend of the Spree river in Germany. Also, Zinger et al. (2013) documented the 3D structures of flow and bed morphology of developed chute cutoffs on meander bend on the Wabash River, USA.

c) ***Submarine canyons***: the plan-form patterns of meandering submarine channels and subaerial fluvial bends show many similarities that has given rise to strong analogies concerning the fluid dynamics of these channel types. Corney et al. (2006) and Straub et al. (2008) investigated and compared flows within fluvial meanders and submarine model channel bends.

d) ***Tidal forcing and river discharge***: in recent times, many studies related to tidal forcing and river discharge have been carried out. Chant (2002) related the strength, structure and character of secondary flow forced by flow curvature to variations in river discharge and tidal forcing through analysis of ADCP data. Cuadrado and Perillo (1997) postulate that helicoidal flow pattern was responsible for the large accumulation of sedimentation observed in one of the entrance channels to the Bahía Blanca system harbour, Argentina

1.5   Thesis Content

The idea was to begin with a critical review of the Rozovskii procedure used to project secondary currents onto a cross-flow plane that is defined locally. Towards that aim, two entirely new approximated flow solutions that mimic helical behavior within a prismatic open channel were proposed. The expectation was to have an independent framework where the capability of the Rozovskii procedure to isolate cross-flow from skewed primary flow can be compared to.

Then, an alternatively projection procedure was proposed given the fact that the Rozovskii rotation schem is an ill-conditioned method. Indeed, Chapter 2 shows that the

method turns out to be unreliable, despite its popularity among practitioners and researchers.

Finally, some numerical simulations with Telemac-3d were undertaken to see how close -or far away- can numerics be from properly captured field-based observations.

In more detail, Chapter 2 recalls that captured patterns of 2D river flow velocities in the cross-plane provide the basis for inferring the existence of helical flow in channel bends and stream confluences as well. Nevertheless, some ambiguities still arise when deciding the orientation of the cross-channel plane that defines the downstream and cross-stream component of flow. Researchers usually refer to the procedure named after Rozovskii, which computes the cross-stream with respect to the mean flow direction at each vertical, forcing by definition a zero net discharge in outward and inward directions. As a consequence, the secondary flow strength is determined locally at each vertical velocity profile instead of defining it on the entire cross-section. Rhoads and Kenworthy (1998a) apparently circumvented this aspect of the Rozovskii procedure by projecting their field data onto fixed cross-sections. However, their contribution sparked a controversy that continues to the present days. For that reason, the questioning of the Rozovskii method is of substantial interest. Chapter 2 seeks to contribute to the elucidation of the controversy with the implementation of two simple close flow solutions that exhibits helicoidal behavior. The work shows that despite the cross-flow looking results delivered by the Rozovskii method, its decomposition is clearly biased and introduce a systematic error in the cross-stream fields.

Chapter 3 reviews critically the capability of the so-called Rozovskii method to isolate a cross-flow from a skewed primary flow. The revision relies on field data collected with an ADCP at two study sites located on the alluvial plain of the Paraná River (Argentina). The river surveying included bathymetry data obtained with an echo sounder and detailed 3D velocity measurements at several cross sections of both study sites. It is here established, in tune with the previous theoretical findings, that the Rozovskii method indeed blends the streamwise velocity component with the crosswise component. A systematic -or blind- application of the method yields the cross-flow component but adds a zero depth-averaged error proportional to the streamwise velocity. To achieve these conclusions was necessary to develop an alternative projection method entirely based on global or earth coordinates instead of local procedures, as customary in the Rozovskii decomposition.

Finally, Chapter 4 presents field and numerical data depicting the flow pattern formed at a diffluence of the Colastiné River, Argentina, where one branch accesses the Santa Fe City's Harbor. The harbor has been in decline since the 1970s due to costly maintenance dredging of the access channel. The objective of the work was thus twofold: to show

the persistence of the flow pattern developed at the diffluence despite recent morphological changes seen at the site, and to test a possible solution to the entrance channel sedimentation problem. Knowledge gained during the execution of the study helped to validate a code developed to process field data captured with two ADCPs. The results confirm that both branches are prone to developing secondary currents. Simulations show that an engineering intervention downstream of the bifurcation can establish a self-dredging flow reversal along the access channel, turning the actual diffluence into a stable confluence.

Chapter 5 grouped the work major conclusions and potential guidelines for future research. It can be said that the thesis major contributions are:

- *i)* the extended theoretical solution to the classical Engelund's model (Engelund, 1974),

- *ii)* the theoretical analysis showing the Rozosvskii method is indeed an ill-posed projection,

- *iii)* the alternative method to project cross-flow (based on global coordinates), and

- *iv)* the engineering solution to the relocation of the Santa Fe City's harbor.

Appendix contains relevant and/or related material but not essential for the thesis development.

Chapter 2

On the Rozovskii method to isolate secondary circulation from skewed flow

Captured patterns of 2D river flow velocities in the cross-plane provide the basis for inferring the existence of helical flow in channel bends and in stream confluences as well. Nevertheless, some ambiguities still arise when deciding the orientation of the cross-channel plane that defines the downstream and cross-stream component of flow. Practitioners and researches usually refer to the procedure named after Rozovskii, where the cross-stream component is computed with respect to the mean flow direction at each vertical, forcing by definition a zero net discharge in outward and inward directions. As a consequence, the secondary flow strength is determined locally at each individual vertical velocity profile instead of defining it on the entire cross-section. Rhoads and Kenworthy (1998a) circumvented this aspect of the Rozovskii procedure by projecting their field data onto fixed cross-sections. However, their contribution sparked a controversy that rages on to the present days. For that reason, the questioning of the Rozovskii method is of substantial interest. It is therefore the purpose of this chapter to contribute to the elucidation of the controversy with the implementation of two simple close flow solutions that exhibits helicoidal behavior. It is then established that despite the cross-flow looking results delivered by the Rozovskii method, its decomposition is clearly in error and fails to reproduce the cross-stream fields in both cases.

2.1   Introduction

The bed topography along river bends is partially shaped by the action of a secondary flow that sets in the transversal direction to the primary longitudinal flow; an effect known as helical flow (Rozovskii, 1957; Dietrich and Smith, 1983). This coherent flow structure is the result of a local competition between the curvature-induced centrifugal acceleration and the counteracting pressure force associated with the lateral gradient of the water surface along the curved channel (Engelund, 1974). Whereas electromagnetic current meters were used intensively in the past to detect the presence of secondary currents (Bathurst et al., 1977; Hickin, 1978; de Vriend and Geldof, 1983; Dietrich and Smith, 1983; Rhoads and Kenworthy, 1998a), nowadays ADCP (acoustic Doppler current profiler) measurements have gained considerable acceptance because of their efficiency to study the three-dimensional (3D) structure of free-surface flows, where the trend is to repeat crossings along linear routes to resolve weak cross-stream velocities (Dinehart and Burau, 2005; Jackson et al., 2009; Parsons et al., 2013). As a result, regardless of the measurement device employed, captured patterns of 2D velocities in the cross-plane provide the basis for inferring the existence of helical flow in river bends (Dinehart and Burau, 2005), and in stream confluences as well (Rhoads and Kenworthy, 1998a; Rhoads and Sukhodolov, 2001; Szupiany et al., 2009). Nevertheless, some ambiguities still arise when deciding the orientation of the cross-channel plane that defines the downstream and cross-stream component of flow (Dietrich and Smith, 1983; Lane et al., 2000). Practitioners and researchers usually refer to the procedure developed by Rozovskii (1957, p.138), where the secondary flow strength is determined locally at each individual vertical velocity profile (Bathurst et al., 1977; Parsons et al., 2007; Szupiany et al., 2009; Coz et al., 2010) instead of defining it on an entire cross-section (Dietrich and Smith, 1983). The cross-stream component is then computed with respect to the mean flow direction at each vertical, forcing by definition a zero net discharge in outward and inward directions. As pointed out by Dietrich and Smith (1983), the analysis of Rozovskii is, therefore, able to capture the proper secondary circulation on a local-basis, albeit may fail to produce the complete picture of the cross-stream velocity field.

Rhoads and Kenworthy (1998a) circumvented this aspect of the Rozovskii procedure by projecting their field data onto fixed cross-sections. However, their contribution sparked a controversy that rages on to present days (Lane et al., 1999; Rhoads and Kenworthy, 1999; Lane et al., 2000; Rhoads and Sukhodolov, 2001; Parsons et al., 2007; Szupiany et al., 2009; Parsons et al., 2013). Similar questioning were raised within the computational fluid dynamics community (Leschziner and Rodi, 1979; Boxall et al., 2003, p.156), where velocities are referred to in global coordinates without need of using correction angles to account for zero net cross-stream discharge. For that reason, and

due to the considerable investment required to collect reliable field data and the risk to infer misleading conclusions regarding the presence and the structure of secondary circulation on river bends or stream confluences (Rhoads and Sukhodolov, 2001, p.2403), the questioning of the Rozovskii method is of substantial interest. It is therefore the purpose of this chapter to contribute to the elucidation of the controversy.

We revisit the Rozovskii method under the light of a rather simple analytical flow solution that exhibits helical behavior, obtained under assumptions si-milar to those invoked by Kitanidis and Kennedy (1984). However, it must be clear that the proposed model of helical flow behavior by no means attempts to capture the precise complex flow-patterns that set in curved open-channels. It should be considered as a semi-heuristic model built from past and probed descriptions of the process (e.g. Rozovskii, 1957; Engelund, 1974; Kitanidis and Kennedy, 1984), and aimed solely to judge the capability of the Rozovskii method to isolate a well-defined cross-circulation from the primary flow component. An attempt in this direction was made by Lane et al. (2000) using numerical tools instead as the preferred reference frame where the outcome of the method was compared to.

Here, using ideas borrowed from lubrication theory, a flow solution is obtained whose downstream component is uncoupled from the cross-stream component. For the downstream velocity distribution, the classical slip-velocity concept of Engelund (1974) is used, whereas the cross-flow component is driven by a vortex sheet with fixed vorticity distribution along a thin strip located at the cross-section centre superimposed to a lateral drift to account for the cross-stream discharge effect. It is then established that the Rozovskii method, albeit conceptually correct, may introduced a systematic bias when reproducing the entire cross-stream velocity field.

2.2 Theoretical Framework

Unless stated otherwise, a lower case letter represents a dimensionless quantity and its corresponding upper case letter represents its dimensional counterpart. Bold face upper case letters represent vectors.

Figure 2.1 defines a reference frame for two analytical models for laterally unbounded flows, intended to provide two base solutions to test the Rozovskii decomposition. The first model corresponds to the classical Engelund (1974) solution, and the second to the foregoing vortex sheet model.

The water layer of depth H_0 bounded by the bed elevation Z_b and by the free-surface elevation Z_w that flows along the curved channel depicted in Figure 2.1 is now referred to
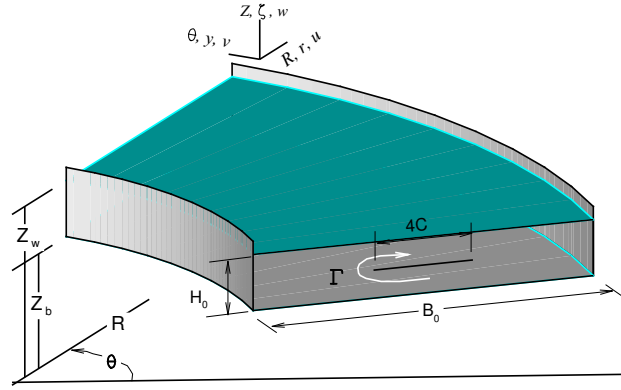
FIGURE 2.1: Reference frame for a channel bend

in cylindrical polar coordinates (R, θ, Z), with (U_R, U_θ, U_Z) as the corresponding velocity components.

2.2.1 Engelund model

The long wave approximation yields the well-known hydrostatic pressure distribution within the flow field. If it is further assumed a motion approximately independent of θ, the full set of governing equations reduces (Appendix A.2.1), after an order of magnitude analysis (Rozovskii, 1957), to

$$\frac{1}{R}\frac{\partial\left(RU_R\right)}{\partial R} \simeq 0 \tag{2.1}$$

$$-gS_R + \epsilon\frac{\partial^2 U_R}{\partial Z^2} \simeq -\frac{U_\theta^2}{R}, \tag{2.2}$$

$$gS_\theta + \epsilon\frac{\partial^2 U_\theta}{\partial Z^2} \simeq 0, \tag{2.3}$$

where the free-surface slopes in crosswise and streamwise directions are

$$S_R = \frac{\partial Z_w}{\partial R} \ , \ S_\theta = -\frac{1}{R}\frac{\partial Z_w}{\partial \theta} \ , \tag{2.4}$$

respectively.

The primary flow component obeys the downstream momentum equation for uniform and steady flow in a wide rectangular channel, whose integration between Z_b and a point Z, after specifying the boundary shear stress at the bed level and the stress-free condition at the water surface, leads to

$$U_*^2 = gH_0 S_\theta \ , \tag{2.5}$$

known as the friction or shear velocity. Moreover, Rozovskii (1957, p.93), and similarly Engelund (1974), argued that for a circular channel the downstream water surface slope must satisfy $S_\theta = I_\theta/R$, where I_θ is the uniform water surface elevation drop per unit of turning angle. Consequently, the shear velocity varies inversely with the square root of R

$$S_\theta = \frac{R_0}{R} S_\theta^0 \;,\;\; U_* = \sqrt{\frac{R_0}{R}} U_*^0 \;, \tag{2.6}$$

However, since the Engelund's model is based upon a constant eddy viscosity assumption defined along the channel centerline by

$$\epsilon_0 = \frac{U_*^0 H_0}{a} \;, \tag{2.7}$$

equation (2.6) forces ϵ to vary with the inverse of the square root of R. Above, the choice $a = 13.04$ fits a parabolic velocity defect law into the upper 90% of the log-law profile in the least square sense (Engelund (1974), Appendix A.2.4).

From now on either the superscript or subscript "0" means quantities measured at the channel centerline. Then, if the following similar solutions in product form of functions of non-dimensional quantities

$$\zeta = \frac{Z - Z_b}{H_0} \;, \tag{2.8}$$

$$\frac{U_R}{V} = \frac{R_0}{R} \left[j(\zeta) + u(\zeta) \right] \;, \tag{2.9}$$

$$\frac{U_\theta}{V} = \sqrt{\frac{R_0}{R}} \, v(\zeta) \;, \tag{2.10}$$

$$S_R = \alpha \frac{R_0}{R^2} \frac{V^2}{g} \;, \tag{2.11}$$

are introduced, the equations (2.2) and (2.3) become

$$j''(\zeta) = 0 \;, \tag{2.12}$$

$$u''(\zeta) = \mathrm{Re}_0 \left[\alpha - v^2(\zeta) \right] \;, \tag{2.13}$$

$$v''(\zeta) = -2\beta . \tag{2.14}$$

Here $' = d/d\zeta$, $j(\zeta)$, $u(\zeta)$, and $v(\zeta)$ are mere shape functions defining the crosswise drift, helical and streamwise flow components, respectively, V a free-surface velocity scale in the downstream direction, α a yet undetermined nondimensional parameter, Re_0 an effective Reynolds number defining the strength of the cross-circulation, and r_* the dimensionless slip-velocity at the channel bed in the radial direction (Engelund

(1974); Johannesson and Parker (1989b))

$$\mathrm{Re}_0 = \frac{U_0 H_0}{\epsilon_0} \quad , \quad \beta = \frac{a}{2}\frac{U_*^0}{V} \quad , \quad r_* = \frac{U_{R_b}}{U_*} \; . \tag{2.15}$$

Above, U_0 is a lateral velocity scale that depends on R albeit it is on the order of $V H_0/R_0$ whenever $R_0/R \simeq 1$.

The flow entering an open-channel bend exhibits a skewed main velocity distribution (towards the inner bank in the first part of the bend, and gradually shifting outwards to the outer bank near the bend exit (de Vriend and Geldof, 1983)). The choice $j''(\zeta) = 0$ governs a radial velocity drift that satisfies the constraint (2.1) while preserving the Engelund model for $u(\zeta)$ and $v(\zeta)$, defined by (2.13) and (2.14), respectively.

The set of ordinary differential equations (2.12)-(2.14) must obey the following restraints: *i*) a mean lateral flow equal to the slip-velocity at the channel bed and no stresses at the water surface, *ii*) a downstream velocity at the channel bed proportional to the friction velocity and equal to V at the water surface, *iii*) a zero cross-circulation flux in lateral direction and, *iv*) an equal ratio between the velocity components and the shear stresses components in radial and azimuthal directions. In mathematical terms:

$$j(0) = \frac{2\beta}{a}r_* \quad , \quad j'(1) = u'(1) = 0 \; , \tag{2.16}$$

$$v'(0) = 2\beta \quad , \quad v(1) = 1 \; , \tag{2.17}$$

$$\int_0^1 u(\zeta)d\zeta = 0 \; , \tag{2.18}$$

$$2\beta\left[j(0) + u(0)\right] = v(0)\left[j'(0) + u'(0)\right] \; . \tag{2.19}$$

The solutions to (2.12)-(2.14) are readily obtained after using the boundary conditions (2.16)-(2.18)

$$v(\zeta) = 1 - \beta\left(1 - \zeta\right)^2 \; , \tag{2.20}$$

$$j(\zeta) = \frac{2\beta}{a}r_* \; , \tag{2.21}$$

$$u(\zeta) = \mathrm{Re}_0\left[P_6(\zeta) - D\right] \; , \tag{2.22}$$

where the sixth degree polynomial $P_6(\zeta)$ and the constant D are

$$P_6(\zeta) = \frac{(\alpha - 1)}{2}(1 - \zeta)^2 + \frac{\beta}{6}(1 - \zeta)^4$$
$$- \frac{\beta^2}{30}(1 - \zeta)^6 \; , \tag{2.23}$$

$$D = \frac{(\alpha - 1)}{6} + \frac{\beta}{30} - \frac{\beta^2}{210} \; . \tag{2.24}$$

The remaining unknown α is now determined by the mixed boundary condition (2.19) (Engelund, 1974)

$$\alpha = \frac{1 - \beta + \left(\frac{3}{5} - \frac{4r_*}{a\mathrm{R}_{\mathrm{e}_0}}\right)\beta^2 - \frac{1}{7}\beta^3}{1 - \frac{\beta}{3}} \; , \tag{2.25}$$

Equations (2.23) and (2.24) are identical to equations (25) and (26) of Engelund (1974) in powers of $\zeta'(= 1 - \zeta)$ differing in that he considered the vertical axis up side down. The expression (2.25) for α coincides with expression (28) of Engelund (1974) except by the factor $4r_*/a\mathrm{R}_{\mathrm{e}_0}$, entirely attributed to the lateral drift contribution $j(\zeta)$ considered here.

The coefficients α and β can now be expressed in terms of the Chezy resistance factor $\mathrm{C_Z}$ which relates, in the limit of vanishing channel curvature, the depth averaged downstream velocity V_m with the shear velocity according to

$$\mathrm{C_z} = \frac{V_m}{U_*} \; . \tag{2.26}$$

The relationships (2.10) and (2.20), once combined with (2.6) for U_* and with (2.15) for $V/U_\star^0$ into (2.26), leads to

$$\beta = \frac{1}{\frac{1}{3} + \frac{\mathrm{C_z}}{6.5}} \; . \tag{2.27}$$

Accepting now that U_0 scales with $V H_0/R_0$, the effective Reynolds number R_{e_0} defined in (2.15) can be expressed as

$$\mathrm{R}_{\mathrm{e}_0} = \left(\frac{\mathrm{C_z}}{1 - \frac{\beta}{3}}\right)\left(\frac{H_0}{R_0}\right) a \; , \tag{2.28}$$

obtained upon using (2.7) and (2.26) after invoking the result $V_m/V = 1 - \beta/3$. Finally, since the factor r_* is also function of the Chezy coefficient (see Appendix A.2), the expressions (2.20)-(2.22) define a biparametric family of solutions in $\mathrm{C_z}$ and H_0/R_0, as explicitly shown by Engelund (1974, p.1636).

Figure 2.2a depicts the vertical distribution of the streamwise component $v(\zeta)$ for $\mathrm{C_z} = 9$, and the helicoidal component $u(\zeta)$ for varying for $\mathrm{C_z}$. The modified solution is steeper than the "classical" solution of Engelund; the later obtained by setting $r_* = 0$ in (2.25).

Nonetheless, part of the concern here is not about which solution best captures the secondary motion, but rather to provide grounds to test the capability of the Rozovskii decomposition to isolate helical currents from primary skewed flows. The modified solution exhibits an asymmetric cross-flow component and a skewed primary flow component. The asymmetry of the cross-flow depends on $\mathrm{C_z}$ and H_0/R_0 (Figure 2.2b), and the skewness of the primary flow depends on the angle $tan^{-1}(\sqrt{R/R_0}(3 - \beta)a/6\beta r_*)$.
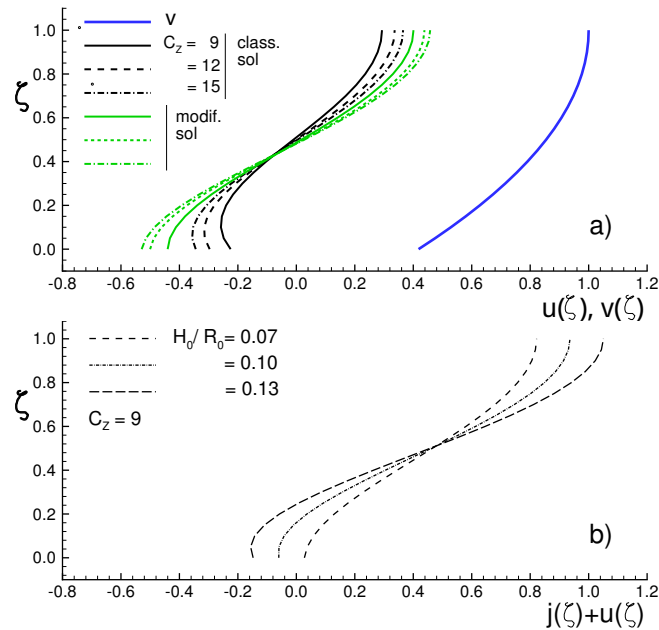
FIGURE 2.2: a) Streamwise and crosswise velocities, b) total crosswise velocity for different ratios H_0/R_0

2.2.2 Vortex sheet model

Kitanidis and Kennedy (1984) used a heuristic model based upon a non-conservative albeit plausible 3D velocity field to account for the phase lag between the secondary currents strength and the curvature of a channel bend. Following them, this work proposes a phenomenological flow model through a reductionist process able to deliver a fully conservative helicity behaviour along mildly curved open-channels instead.

First of all, the so-called small-gap limit is invoked, which reduces the full set of governing equations into a quasi-decoupled system representing pure shearing motion in the azimuthal direction and secondary circulation driven by centrifugal instabilities in the cross-plane (Hall, 1975).

In second place, we established that the Engelund model is, within the bounds of suitable hypothesis, a subset of the small-gap equations. Finally, it is shown that an even simpler model, i.e. the Engelund reduced form of the momentum equation in the downstream direction, and the small-gap limit of the continuity equation in the cross-plane suffices to get helical motion.

In the presence of a free-surface, it is convenient to split the total pressure P between its hydrostatic and dynamic components in the form

$$P = P_0 + \rho g(Z_w - Z) + P_d \,,$$

for some given reference pressure P_0. Then, for a cross-section with slowly-varying water depth $H_0 = H_0(R)$, the following change of variables

$$(x, y, \varsigma, z_w) = \left(\frac{R - R_0}{H_0}, \theta, \frac{Z - (Z_b + H_0/2)}{H_0}, \frac{Z_w}{H_0} \right), \tag{2.29}$$

$$(u, v, w, p) = \left(\frac{H_0 U_R}{\epsilon_0}, \frac{U_\theta}{V}, \frac{H_0 U_Z}{\epsilon_0}, \frac{P_d H_0^2}{\rho \epsilon_0^2} \right), \tag{2.30}$$

is appropriated to cast the flow solution domain and the governing equations in dimensionless form. However, before going any further the chosen scales require some clarification.

On one hand, V above represents a water surface velocity in the downstream direction though this time assumed to be proportional to $\Omega_0 R_0$, where Ω_0 is the mean angular velocity of the curved flow. On the other hand, H_0 represents a vertical length scale that could be locally defined or, eventually, considered constant. For instance, a possible choice for H_0 is the cross-sectional mean water depth, or the water depth at the channel centerline, whatever is more convenient. For analytical purposes the choice $H_0(R)$ in (2.8) maps $Z = [Z_b, Z_w]$ into $\zeta = [0, 1]$ whereas the choice (2.29) maps Z into $\varsigma = [-1, 1]$ for reasons that will become apparent in a moment. On the contrary, a constant length scale H_0 is preferred for computational purposes (e.g. Vionnet, 1995). Finally, all dimensionless variables retain their foregoing definitions unless stated otherwise.

Substituting the dimensionless variables (2.29) and (2.30) into the governing equations detailed in Appendix A.2.1, taking the limit $\delta \to 0$, the following reduced form of the equations of motion is obtained

$$\frac{\partial u}{\partial x} + \frac{\partial w}{\partial \varsigma} = 0, \tag{2.31}$$

$$u \frac{\partial u}{\partial x} + w \frac{\partial u}{\partial \varsigma} = -\frac{\partial p}{\partial x} + \mathcal{L}u + \mathrm{T_a} v^2 - \left(\frac{\mathrm{C_z^2} a^2}{\mathrm{F_m^2}} \right) \frac{\partial z_w}{\partial x}, \tag{2.32}$$

$$u \frac{\partial w}{\partial x} + w \frac{\partial w}{\partial \varsigma} = -\frac{\partial p}{\partial \varsigma} + \mathcal{L}w, \tag{2.33}$$

$$u \frac{\partial v}{\partial x} + w \frac{\partial v}{\partial \varsigma} = 2\beta + \mathcal{L}v, \tag{2.34}$$

where the reduced Laplacian operator $\mathcal{L}$, the small-gap parameter δ, the Taylor number $\mathrm{T_a}$, and the Froude number $\mathrm{F_m}$ are defined as

$$\mathcal{L} = \frac{\partial^2}{\partial x^2} + \frac{\partial^2}{\partial \varsigma^2} \quad , \quad \delta = \frac{H_0}{R_0}, \tag{2.35}$$

$$\mathrm{T_a} = \frac{\Omega_0^2 R_0 H_0^3}{\epsilon_0^2} = \mathrm{R_e^2} \delta \quad , \quad \mathrm{F_m} = \frac{\sqrt{g H_0}}{V_m}, \tag{2.36}$$

respectively. Above, the streamwise Reynolds number

$$\mathrm{R_e} = \frac{V H_0}{\epsilon_0} \tag{2.37}$$

should not be confussed with the effective lateral Reynolds number defined in (2.15) and (2.28).

If the chosen scales were appropriated, the relative magnitude of each term is indicated by the dimensionless factor preceding it. More precisely, for a low-gradient sandy river values of $\mathrm{C_z} \simeq 10$ and $\mathrm{F_m} \simeq 0.1$ are reasonable, and since the free-surface gradient in the lateral direction far outweighed the other terms (i.e. $\mathrm{C_z^2} a^2 / \mathrm{F_m^2} \simeq 10^6$), the rigid lid approximation in the lateral direction, $\partial z_w / \partial x = 0$, is more than appropriated for the present problem.

The resultant system, known as the small-gap equations, is widely used to study the stability of axisymmetric Taylor-Couette flows (Hall, 1975), and the behaviour of rotary lip seals in lubrication applications as well (Vionnet, 1995). Note that the limit $\delta \to 0$ entirely neglects curvature effects, albeit they are retained through the centrifugal term by holding the Taylor number fixed as $\delta \to 0$. It follows that a layer of water that satisfies the wide-channel approximation $H_0/B_0 \ll 1$, together with the smallness requirement on δ, $H_0/R_0 \ll 1$, may be subjected to centrifugal instabilities that in turn could drive secondary currents along the cross-section. Consequently, in the terminology of flows along open-channel bends, the "small-gap" parameter actually embodied the "mildly curved and shallow" flow condition concept for (2.31)-(2.34) to be valid.

It is possible to recover and enhance the Engelund model from the small-gap equations. To that aim, and after assuming: *i*) negligible inertia, *ii*) constant pressure gradient in lateral direction, *iii*) negligible vertical velocity across the water layer ($w \simeq 0$), and *iv*) boundary layer behaviour (with much larger diffusion of vorticity in the normal than in the lateral direction to a solid boundary), i.e.

$$\frac{\partial p}{\partial x} = \alpha \mathrm{T_a} \quad , \quad \frac{\partial p}{\partial \varsigma} \simeq 0 \quad , \quad \frac{\partial^2}{\partial x^2} \ll \frac{\partial^2}{\partial \varsigma^2} \, ,$$

the equations (2.13) and (2.14) are recovered with $\mathrm{T_a}$ instead of $\mathrm{R_{e_0}}$, and defined over $\varsigma = [-1, 1]$ in place of $\zeta = [0, 1]$. The approximation closes with the constraint (2.31). In brief, the exact set of equations (2.31)-(2.34), obtained in the limit $\delta \to 0$, embodied the Engelund model.

However interesting the small-gap equations are, a restricted form of them is enough to get helical flow behaviour. The continuity constraint (2.31) together with the afore-mentioned Engelund streamwise momentum equation provides a full and convenient

description for (u, v, w).

Considering now that all bounding surfaces (lateral walls, bed and free-surface) effects are far away to be safely ignored, and that (2.7) describes the turbulence mixing adequately under the hypothesis that supports the slip-velocity concept at channel bed of Engelund (1974).Equation (2.31) is thus solved with 2D irrotational flow theory with the aid of conformal mapping. A layer of negligible thickness, located in the mid-channel section $\varsigma = 0$, $|x| \leq 4c < B_0/H_0$, $c = C/H_0$, where the vorticity is assumed uniformly distributed with total cross-circulation Γ (Figure 2.1), provides a surface across which the horizontal component of velocity is discontinuous albeit satisfying (2.31) exactly.

As mentioned before, the expected skewing of the main velocity distribution is towards the inner bank in the first part of the bend, outwards further downstream (de Vriend and Geldof, 1983). Thus, it is customary to decompose the lateral velocity into a depth-averaged or drift component, and a helicoidal part as in (2.9) (Johannesson and Parker, 1989b; Blanckaert and de Vriend, 2003)

$$U_R = U_{R_l} + U_{R_h} \,. \tag{2.38}$$

Then, an uniform lateral drift velocity of magnitude $u_l \lessgtr 0$ is added to the pure cross-circulation motion, whose combined solution is (see Appendix A.2.5 for details)

$$u = u_l - \frac{\gamma}{2\pi} \frac{h(x,\varsigma)}{d(x,\varsigma)} \quad , \quad w = \frac{\gamma}{2\pi} \frac{f(x,\varsigma)}{d(x,\varsigma)} \,, \tag{2.39}$$

where $\gamma = \Gamma/\epsilon_0$ is the dimensionless total circulation, and h and f the circulation functions in the cross-stream and the vertical directions,respectively, given by

$$
\begin{aligned}
h &= sgn(\varsigma)\sqrt{\frac{-p+d}{2}} \quad , \quad f = sgn(x)\sqrt{\frac{p+d}{2}} \,, & \tag{2.40} \\
p &= (x^2 - 4c^2) - \varsigma^2 \,, \\
d &= \sqrt{\left[(x+2c)^2 + \varsigma^2\right]\left[(x-2c)^2 + \varsigma^2\right]} \,. & \tag{2.41}
\end{aligned}
$$

Above, the sign of the real number t is defined as follows

$$
sgn(t) = \begin{cases} \text{-1 if } t < 0 \\ 1 \text{ if } t \geq 0 \end{cases} \tag{2.42}
$$

The 2D velocity field solution (2.39), valid in the cross-plane (r, ς), is now complemented with the decoupled 1D solution in the streamwise direction, equation (2.14). Summarizing, the proposed phenomenological 3D model that mimics helical flow behaviour, after

going back to physical variables and scaling against V instead, is

$$\frac{(U_R, U_\theta, U_Z)}{V} = \left(\frac{U_{R_l}}{V} - \frac{\Gamma}{2\pi V H_0} \frac{h(x,\varsigma)}{d(x,\varsigma)}, \; v(\varsigma), \right.$$
$$\left. \frac{\Gamma}{2\pi V H_0} \frac{f(x,\varsigma)}{d(x,\varsigma)} \right), \tag{2.43}$$

where $v(\varsigma)$ is defined in (2.20). Note that $h(x,\varsigma)$ is an odd function in ς, i.e. $h(x,-\varsigma) = -h(x,\varsigma)$ whereas d is even, $d(x,-\varsigma) = d(x,\varsigma)$. Consequently, the total volume flux due to the transverse circulation through the vertical vanishes

$$\int_{-1}^{1} \frac{h(x,\varsigma)}{d(x,\varsigma)} d\varsigma = \int_{-1}^{0} \frac{h(x,t)}{d(x,t)} dt + \int_{0}^{1} \frac{h(x,\varsigma)}{d(x,\varsigma)} d\varsigma = 0 \;, \tag{2.44}$$

as it can be shown by introducing $t = -\varsigma$, and swapping the limits of integration.

The vertical distribution of the vortex sheet solution at $r = 0$ (mid-channel section) is shown in Figure 2.3 for different values of $U_{R_l} H_0 / \Gamma$. The radial component of velocity
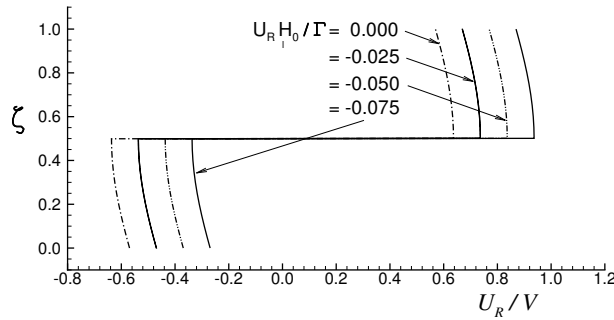
FIGURE 2.3: Radial velocity component.

is continuous everywhere but across the vortex sheet, where the condition of zero-mass flux is attained through a jump discontinuity.

Figure 2.4(a) depicts the vector field of the composite 3D phenomenological flow model when U_Z is set, for illustration purposes, equal to zero. Finally, Figure 2.4(b) shows the helicoidal nature of the composite flow through the use of ribbon-like streamlines starting from arbitrary locations at the inlet cross-section. The depicted velocity field is the outcome of a clock-wise cross-circulation (negative) with a non-zero mean radial velocity in outwards direction corresponding to the parameter ratio $U_{R_l} H_0 / \Gamma = -0.04$.

2.2.3 The Rozovskii method

The longitudinal and the principal velocities along a riverbend do not coincide precisely since the velocity vectors are, in general, obliquely aligned with respect to any referential
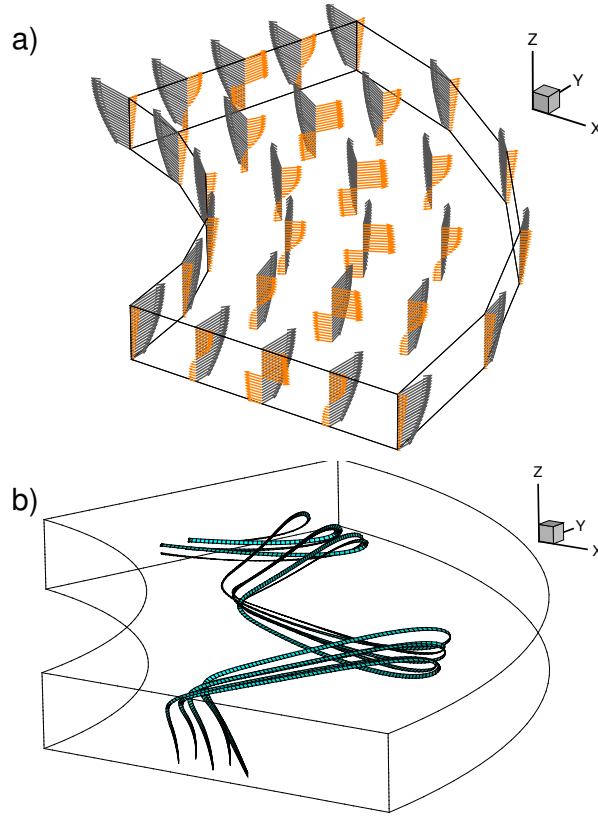
FIGURE 2.4: a) 3D composite velocity field, b) streamtraces

cross-section (de Vriend and Geldof, 1983). Consequently, the magnitude of a cross-stream component can be influenced by this skewed flow, hampering the correct isolation of the helical flow structure (Rhoads and Kenworthy, 1998a; Szupiany et al., 2009).

Rozovskii (1957) claimed that secondary currents at some given vertical if any, occur in a plane normal to the depth-averaged velocity vector. The method was revised and popularized by the work of Bathurst et al. (1977), and still widely used for treating field data (Parsons et al., 2013).

According to Rozovskii (1957)[p.138], if $\mathbf{U} = (U_x, U_y)$ represents the flow velocity in an open-channel bend at any depth Z with respect to Cartesian coordinates (X, Y), whose modulus forms an angle φ with the X-axis whenever $Z_b \leq Z \leq Z_w$, the primary and secondary velocity components, V_p and V_s respectively, are

$$V_p = |\mathbf{U}| \cos(\phi - \varphi) , \tag{2.45}$$

$$V_s = |\mathbf{U}| \sin(\phi - \varphi) . \tag{2.46}$$

To avoid overuse of notation, the equivalence between the velocity fields in terms of the unit base vectors $\mathbf{e}_R, \mathbf{e}_\theta$ and the alternative Cartesian basis $\mathbf{i}, \mathbf{j}$ is sketched in Figure

(2.5). In appendix C the reader can find a discussion about the definition of a positive $v_s(v_s > 0)$ or negative $v_s(v_s < 0)$.
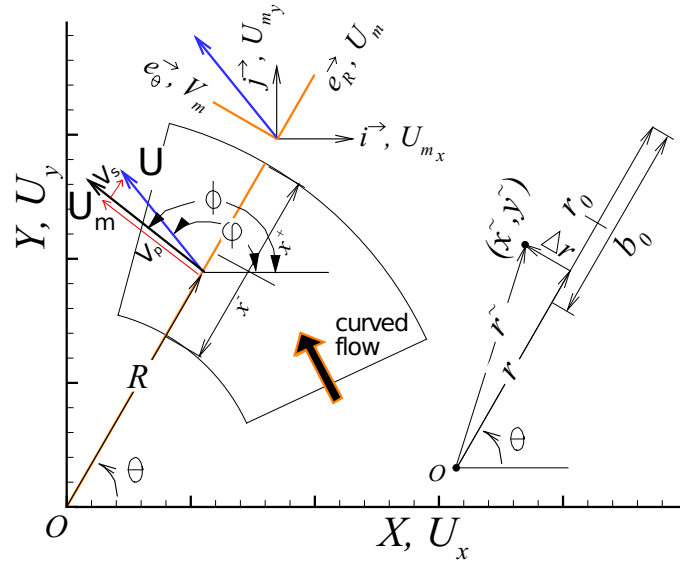
FIGURE 2.5: The Rozovskii decomposition

Expanding the trigonometric expressions with the angle difference identities, the decomposition becomes

$$\begin{bmatrix} V_s \\ V_p \end{bmatrix} = \begin{bmatrix} sin\phi & -cos\phi \\ cos\phi & sin\phi \end{bmatrix} \begin{bmatrix} U_x \\ U_y \end{bmatrix}, \tag{2.47}$$

where ϕ is the angle of the depth-averaged velocity vector $\mathbf{U_m} = (U_{m_x}, U_{m_y})$ with respect to the X-axis

$$\phi = \tan^{-1}\left(\frac{U_{m_y}}{U_{m_x}}\right), \tag{2.48}$$

$$U_{m_x} = \frac{1}{H}\int_{Z_b}^{Z_w} U_x dZ \ , \ \ U_{m_y} = \frac{1}{H}\int_{z_b}^{z_w} U_y dZ. \tag{2.49}$$

Equation (2.48) implicitly satisfies the condition of zero net cross-stream discharge at each vertical, $\int_{Z_b}^{Z_w} V_s dZ = 0$, which is the essence of the Rozovskii procedure to isolate secondary circulation from a skewed flow (Bathurst et al., 1977)

2.3 Results

2.3.1 ADCP kind of data

The Rozovskii method is still used for processing measurements obtained with an ADCP mounted on a moving vessel (Parsons et al., 2013). The method is one of four commonly
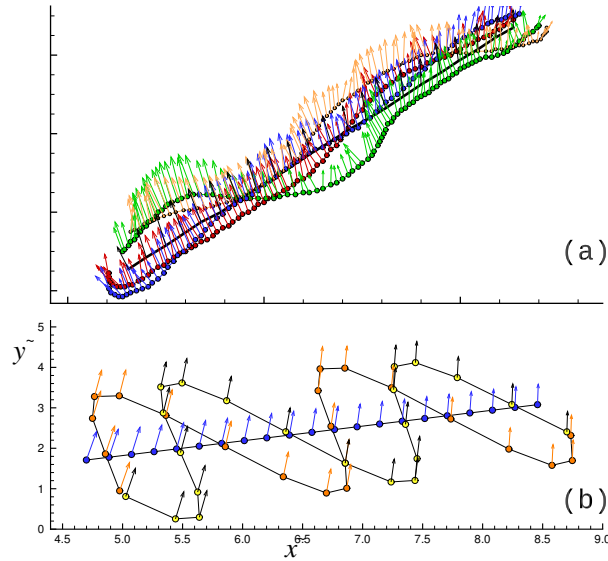
FIGURE 2.6: 2DH velocity field along: (a) real vessel paths when surveying a linear transect with an ADCP, (b) assumed sinusoidal and optimal vessel paths.

employed to rotate a river cross-section to isolate secondary circulation among the so-called centre-line plane, the zero-net cross-stream plane, and the discharge continuity plane (Lane et al., 2000). Others authors, such as Dinehart and Burau (2005) rotated the flow vectors to conform with indicators inferred by the ADCP backscatter intensity.

However, the ambiguities in defining secondary-circulation planes are irrelevant in the present context. The optimal cross-plane is unambiguously defined by $r_{inn} \leq r \leq r_{out}$, $\theta = const$ (Figure 2.5). The limits $r_{inn,out} = \mp b_0/2$ represent the normalized radii along the channel bend banks, used just for illustration purposes since the solutions are laterally unbounded where $b_0 = B_0/H_0$.

Consequently, the foregoing exact solutions are now used as virtual ADCP data where the synthetic flow velocities are sampled at regularly spaced verticals along a sinusoidal or straight vessel path. Figure 2.6(a) depicts repeated transects that oscillate around a targeted linear cross-section measured at the alluvial plain of the Paraná River nearby Santa Fe City (Morell et al., 2014). The waviness arises when the helmsman follows an oscillating path around a planned navigation transect in response to its steering ability, lateral drag, and wind effects.

Other uncertainties originated from different sources (Simpson, 2001), such as the extrapolation employed by the ADCP proprietary software to fill data in the unmeasured portions of the cross-section are ignored because both flow fields are known exactly in the whole domain.

The ADCP internal compass and tilt sensor (roll/pitch) referred water velocities components in terms of the orthogonal East-North-Up (ENU) coordinates, with the first two

later turned into Transverse Mercator (X, Y) coordinates once corrected by the magnetic declination bias. Thus, the virtual data considered here either inherits a small positional error or is free of it if the vessel path is coincident with the cross-plane $\theta = const$. In both cases, the sampled velocity data (U_R, U_θ) is converted into (X, Y)-components and make it 3D with the up-component U_Z.

The following dimensionless system delivers a set of $n_r + 1$ discrete points that mimics such sinusoidal vessel path about the optimal cross-section (Figures 2.5 and 2.6(b)):

$$
\begin{bmatrix} \tilde{x}_j \\ \tilde{y}_j \end{bmatrix} = \begin{bmatrix} cos\theta & -sin\theta \\ sin\theta & cos\theta \end{bmatrix} \begin{bmatrix} r_0 + x_j \\ \Delta r_j \end{bmatrix} , \tag{2.50}
$$

$$
\Delta r_j = a(r)cos\left[\frac{2\pi k}{b_0}(r_0 + x_j) + \varphi_0\right], \tag{2.51}
$$

$$
x_j = -\frac{b_0}{2} + j\frac{b_0}{n_r} , \quad j = 0, 1, \ldots, n_r . \tag{2.52}
$$

Above,

$$
a(r) = \begin{cases} \frac{A}{H_0} & : constant , \\ \frac{A}{H_0}\sqrt{\frac{r_0}{r_0 + x_j}} & : variable , \end{cases} \tag{2.53}
$$

represents alternatively a constant or slowly varying amplitude function with A/H_0 a dimensionless wave displacement at the channel centerline, Δr_j the orthonormal varying vessel departure from the optimal path $\theta = const$, φ_0 an initial phase, k an arbitrary integer representing the total number of wavelengths along the nominal channel width b_0, and $r_0 = R_0/H_0$. The remaining parameters retain the definition given previously. If $A = 0$ the optimal path is recovered.

A straightforward application of the Rozovskii decomposition implies evaluating (U_m, V_m) and (U, V) at each j-*th* vertical profile or water column, in turn divided into n_z depth cells. The depth-averaged velocity components for both models in R, θ directions are (see (2.9), (2.10), and (2.43))

$$
\left(U_{m_j}, V_{m_j}\right)/V = \left(\chi_j\, u_l, \sqrt{\chi_j}\,[1 - \beta/3]\right) , \tag{2.54}
$$

with a primary flow skewness given by

$$
\phi_j = \theta + tan^{-1}\left[\frac{(1 - \beta/3)}{u_l\,\sqrt{\chi_j}}\right] , \quad j = 0, 1, \ldots, n_r. \tag{2.55}
$$

Here, the mean lateral flow u_l and the geometric factor χ_j are $\pm 2\beta r_*/a$ (see (2.21)) and

$$
\chi_j = \begin{cases} r_0/\tilde{r}_j & , \text{ Engelund model,} \\ 1 & , \text{ Vortex sheet model,} \end{cases} \tag{2.56}
$$

respectively, where $\tilde{r}_j = (\tilde{x}_j^2 + \tilde{y}_j^2)^{1/2}$ is defined by (2.50). Whenever $u_l \to 0$, ϕ tends to $\theta + \pi/2$ in (2.55), expressing that the depth-averaged primary flow component is perpendicular to the cross-plane $\theta = const$ (Figure 2.5).

Both cross-flow structures discussed are well defined over a local plane (x, ς) with constant azimuthal angle. However, it is convenient to assume they come from an orthogonal projection based on global coordinates (x, y, ς), in tune with reasons best known to ADCP users.

Any field ADCP data interpretation requires further processing based on local projection procedures such as the Rozovskii (Parsons et al., 2013), or alternative methods based on global coordinates. The former referred to as ENU from now on (Morell et al., 2014).

Figure 2.7(a) shows the vertical distribution produced by the ENU algorithm when the Engelund velocity field is either sampled along the optimal path (vectors) or the sinusoidal path (dots). The associated velocity field delivered by the Rozovskii projection appears in Figure 2.7(b). Figures 2.7(c) and 2.7(d) show equivalent results for the ENU procedure and the Rozovskii decomposition, respectively, when the velocity field come from the vortex sheet model instead.

The sampling along the sinusoidal path produces a weak distortion of the velocity field with respect to its exact vertical distribution, defined along the straight path (Figures 2.7(a) and 2.7(c)). Nevertheless, the Rozovskii method delivers a cross-flow looking projection that is clearly in error.

Summarizing, Figures 2.7(a) and 2.7(c) plot the exact secondary flow delivered for both theoretical models, termed here as ENU in tune with standard ADCP field practice (Simpson, 2001). Any accurate post-processing tool performing data mining from ADCP data should be able to extract and produce graphs similar to those depicted in the Figures 2.7(a) and 2.7(c). The apparent capability of the Rozovskii decomposition to deliver cross-flow looking results may well explain its long-standing acceptance among researchers and practitioners (Parsons et al., 2013).

The cross-stream velocities plotted in Figure 2.7 were "captured" with the following parameters values: $\theta = 20^o$, $n_r = 20, n_z = 20, A/H_0 = 3, k\pi/b_0 = 2$, and $\varphi_0 = \pm 1$. In turn, the cross-stream velocities themselves were formed with some of the parameters values used to produce the solutions portrayed in Figures 2.2 and 2.3.
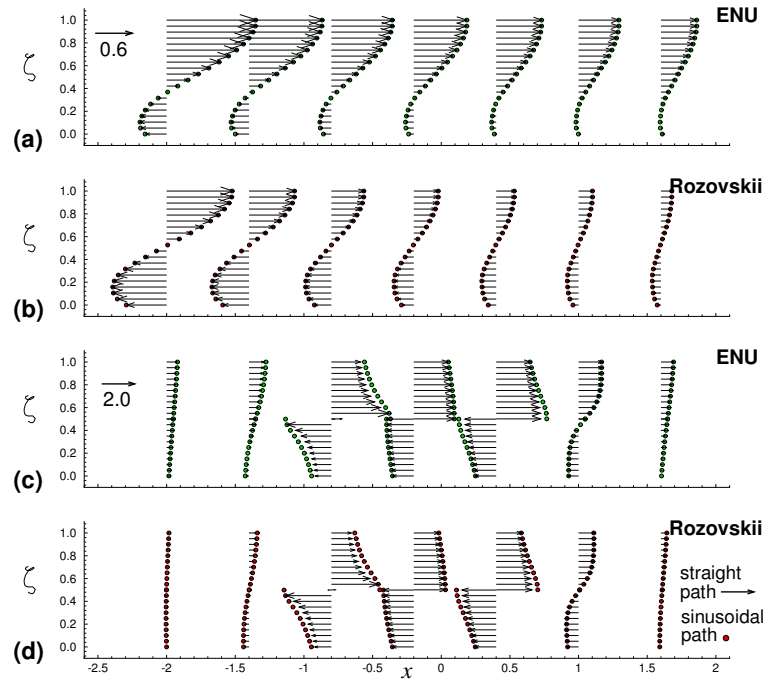
FIGURE 2.7: Dimensionless ADCP data mining from the: (a) Engelund model with ENU, (b) Engelund model with Rozovskii, (c) Vortex sheet model with ENU, (d) Vortex sheet model with Rozovskii.

2.3.2 Error Analysis

2.3.2.1 Positional error

The synthetic data used are error-free from the sampling restrictions commonly faced in any field situation (Oberg and Mueller, 2007). The analysis restricts to the error introduced when collecting data away from the optimal path.

To that aim, it is convenient to assume that vorticity prevails downstream and upstream of the cross-section for distances proportional to the local water depth. In other words, it suffices to assume that the vectors unfolded in Figures 2.7(c) belong to the locally stable 3D flow depicted in Figure 2.4. These data are then transformed first from polar to Cartesian, and afterwards to Rozovskii with (2.47) to construct the error path free vectors shown in Figure 2.7(d). Identical reasoning applies when treating the Engelund data.

Under the bounds of the preceding assumption, the cross-sectionally averaged of the absolute deviation of the velocity collected along the sinusoidal path with respect to the straight path data is

$$\overline{\delta u}|_{xs} = \frac{1}{n_r + 1} \sum_{j=0}^{n_r} \frac{1}{n_z} \sum_{k=1}^{n_z} \frac{|\tilde{u}(\tilde{x}_j - r_0, \varsigma_k) - u(x_j, \varsigma_k)|}{|u(x_j, 1)|} \, . \tag{2.57}$$

TABLE 2.1: Relative values of the absolute deviation

abs. dev.	$a(r)$	Engelund		Vortex sheet	
		ENU	Rozov.	ENU	Rozov.
		Fig.2.7(a)	Fig.2.7(b)	Fig.2.7(c)	Fig.2.7(d)
$\overline{\delta u}\|_{xs}$	con.	0.2%	0.2%	4.4%	4.0%
	var.	0.3%	0.2%	3.7%	3.4%
$\max \overline{\delta u}\|_j$	con.	0.6%	0.4%	27.2%	25.3%
	var.	0.9%	0.6%	21.8%	19.9%

Above, the pointwise absolute deviation is relative to the cross velocity at the free-surface of each profile. The tilde indicates data taken off but orthogonally projected onto the optimal plane, with $\tilde{x}_j$ evaluated according to (2.50).

Table 2.1 summarizes cross-sectionally and maximum depth-averaged values of the relative absolute cross-velocity deviation, computed with the full expression (2.57) for the former case and the inner summation for the later. The Engelund solution depends weakly on the radial position whereas the vortex sheet solution varies sharply nearby the half depth and with the radial position to a lesser extent. However, both methods yield similar error bounds for each testing solution. These are about 0.3 % and 4 % on average with a local maximum of 1 % and 25 % for the Engelund and the vortex sheet models, respectively.

These are expected error bounds if the cross-flow is locally stable, and the vessel departs up to three times the local water depth from the targeted linear transect. The consistency of the error distribution is an indication that whenever data projects correctly onto the optimal plane, the result is independent of the chosen methodology.

2.3.2.2 Identification of Rozovskii elemental error

While the positional error seems to be independent of the projection method, the Rozovskii decomposition produces a cross-circulation pattern clearly erroneous. To isolate the problem, it is first necessary to express the Rozovskii decomposition in terms of the polar components of the flow velocity U_R and U_θ, and their depth-averaged values, namely U_m and V_m, respectively. Thus, the well-known rotation between polar and Cartesian coordinates

$$\begin{bmatrix} U_x \\ U_y \end{bmatrix} = \begin{bmatrix} cos\theta & -sin\theta \\ sin\theta & cos\theta \end{bmatrix} \begin{bmatrix} U_R \\ U_\theta \end{bmatrix}, \qquad (2.58)$$

allows mapping $\mathbf{U_m} = (U_m, V_m)$ onto (U_{m_x}, U_{m_y}) (Figure 2.5). Then, after using (2.47) and (2.58) to relate V_p and V_s with U_R and U_θ, and by noting that $cos(\phi-\theta) = U_m/|\mathbf{U_m}|$

TABLE 2.2: Signs of $e_{rr}(Z)$ depending on bend location

water layer	bend entry	bend exit
upper	$+$	$-$
lower	$-$	$+$

and $sin(\phi - \theta) = V_m/|\mathbf{U_m}|$, the scaled Rozovskii decomposition against V reads

$$\frac{V_p}{V} = \frac{U_m}{|\mathbf{U_m}|}\frac{U_R}{V} + \frac{V_m}{|\mathbf{U_m}|}\frac{U_\theta}{V} \,, \tag{2.59}$$

$$\frac{V_s}{V} = \frac{V_m}{|\mathbf{U_m}|}\frac{U_R}{V} - \frac{U_m}{|\mathbf{U_m}|}\frac{U_\theta}{V} \,, \tag{2.60}$$

valid whenever $|\mathbf{U_m}| \neq 0$. Had the Rozovskii method been correct, the secondary component would inherit just the helical contribution U_R, which is the only crosswise velocity part to isolate from the skewed principal flow.

Two conclusions are easily extracted from (2.60): i) the location of the cross-section does not affect the computation of V_s (θ independent), as it should be in any locally-based projection method, and ii) the magnitude of the secondary current is erroneously affected by the streamwise velocity component. To see these effects better, it is convenient to recall (2.38) with $U_{R_l} \equiv U_m$. Then, the Rozovskii estimation for V_s would read

$$\frac{V_s}{V} = v_{scl}\frac{U_{R_h}}{V} + e_{rr} \,, \tag{2.61}$$

where $v_{scl} = V_m/|\mathbf{U_m}|$ is a positive definite scale factor, and e_{rr} the departure from the helicoidal flow portion given by

$$e_{rr}(Z) = u_{scl}\left[\frac{V_m}{V} - \frac{U_\theta(Z)}{V}\right] \,, \quad u_{scl} = \frac{U_m}{|\mathbf{U_m}|} \,. \tag{2.62}$$

Thus, the Rozovskii decomposition adds a varying error along any vertical profile proportional to the excess (or deficit) of the primary flow velocity component relative to its depth-averaged value.

Any monotonically increasing function for U_θ produces the inequality $V_m - U_\theta(Z) \lessgtr 0$ within the upper and lower portion of the water column, respectively (e.g. Figure 2.2(a)). Then, the error function $e_{rr}(Z)$ could alternatively be negative or positive on the vertical depending if the cross-section locates nearby the bend entry or exit (Table 2.2), where $U_m \lessgtr 0$, respectively (de Vriend and Geldof, 1983).

Each term of the error expression (2.62), resulting from both theoretical models, are plotted in Figure 2.8. The composite velocity matches the Rozovskii decomposition deployed in Figure 2.7(b) and (d), profiles 1 and 4, respectively.
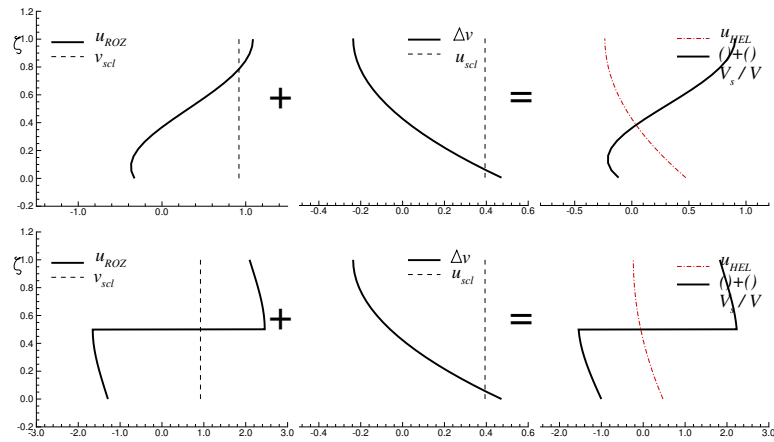
FIGURE 2.8: Rozovskii elemental error: (a) Profile 1 of the Engelund model depicted in Figure 2.7(b), (b) Profile 4 of the Vortex sheet model depicted in Figure 2.7(d)

2.4 Discussion

The adoption of the constant eddy viscosity model of Engelund allows to treat the full 3D free-surface flow problem along curved channels into two simpler and decoupled problems (1D + 2D). The models so obtained exhibit secondary currents or helical flow behavior where the Rozovskii method can be compared with.

The Rozovskii procedure supposedly provides a criterion for determining whether coherent flow patterns of secondary circulation may be present along a curved flow path. The method relies on computing a discrete sequence of "flow planes" oriented perpendicular to the local orientation of the depth-averaged velocity field. Only at verticals where $\phi = \theta + \pi/2$ the Rozovskii local plane of reference and the actual cross-sectional plane containing the cross-circulation be equivalent. Apparently, the Rozovskii method takes the correct orientation of the cross-stream plane, it computes the excess (or deficit) of the cross-component of flow velocity relative to its respective depth-averaged value. This was clearly the objective set forth by Rozovskii ... *if the angle ϕ is correctly computed, then the transverse flow across the vertical must be equal to zero* (Rozovskii, 1957, p.139).

However, the systematic use of Rozovskii embeds part of the downstream velocity component in the secondary circulation (despite a zero depth-average error). Consequently, the isolation of a well-defined cross-circulation from the primary flow component could be masked by a straightforward application of the Rozovskii procedure.

Regarding the controversy, both Rhoads and Kenworthy (1999) and Lane et al. (1999, 2000) were right on their own. Rhoads and Kenworthy (1998a) explicitly uses a set of local coordinates to project the Rozovskii components of the velocity field. In turn,

Lane et al. (2000) were right when claiming to abandon Rozovskii when treating flow data in river bends.

An alternative projection method based on absolute coordinates should be used instead. Morell et al. (2014) decompose the 2DH and the 3D velocity fields along the cross-wise and the stream-wise planes components of the absolute velocity relative to the ground, with the addition of the up component for the 3D case. Finally, both the tangential and up components define the vertical 2DV representation of the flow field along the projected cross-stream plane. Their treatment of the flow field is fully compatible with the data mining outcome depicted in Figures 2.7(a) and (c).

Chapter 3

A global-referenced grid method to isolate secondary circulation from a skewed flow

The capability of the so-called Rozovskii method to isolate the helical flow component from a skewed primary flow is critically reviewed. The 90's witnessed a debate about the appropriateness of the method for processing field data. The questioning of it is of substantial interest given its continued use and the still unanswered issues that stem from that debate. This chapter shows that despite the capability of the method to project crossflow-looking distributions, it adds an error source term that depends on the streamwise velocity. The method indeed mixes what it pretends to isolate, which is a pure crossflow component dissociate from the streamwise component. An alternative projection method, based on globally referenced grid coordinates, is here proposed. Contrary to most published works, it relies on an algorithm that coalesces ADCP (acoustic Doppler current profiler) neighboring cells data without resorting to any interpolation whatsoever. The revision relies on field data collected with an ADCP at two study sites located on the alluvial plain of the Paraná River, Argentina.

3.1   Introduction

The so-called Rozovskii procedure provides a criterion for determining whether coherent flow patterns of secondary circulation may be present along a curved flow path (Bathurst et al., 1977). The method computes a sequence of projection planes oriented perpendicular to the local direction of the depth-averaged velocity field.

However, the secondary flow field is not necessarily perpendicular to the mean flow at each faceted plane. The ambiguities surrounding the optimal cross-plane orientation have been the subject of intense research (Dietrich and Smith, 1983; Lane et al., 2000; Dinehart and Burau, 2005).

Consequently, many authors prefer to use instead a set of *tangential* (t), *normal* (n), and *up* (z) cylindrical coordinates departing from a local center of curvature. The z-axis points perpendicularly upward from the horizontal (t, n) plane, and increments Δn and Δt relate in the polar coordinates sense, $\Delta n = t \Delta \theta$, with θ the azimuthal angle.

Rhoads and Sukhodolov (2001) used that frame to study a river confluence, as well by Daniels and Rhoads (2006) and Sukhodolov (2012) for analyzing obstruction effects and flow turbulence on meander bends, respectively. In all cases, they deployed one or several ADV (acoustic Doppler velocimeter) along predetermined verticals to measure the fluid velocity components. The 3D (three-dimensional) velocity field were measured with respect to the right-handed coordinate system (t, n, z) aligned with the main sensor axis, in turn oriented orthogonally to the cross section at each vertical.

Field measurements produced in the past with flowmeters either at river bends (Rozovskii, 1957; Hickin, 1978; Bathurst et al., 1979) or confluences (Rhoads and Kenworthy, 1998a) oriented the sensor head with similar criteria.

Thus, Rhoads and Sukhodolov (2001), Daniels and Rhoads (2006) and Sukhodolov (2012) followed standard laboratory practices, where an ADV scans the curved flow on fixed cross-sections (Blanckaert and de Vriend, 2004; Kashyap et al., 2012). Upon filtering the data, the proprietary software of the ADV yields then profiles of the time-mean transverse velocity $u_t(z)$, or crossflow cells (u_t, w) in the plane (t, z).

However, contrary to the readily identifiable (t, n, z) storage format of the data produced by stationary devices, measurements from moving platforms are not directly transferable into (t, n) coordinates. In the later case, the *up* coordinate is invariant unless uncorrected by roll and pitch.

A typical moving platform is a downward-looking ADCP mounted on fiberglass or aluminum-made boats (Muste et al., 2004; Szupiany et al., 2007). With an ADCP the trend is to repeat transects along linear routes for resolving weak cross-stream velocities (Dinehart and Burau, 2005). Then, the adequacy of repeating transects for capturing 3D flow structures adds another issue to the dauting task of processing field data.

In the presence of large convective instabilities as those found at the confluence of two streams (Best and Roy, 1991), the repetition of transects would cut the information in uncorrelated pieces. The front cover of Ashworth et al. (1996)'s book provides a striking

TABLE 3.1: Some studies based on the Rozovskii method.

River	device	mechanism
Desna and Snov, Ukraine[1]	current-meter	bend-driven
Severn, UK[2]	elect. flowmeter	bend-driven
Kaskaskia, USA[3]	elect. flowmeter	confl.-driven
Upper Paraná, Argentina[4]	ADCP	confl.-driven
Lower Paraná, Argentina[5]	ADCP	confl.-driven
Ain River, France[6]	ADCP	cavity-driven
Wabash-Embarras, USA[7]	ADCP	confl.-driven
White-Wabash, USA[8]	ADCP	confl.-driven
Wabash-Ohio, USA[9]	ADCP	bend cutoff-driven

[1](Rozovskii, 1957) , [2] (Bathurst et al., 1979), [3] (Rhoads and Kenworthy, 1998a), [4] (Parsons et al., 2007) , [5] (Szupiany et al., 2009) , [6] (Coz et al., 2010), [7] (Parsons et al., 2013) , [8] (Jackson, 2013) , [9] (Zinger et al., 2013)

example of such Kelvin-Helmholtz instabilities. Thus, repeat-crossings based research should restrict to stable flow situations (Jackson et al., 2009).

On the other hand, the intrinsic structure of the ADCP data have hampered the interpretation of secondary currents role given the lack of proper tools to translate between geographical and local coordinates until recently (Parsons et al., 2013). The data handling shortcoming and the straightforward implementation of the Rozovskii decomposition made it the preferred choice for researchers to infer the existence of transverse flow on a river cross-section.

Table 3.1 details devices used and the type of curvature-driven mechanism of the secondary currents, isolated in turn with the Rozovskii procedure. It was the work of Rhoads and Kenworthy (1998a) what caused a controversy (Lane et al., 1999; Rhoads and Kenworthy, 1999; Lane et al., 2000; Richardson and Thorne, 2001; Rhoads and Sukhodolov, 2001), whose implications have not been addressed yet in light of the continued use of the method. For that reason, the questioning of the Rozovskii method is still of substantial interest.

Hickin (1978) quoted that the formation of cross-flow scales with the channel width, B, water depth, H, and channel curvature, R. Although the ratio $\beta = B/H$ changes with flow stage and channel planform geometry, most values reported in the literature range from 10 to 15 (Table 3.2). Similarly, the ratio $\alpha = R/B$ lies within $1.0 \leq \alpha \leq 6.0$. Flume-based research usually works with other ranges (Blanckaert and de Vriend, 2004; Kashyap et al., 2012).

On a river bend, the competition between centripetal acceleration and pressure forces ensures the presence of persistent crossflow (Engelund, 1974). Thus, a river bend and

its associated ADCP data constitute a benchmark against which the Rozovskii method can be compared with.

The objective of this chapter is thus twofold: to introduce an alternative procedure to isolate and project secondary currents, and to test the Rozovskii decomposition against it. The last objective seeks to confirm with field data previous theoretical findings (Chapter 2).

Despite the Rozovskii rotation may hit the order of magnitude of the secondary current (Parsons et al., 2007, 2013), the procedure adds an error proportional to the streamwise flow component. Although the error is zero when averaged over depth, its pointwise magnitude growths with the flow skewness.

The alternative procedure bases its projections on global-referenced grid coordinates. It relies on an algorithm that coalesces ADCP neighboring cells data without resorting to any interpolation whatsoever. The use of the global coordinates produces field data readily available for comparison with 3D numerical simulations, which is another drawback of the Rozovskii decomposition (Leschziner and Rodi, 1979; Boxall et al., 2003).

Knowledge acquired while executing the study helped to refine a computer routine developed to process field data obtained with an ADCP. Both, the Rozovskii and the global-referenced grid methods interpret data from two sites located nearby the outlet of the Colastiné River, in the alluvial plain of the Paraná River, Argentina (Figure 3.1). The sites are a river bifurcation, with one branch behaving as a river bend typified by $\beta \simeq 13$, and a river confluence by $\beta \simeq 75$, both with $\alpha \simeq 1$ (Table 3.2).

The next section describes the study sites and the collected data. There follows a description of the algorithm developed to treat the field data. Then, a qualitative comparison between Rozovskii results and the new projection is presented, to close with few recommendations.

3.2 Materials and Methods

3.2.1 Study sites

The Colastiné River is an anabranch of the Paraná River with riverbanks composed of a $4-6$ m layer of clay and silt overlying coarse sands (Iriondo, 2007), with a free-surface slope of about 2 cm/km. It is a typical meandering river with an approximated average water depth, channel width, and discharge of 6 m, 600 m, and 1700 $\mathrm{m^3s^{-1}}$ respectively.

TABLE 3.2: Studies on river bends around the world.

River	$\alpha = R/B$	$\beta = B/H$
Desna, Ukraine[1]	2.3	43.0
Squamish, Canada[2]	1.9	11.2
Severn, UK[3]	5.9	13.3
Dommel, The Netherlands[4]	2.8	12.0
Muddy Creek, USA[5]	1.5	11.0
Klarälven[†], Sweden[6]	1.9	15.0
Sacramento, USA[7]	4.3	10.8
Lower Paraná[⋆], Argentina[8]	4.2	54.0
Spree, Germany[9]	6.0	11.8
bifurc. Colastiné, Argentina[10]	1.1	13.0
Colastiné[⋆], Argentina (this study, XS3)	1.4	75

[1](Rozovskii, 1957, XS3) , [2] (Hickin, 1978, XS7) , [3] (Bathurst et al., 1979, Llandinam bend, XS 3), [4] (de Vriend and Geldof, 1983, reach average) , [5] (Dietrich and Smith, 1983, reach averge) , [6] (Dargahi, 2004, XS_W13), [7] (Dinehart and Burau, 2005, XS6) , [8] (Szupiany et al., 2009, XS_B2) , [9] (Sukhodolov, 2012, XS4), [10] (Morell et al., 2014, XS4) , [†] inferred numerically , [⋆] confluence

About 80-85 % of the river sediment transport is wash load made of silts and clays barely found in measurable quantities in the bed (Drago and Amsler, 1988). The rest is bed-material made of fine and medium sands predominantly carried in suspension. Morell et al. (2014) includes size distributions of bed material collected at the sites.

Before reaching the main channel of the Paraná River, the Colastiné outlet forms a diffluence node with the entrance channel to the Santa Fe's city harbor, whose sharp turn makes it prone to developing secondary currents. Few hundreds of meters upstream the vegetated bar, named "Isla Las Gallinetas", provides the second scenario to test the Rozovskii procedure (Figure 3.1).

3.2.2 Field data

Table 3.3 summarizes the low-medium flow conditions found and parameter values used in the field works. The surveys discussed from now on were conducted in both cases with a downward-looking 1200 kHz TRDI ADCP mounted on the side a fiberglass vessel. A second serial port connected a digital 210 Hz Raytheon single beam echo sounder to the on-board computer during the surveys.

The ADCP integrated water velocity and bathymetry data with a Leica 1200 differential Global Positioning System working in Real Time Kinematic (dGPS RTK) mode and reading at the rate of two positional points per second. The setup delivered an accuracy of ±0.02 m in planar and ±0.04 m in vertical directions. The ADCP internal compass
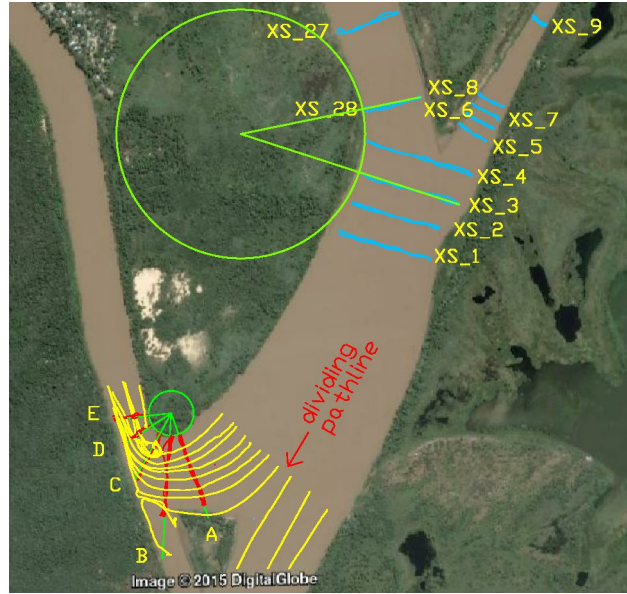
FIGURE 3.1: Location of the study sites, in the floodplain of the Paraná River, Santa Fe, Argentina.

and tilt sensor (roll/pitch) then referred water velocities components in terms of *East-North-Up* or *ENU* coordinates.

On the curved reaches, the surveyed transects aligned with rays departing from a virtual center of curvature located on the inner -convex- bank sides. The curvature center defines the radius of a circle that best fits the river planform on the inner bank. Otherwise, in the straight reaches, the transects aligned approximately perpendicular to the streamwise velocities. Once in the field, the helmsman maneuver to navigate along the drawn transects as closely as possible by tracking the vessel position in real-time with the dGPS RTK (Figure 3.1).

Both bed elevation models, $z_b = z_b(x^+:East, y^+:North)$, were generated with bathymetry data collected by the echo sounder and depth data estimated with the ADCP TRDI. The echosounder data referenced in geographical coordinates was later converted to Transverse Mercator (TM) coordinates with the formulas given by Snyder (1987). In a separate processing, the water depth data from the four beams of the ADCP were geo-referenced with the bathymetry export option of the Velocity Mapping Toolbox (Parsons et al., 2013). Both data sets were later merged with information from complementary sources and processed according to the procedure detailed in Morell et al. (2014). The additional data usually represent borders of mid-channel vegetated bars and river banks elevations.

TABLE 3.3: River parameters estimated during the fieldworks: z_w : water stage above datum at Santa Fe harbour in m, Q_r and Q_l, discharges along right and left branches in m^3s^{-1}, respectively, and V_b : boat velocity during surveys in ms^{-1}

site	date	z_w	Q_r	Q_l	V_b
bifur. Col.[1]	4 May 2010	12.78	1085 ± 63	$-$	1.52
	17 Dic 2013	11.24	863 ± 43	1976 ± 3	1.79
confl. ILG[2]	2 Mar 2012	10.57	1401 ± 18	182 ± 6	1.51
	20 Sep 2012	10.56	1419 ± 16	182 ± 4	1.23

[1] Colastiné River outlet, [2] "Isla Las Gallinetas"

3.2.2.1   The external reach of the entrance channel

The bifurcation node has remained stable in the past hundred years, in part due to the maintenance dredging performed periodically over the so-called external reach that links the entrance channel with the Paraná River.

Morell et al. (2014) reconstructed the site morphology with a century-long record, establishing the Y-shaped node exhibits nowadays a bifurcation angle close to the stability range reported by Federici and Paola (2003). Table 3.3 details the fieldworks where the cross-sections labeled from A to E (Figure 3.1) were surveyed with four to six transects. Pathlines produced by releasing two floats equipped with standard navigation software, together with numerical results, confirm that the flow along both bifurcation branches matches the hydrodynamic of a river bend.

The pathlines along the left branch are smooth, weakly curved, whereas on the right branch tend to point regions of flow reversal, stagnation, separation, and reattachment. A dividing pathline, extending behind the mid-channel island bounds the zone of stagnant water formed there, so conforming with a solid river bend response (Figure 3.1).

The procedure detailed later recomputes, among other ADCP output data, the river discharge through the surveyed transects. The lateral distribution of the horizontal depth-averaged (2DH) flow velocity $(U(s), V(s))$ depicted in Figure 3.2 delivers a hydrodynamic portrayal consistent with the surveyed pathlines pattern. Here, s is the arc length along the cross-section, increasing from left to the right bank when looking downstream. A vortex is clearly visible in the vicinity of the curve apex, on the inner bank. The lower window of Figure 3.2 shows that the point of maximum depth shifts towards the outer bank from upstream to downstream.

3.2.2.2   At the confluence "Isla Las Gallinetas"

The diffluence-confluence unit formed by the vegetated sandbar "Isla Las Gallinetas", located few hundred meters upstream from the Colastiné River outlet, steers flow and
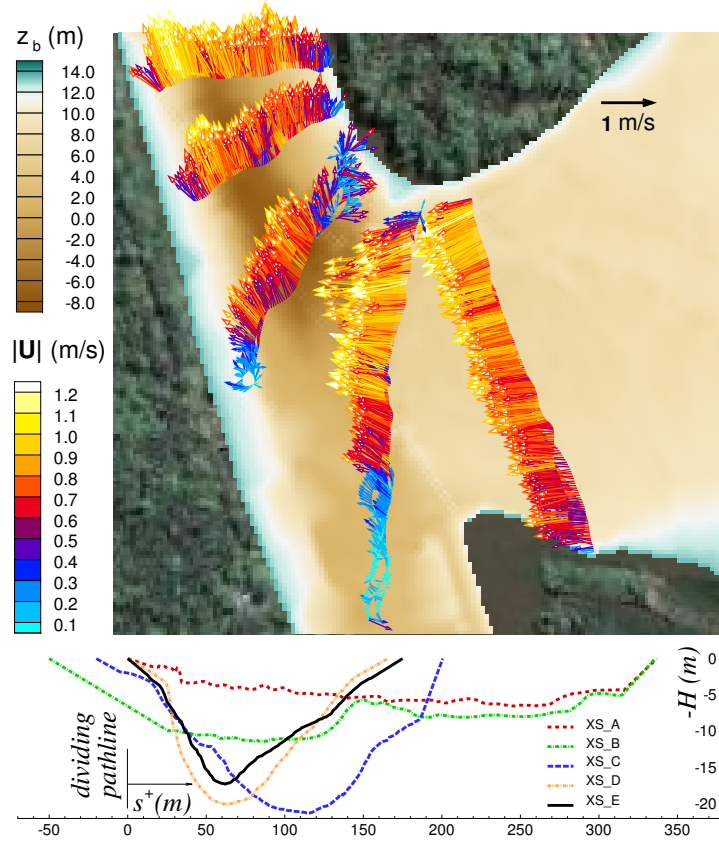
FIGURE 3.2: Top: depth-averaged velocity (U, V) on transects at the external reach of the entrance channel to Santa Fe's harbor. Vectors colored with $|\mathbf{U}| = \sqrt{U^2 + V^2}$, in ms^{-1}. Bottom: cross-sections with zero progressive distance at the dividing pathline (Figure 3.1).

sediment around both branches without human interference.

Detailed ADCP measurements were undertaken at the site with two to four repeating transects each starting at the entrance channel mouth (Table 3.3).

Figure 3.3 depicts the 2DH flow field surveyed on September 20, 2012. The lower window shows the bed elevation of the left branch is, on average, 5.5 m above the main channel of the Colastiné River. The height differences between the elevations of the scour hole found at the confluence and the bottoms of the left and right branches are 8.5 m and 3 m, respectively. A sandbar is visible between XS_4 and XS_3.

The left branch discharge reaches full mix a short distance from XS_4, approximately at twice the right upstream channel width. The fast mixing responses to the small flow momentum ratio of the confluence, $(\rho QV)_l / (\rho QV)_r \simeq 0.09$. Here, the subscripts r and l and Q retain the definition given in Table 3.3, and ρ denotes water density and V cross-sectionally average flow velocity (ms^{-1}).
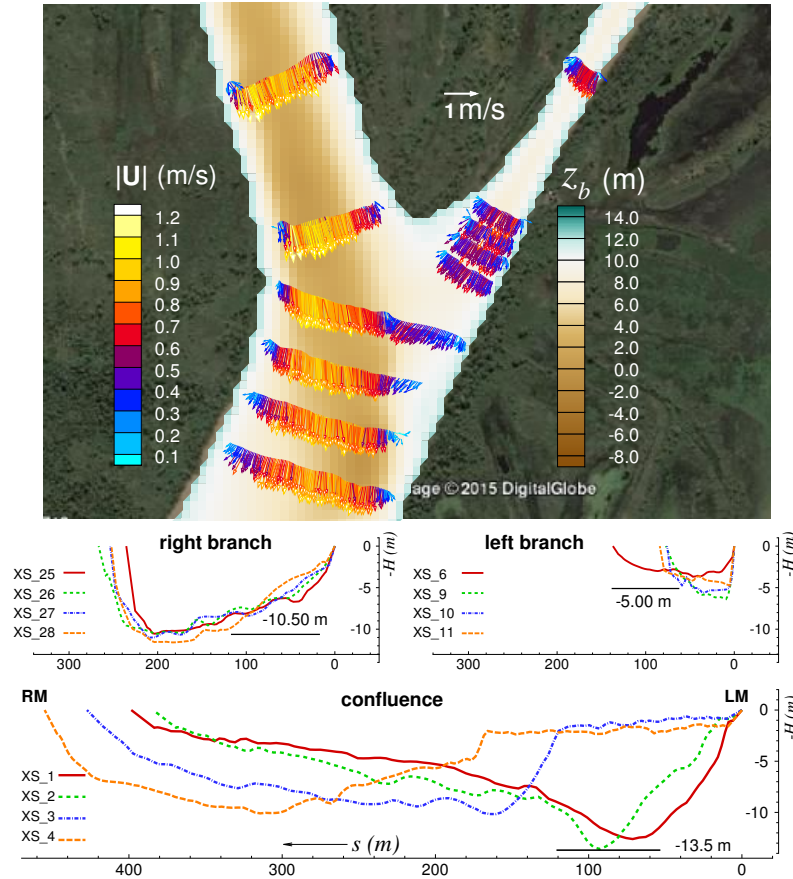
FIGURE 3.3: Top: depth-averaged velocity vectors (U, V) along the transects at the 'Las Gallinetas". Bottom: cross-sections of upstream branches and downstream confluence. Distance decreases from right (RM) to left (LM) margins, so view agrees with the satellite imagery.

The flow separates ahead of the vegetated bar, and downstream the junction between XS_4 and XS_1 and the outer edges of the faster flow core and the riverbanks. It is within the fast unmixed core of water flowing along the gently curved right branch where cross-flows are prone to develop.

3.2.3 ADCP data

On one hand, the intrinsic working principles of an ADCP (Sontek, 2004; TRDI, 2007) and users experience helped to establish guidelines for safe field practices (Muste et al., 2004; Szupiany et al., 2007; Parsons et al., 2013). Thus, besides following them and keeping the best possible control of boat speed and orientation (Table 3.3), the ADCP was set up in water mode 1 with a 0.25 m bin size and a sampling frequency of one ensemble every 0.59 s. Then, the distance from the water surface to the first cell center was about 0.6 m.

On the other hand, the post-processing procedure adopted here involves two steps: first the use of proprietary software and then an in-house code. The in-house code gets the sought cross-velocity field onto a given cross-section. The proprietary program *WinRiver* II exports 3D flow data into spreadsheet files written in ASCII format (TRDI, 2007). A fortran 95-based program called *read_aDcp* loads then the ASCII files for further processing and visualization.

In summary, the methodology bases the flow velocity projection in the following step-by-step procedures: *i)* filtering raw ensembles (a vertical profile with n_z^i bins each filled with sampled velocities and backscatter intensity, and all referenced with respect to true earth coordinates), *ii)* transforming geographical coordinates into TM coordinates (with the Snyder (1987) formulae), *iii)* computing flow discharge trough each transect and reversing it if necessary, *iv)* finding the best cross-section fit to all transects, *v)* averaging the flow velocity with all transects data, *vi)* projecting the flow velocity, and *vii)* computing the Rozovskii rotation.

3.2.3.1 Filtering raw ensembles

Several filters are run first to improve the ADCP data quality. A moving platform separates successively sampled ensembles by some distance function of the boat speed. However, depending on the sampling frequency of the dGPS RTK and the boat speed, two or more successive ensembles may be spatially coincident. Moreover, some of these positional coincidental raw ensembles may include different cells with wrong readings. Thus, for each transect, the filter stripes bad echoed data and averages those sharing the same recorded position geographically. In turn, it averages the water depth with the number of good readings (one, two, three or four out of four emitted beams). With this filtering, positional repeated data are averaged, and missing data are filled rather than interpolated.

3.2.3.2 Transforming coordinates

The ADCP automatically georeferences the velocity components and backscatter intensity during data collection. First, the magnetic declination bias reconciles the internal compass readings of the ADCP with the dGPS true earth coordinate system. Then, it is straightforward to compute the Gauss-Krüger official TM coordinates in Argentina from the geodetic readings of the dGPS RTK. The South latitude and West longitud are converted to rectangular x (positive towards *East*), and y (positive towards *North*) with the aid of the expansion given by Snyder (1987) (p. 61). The *up* z coordinate remains

FIGURE 3.4: Schematic representation of the moving platform surveying procedure.

invariant. The origin of the Gauss-Krüger coordinates is the intersection of the South Pole with the central meridian of each band, with a zero northing.

3.2.3.3   Computing river discharge

If when transversing two reciprocal transects the boat path $\partial\Omega$ encloses a region Ω, parameterized by the unit tangent $\mathbf{t}^+$ and the unit normal $\mathbf{n}^-$ vectors (Figure 3.4)

$$
\begin{aligned}
\mathbf{t}^+ &= (t_x, t_y) \equiv (\delta x/\delta s, \delta y/\delta s) \\
\mathbf{n}^- &= (-t_y, t_x) \equiv (-\delta y/\delta s, \delta x/\delta s) \ ,
\end{aligned}
\tag{3.1}
$$

a simple relation for the mass continuity can be derived.

In the absence of sources, the mass conservation constraint for a steady shallow 2DH flow $\mathbf{U_m} = (U, V)$ and thickness H reads $\nabla \cdot H\mathbf{U_m} = 0$. The integral form of the equivalent outward flux of $H\mathbf{U_m}$ yields the sought river discharge $\tilde{Q}$ through either transect (zero fluxes at the riverbanks)

$$
\tilde{Q} = \int_{\partial\Omega} (H\mathbf{U_m}) \cdot \mathbf{n}^+ \ ds
\tag{3.2}
$$

$$
\simeq \sum_{i=1}^{n_e^j} (UH\,t_y - VH\,t_x)_i \ \frac{(\Delta s_{i-1} + \Delta s_i)}{2} \ ,
\tag{3.3}
$$

where ∇ refers to the plannar nabla operator, n_{e_j} the number of ensembles measured along transect T_j, Δs_i the separation distance between two consecutive ensembles with Δs_0 and Δs_{n_j}, the specified user distance from both riverbanks to the first and last measured ensemble, respectively, and $\mathbf{U_m} \cdot \mathbf{n}^+ = U_n$ the outward normal velocity of the depth-averaged flow. The $\mathbf{t}^+$ points in the increasing arc-length (s^+) direction when traversing the transect in the counterclockwise direction, and a 90° counterclockwise rotation of it yields $\mathbf{n}^-$ such that $\mathbf{n}^+ = -\mathbf{n}^-$.

At one point, the internal computations of *read_aDcp* determines the number n_z^i of active depth cells scanned by the ADCP in each water column. Then, if (u, v, w) are the velocity components at the barycentric point (x, y, z) of each depth cell, the adopted depth-averaged flow is

$$U_i = \frac{\sum_{k=1}^{n_z^i} u_k}{n_z^i + 1} \quad , \quad V_i = \frac{\sum_{k=1}^{n_z^i} v_k}{n_z^i + 1} \; . \tag{3.4}$$

The above arithmetic mean results from imposing the no-slip condition at the river bed without correction for the bottom layer thickness (Morell et al., 2014).

The approximations for inferring the nearest surface, bed, and riverbanks flow velocities differ considerably from the one-sixth power-law and the ratio interpolation methods embedded in the proprietary software (TRDI, 2007). The proprietary code delivers in turn the discharge Q. Nevertheless, computations of $\tilde{Q}$ and Q across all transects depicted in Figures 3.2 and 3.3 shows $\tilde{Q}$ is, on average, 1.2% off from Q with a fractional standard deviation of 4.1 %.

Such way of computing $\tilde{Q}$ is relevant for four reasons:

1. to check the consistency of results produced by the proprietary software and the actual methodology,

2. to enforce the correct handling of the unit vectors $\mathbf{t}^+$ and $\mathbf{n}^-$, which are the base of the proposed scheme to project the cross-flow components,

3. to set the proper orientation of the actual transect ($Q < 0$ when surveying data from left to right banks when looking downstream or $Q > 0$ in the opposite case). Reversing data for the latter case correctly locates both banks,

4. to apply the Rozovskii method, for which (3.4) is critical.

3.2.3.4 Finding the best cross-section fit

Repeat transects surveyed along a ray drawn in advance from a virtual center of curvature usually oscilate around the line representing the optimal cross-section (Figures 3.1).

The scanning of any cross-section n_t times yields n_{e_j} ensembles along each transect T_j. The mean line $T_m(ax + b = y)$ fitting the 2D set $\{x_k^j, y_k^j\}_{k=1}^{n_{e_j}}$, for all $j = 1, \ldots, n_t$, that
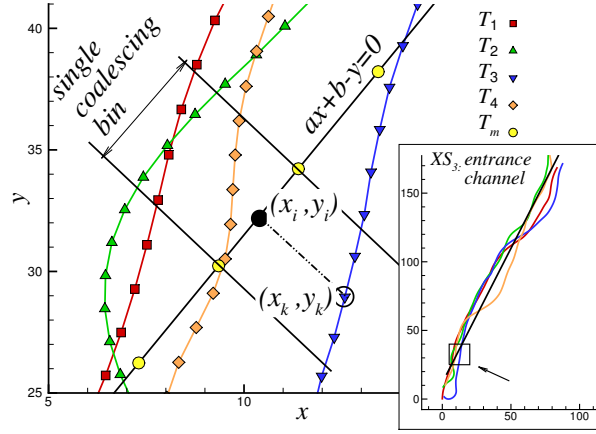
FIGURE 3.5: Orthogonal linear regression of all T_j along XS_3 (inset). The procedure *read_adcp* coalesces those ensembles from each T_j lying in a single averaged bin.

minimizes the orthogonal distance function

$$D(a,b) = \sum_{j=1}^{n_t} \sum_{k=1}^{n_{e_j}} \left(x_i^j - x_k^j\right)^2 + \left(y_i^j - y_k^j\right)^2 \tag{3.5}$$

assumes that both $\{x_k\}$ and $\{y_k\}$ are affected by equally random positional errors.

Ignoring the superscript j from now on, any equation of the form $y' = -x/a + b'$ is necessarily orthogonal to the sought regression line. If this second line passes through the data point (x_k, y_k), these two lines intersect at the point (x_i, y_i) (Figure 3.5) satisfying

$$x_i - x_k = \frac{aL_k}{1+a^2} \quad , \quad y_i - y_k = -\frac{L_k}{1+a^2} \tag{3.6}$$

where

$$L_k \equiv y_k - (ax_k + b) \; . \tag{3.7}$$

The substitution of (3.6) in (3.5) yields

$$D(a,b) = \left(1+a^2\right)^{-1} \sum_{k=1}^{m} L_k^2 \; , \tag{3.8}$$

which is a generalization of the ordinary least squares method by the factor $\left(1+a^2\right)^{-1}$. Above, $m = \sum_{j=1}^{n_t} n_{e_j}$ is the total number of ensembles associated with T_m.

The condition for an extreme of D is obtained whenever $\partial D/\partial a = \partial D/\partial b = 0$, which comes down to a quadratic equation for a whose two solutions represent a minimum and a maximum of D. The corresponding lines are orthogonal to each other, and the proper one must be used to get the slope of the so-called *Deming regression line*.

3.2.3.5 Averaging the flow velocity

Firstly, the adopted procedure links all ADCP data to the bed elevation model $z_b = z_b(x, y)$ constructed from bathymetry data (Figures 3.2 and 3.3). Therefore, each depth cell in which the device averages the collected data later is referred to the elevation above datum using $z_k = z_w - z_k^\star$. Here, z_w is the free-surface elevation above datum, and $z_k^\star$ is the local depth of the *kth* cell (Figure 3.6). The later results after using $z_k^\star = t_d + b_d + (k - 1/2)\Delta z$ for all $k = 1, \ldots, n_z^i$, where t_d, b_d, and Δz are the transducer draft, the blanking distance, and cell size, respectively, and the superscript "i" refers to the ith ensemble along the T_j transect.

Secondly, the processing of the ADCP data uses a coalescing technique without any interpolation whatsoever. A bin value, n_{bin}, must be defined first, preferably an odd number equal e.g. to 3 which means that the central, left, and right ensembles coalesce into a single bin (Figure 3.5). In brief, n_{bin} ensembles come together from each transect T_j to form a larger group of data cells at each depth cell. If each T_j contributes on average with 180 ensembles, the mean transect T_m will have about 60 coalescing bins, referred as n_b.

The averaging counts on a double bookkeeping procedure, one "dissipative" that works on globally-grid coordinates, and one "conservative" that projects on local ones. The first relies on the coalesced matrix e_n, an integer matrix that stores the coalescing bin number of T_m where each ensemble from each transect projects onto. Then, summing all well-echoed data shapes the integer matrix m_{vel}, which counts the ith ensembles of each T_j that coalesces onto the e_nth bin of T_m. Finally, m_{vel} contracts to the matrix n_{occ} required for the final averaging. The matrix n_{occ} stores how many depth-cells come together into each coalescing bin for the final averaging. As the procedure progresses, information is lost since it adds cell data one by one. In more detail, the averaging goes through three different programming blocks:

a. "Dissipative" bookkeeping algorithm

1. **input** (v_e, v_n, v_u) *w.r.t. ENU* coordinates,

2. **set** all arrays $= 0$,

3. **forall** $j = 1 : n_t,\ i = 1 : n_e(j),\ k = 1 : n_z$

    $\rightarrow$ **retrieve** $e_n = e_n(i, j)$,

    $\rightarrow$ **if** $(\neq\ bad\_echoe) : (\overline{v}_e, \overline{v}_n, \overline{v}_u) = \sum(v_e, v_n, v_u)$

    $\rightarrow$ **add** $m_{vel}(k, e_n, j) = m_{vel}(k, e_n, j) + 1$

4. **contract** m_{vel}

$\quad \rightarrow n_{occ} = \sum(m_{vel}, dim = 3)$

$\quad \rightarrow l_{vel} = \sum(m_{vel})$

5. **average** $\rightarrow (\bar{v}_e, \bar{v}_n, \bar{v}_u) = (\bar{v}_e, \bar{v}_n, \bar{v}_u)/n_{occ}$

Figure 3.6 shows a strip of n_{occ} obtained after surveying an XS with four transects. Each column represents a coalescing bin and each row the depth cells set up at the beginning of the field work. The number of contributing depth-cells diminishes towards the edge of the overlapping transects. Whenever the argument *dim* is present in the contraction expression $\sum(array, dim)$, the result is the summation of all elements values of *array* along dimension *dim*.

On the contrary, the "conservative" bookkeeping preserves each single depth cell data from each ensemble and averages them all at once. It relies on the matrix i_{T_m} that stores how many ensembles from each T_j coalesces onto the jth bin, and the matrix n_{vel} that stores the ensemble number of each T_j that coalesces onto the jth bin. In detail, the conservative bookkeeping procedure amounts to:

b. "Conservative" bookkeeping algorithm

1. **set** all arrays $= 0$,

2. **forall** $i_{xs}=1{:}n_t$, $j=1{:}n_b$, $i=1{:}i_{T_m}(j, i_{xs})$, $k=1{:}n_z$

$\quad \rightarrow$ **retrieve**

$\quad\quad\quad \rightarrow l$: cumulative # of ensembles,

$\quad\quad\quad \rightarrow e_n = n_{vel}(i, j, i_{xs})$, **if** ($\neq$ *bad_echoe*)

$\quad\quad \rightarrow$ **then** $(u_t, u_n)|_{(k,l,j)} = \mathbf{Q}(v_e, v_n)^{\mathrm{T}}|_{(k,e_n,i_{xs})}$

$\quad\quad \rightarrow$ **set** $i_{scat}(k, l, j) = 1$

3. **contract** i_{scat}

$\quad \rightarrow n_{scat} = \sum(i_{scat}, dim = 2)$,

$\quad \rightarrow l_{scat} = \sum(i_{scat})$

4. **contract & average** (u_t, u_n)

$\quad (\bar{u}_t, \bar{u}_n) = \sum(u_t, u_n, dim = 2)/n_{scat}$
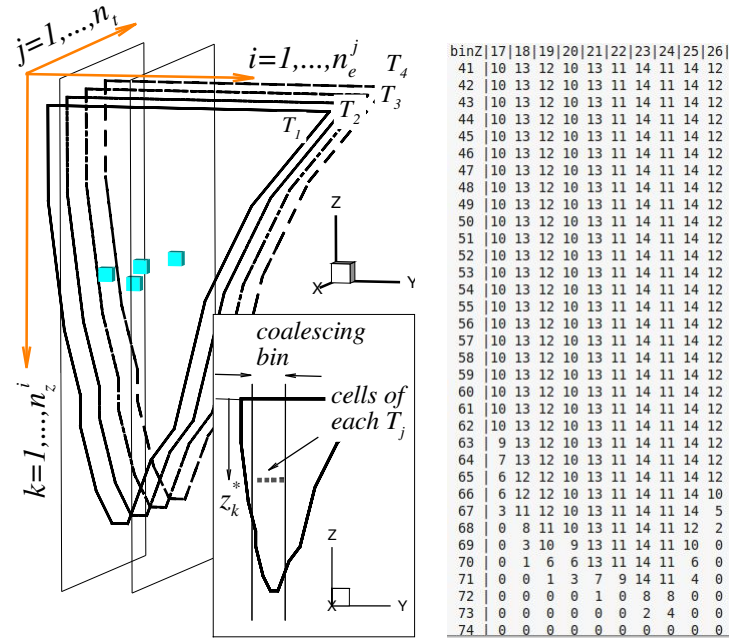
FIGURE 3.6: Left: schematic of four transects with cells at same depth albeit laterally displaced (see inset). Right: a sample of the integer matrix n_{occ} showing the number of coalescing data contributing to the final average.

Above, $\mathbf{Q}$ is a projection matrix to be defined next, and (u_t, u_n) the tangential and normal components of the projected velocities of each cell onto each bin of T_m. The superscript$^{\mathrm{T}}$ denotes the transpose of the vector (v_e, v_n). In the end, both bookkeeping must coincide:

c. Cross-check

1. **if** $(l_{vel} \neq l_{scat}) \rightarrow$ **stop**.

2. **if** $(n_{occ} \neq n_{scat}) \rightarrow$ **stop**.

3. **if** $(\overline{u}_t, \overline{u}_n) \neq \mathbf{Q}(\overline{v}_e, \overline{v}_n)^{\mathrm{T}} \rightarrow$ **stop**.

The average of the up-component, v_u, is only computed with the first bookkeeping algorithm, and it does not require any further manipulation.

3.2.3.6   Projecting the flow velocity

In the previous chapter shows that when the ADCP data, collected with a moderated boat path departure from a straight radial cross-section, projects orthogonally onto it the mean relative deviation is utmost 4 %. Accordingly, the actual procedure relies on the following assumptions: i) the surveyed transects are as close as possible to the local

optimal radial plane, *ii*) the projected data lies on a plane that best fit the surveying boat paths, and *iii*) the error in the Rozovskii method indicates how to extract the crossflow.

The first premise depends on well-planned fieldworks (Figure 3.1) and the second on minimizing (3.8). Finally, if (t^+, n^-) points in radial and azimuthal directions in terms of a local polar system, respectively (Figure 3.4), the Rozovskii crossflow component v_s reads (Chapter 2):

$$v_s = \frac{U_n}{|\mathbf{U}|} u_t^{hel} + \frac{U_t}{|\mathbf{U}|}(U_n - u_n) \ . \tag{3.9}$$

Here, u_t^{hel} strictly refers to the helicoidal part of the crossflow velocity, (U_t, U_n) the 2DH velocity components, and $|\mathbf{U}|$ its modulus.

The expression establishes that the helical crossflow component points in the opposite direction, and it is proportionally affected by the excess or deficit of the streamwise component with respect to its 2DH value. To reconcile things it suffices to project the velocity data on the tangent plane and to remove the 2DH value of the u_t-component.

Mathematically, a vector projection is always a vector though in engineering aplications usually means its magnitude. Thus, the projection of the column vector $\mathbf{u} = (v_e, v_n)^{\mathrm{T}}$ on the line generated by the vector $\mathbf{n}$, with norm $\|\mathbf{n}\|^2 = \langle \mathbf{n}, \mathbf{n} \rangle$, is the vector $c\mathbf{n}$ for some scalar c. Now, the difference $\mathbf{u} - c\mathbf{n}$ is orthogonal to $\mathbf{n}$, so $\langle \mathbf{n}, \mathbf{u} - c\mathbf{n} \rangle = 0$, where $\langle \cdot, \cdot \rangle$ is the inner product between two vectors. Solving for c and using elementary linear algebra, the isolated crossflow helical component becomes

$$\mathbf{u_t^{hel}} = \left(\mathbf{I} - \frac{\mathbf{n}\mathbf{n}^{\mathrm{T}}}{\|\mathbf{n}\|^2} \right) \mathbf{u} - \mathbf{U_t} \ , \tag{3.10}$$

where $\mathbf{I}$ is the identity matrix and the expression between parenthesis is the matrix $\mathbf{Q}$ that projects $\mathbf{u}$ onto T_m. From (3.10), the velocity component normal to T_m is

$$\mathbf{u_n} = \frac{\mathbf{n}\mathbf{n}^{\mathrm{T}}}{\|\mathbf{n}\|^2}\mathbf{u} = \mathbf{P}\mathbf{u}, \tag{3.11}$$

such that $\mathbf{PQ} = \mathbf{0}$.

3.2.3.7 The Rozovskii rotation method

The primary v_p and secondary v_s flow Rozovskii components at elevation z are (Bathurst et al., 1977)

$$\begin{bmatrix} v_s \\ v_p \end{bmatrix} = \begin{bmatrix} sen\phi & -cos\phi \\ cos\phi & sen\phi \end{bmatrix} \begin{bmatrix} v_e \\ v_n \end{bmatrix}, \tag{3.12}$$

where ϕ is the angle of the depth-averaged velocity vector $\mathbf{U} = (U, V)$ with respect to the x-axis whenever $z_b \leq z \leq z_w$ (Figure 3.4). Furthermore, if these velocities are projected into the normal and tangential directions along T_m, then

$$v_p^{rk} = v_p \cos(\phi - \alpha), \tag{3.13}$$

$$v_s^{rk} = v_s \sin(\phi - \alpha), \tag{3.14}$$

represents the downstream and cross-stream components, respectively, of the Rozovskii velocities after Rhoads and Kenworthy (1998b).

The derivation of (3.13)-(3.14) require the angles φ and α measured counterclockwise from the x-axis to (v_e, v_n) and T_m, respectively (Figure 3.4).

3.3   Results and discussion

Figures 3.7 depicts $\mathbf{u_n}$ and $\mathbf{u_t^{hel}}$ in terms of the globally-grid coordinates given by (3.10) and (3.11), the later isolated from any primary flow skewness effect. The vertical distribution of $\mathbf{u_n}$ is seen on a large part of XS_b as the flow approaches the sharp turn towards the Santa Fe's harbor entrance channel. A strong helical flow component is visible across XS_c, weaker on XS_d and barely present on a portion of XS_e.

Figure 3.8 illustrates the difference between (3.10) and the first of equations (3.12) by plotting the vertical distribution of the streamwise and the crosswise flow components produced with both methods on selected profiles. The larger the departure of the streamwise flow from an approximated parabolic -or log- distribution the greater the separation between both predictions.

The "dissipative" and "conservative" algorithms deliver identical averaged distributions of u_t^{hel}, indistinguishable on the bottom plot of Figure 3.8. The scatter points represent depth cells contributing to a single coalescing bins, namely profiles 27, 29, and 39. The top plot only depicts every other vertical profile among the final 41 averaged bins that define the mean transect T_m of XS_c on the entrance channel. Similar blanking criteria were used in the following figures to avoid vector cluttering.

Despite Rhoads and Kenworthy (1998b) best efforts to cure the intrinsic deficiencies of the Rozovskii scheme, the extra rotation (3.14) is insufficient to remove completely the streamwise flow component blended into u_t^{hel}. To make sure this is the case, Figures 3.9 and 3.10 plot the vertical bidimensional (2DV) distribution, in the (t, z) plane, of the vector fields $(u_t, 0), (u_t^{hel}, 0)$, and $(v_s^{rk}, 0)$. The fourth plot starting from above depicted the net difference between the proposed projection of the crossflow component and
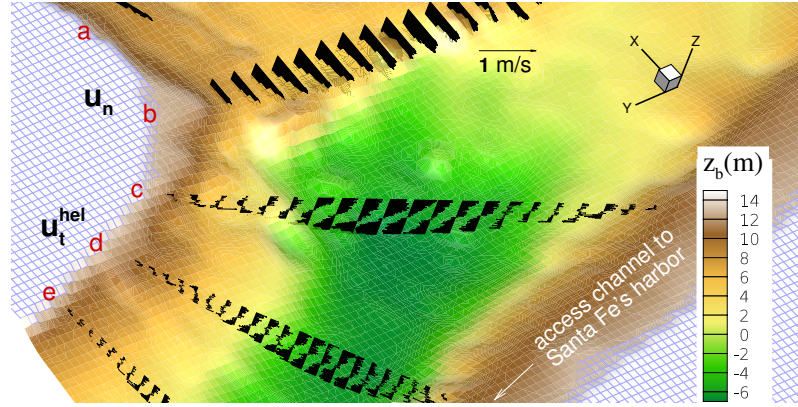
FIGURE 3.7: Projection of $\mathbf{u_t}$ (and $\mathbf{u_n}$) on global-grid coordinates, and isolated from primary flow skewness effects.

Rozovskii, corrected after Rhoads and Kenworthy (1998b), $u_t^{hel} - (v_s^{rk})$. The last plot contains the spatial coverage of the pointwise fractional deviation

$$\delta_{k,j} = \frac{|(u_t^{hel})_{k,j} - (v_s^{rk})_{k,j}|}{(\bar{u}_t^{hel})_j} \quad , \quad k = 1, \ldots, n_z^j \ , \tag{3.15}$$

where $\bar{u}_t^{hel}|_j$ represents the average of the absolute values of u_t^{hel} on the jth profile

$$\left(\bar{u}_t^{hel} \right)_j = \frac{1}{n_z^j} \sum_{k=1}^{n_z^j} |u_t^{hel}|_{k,j} \quad , \quad j = 1, \ldots, n_b \tag{3.16}$$

Equation (3.15) takes u_t^{hel} as a reference quantity, a certain assertion once (3.9) probes true. Finally, each plot exhibits either the contours of the flow modulus or the local fractional deviation in the background. The plot of Figures 3.9 and 3.10 show that the local fractional deviation between the two methods peaks well above 100 % in some areas.

The discrepancy between the outcome of the two projection procedures is similar when the fluvial setting is different. The broad and gently curved right branch of the "Las Gallinetas" confluence triggers the formation of weak secondary currents, here captured on XS_4 just downstream the junction (Figure 3.11). Again, the local fractional deviation is about 50 % in vast parts of the cross section and above 100 % in the upper and lower flowing layers.

The magnitude of $\delta_{k,j}$ signals the limitation of the Rhoads and Kenworthy (1998b) projection to annihilate the inherent deficiency of Rozovskii to match u_t^{hel} (Figure 3.8).

A curved open-channel flow develops helical flow directed radially outward (inward) near the upper (lower) layers of the flow (Engelund, 1974). The radially positive direction is
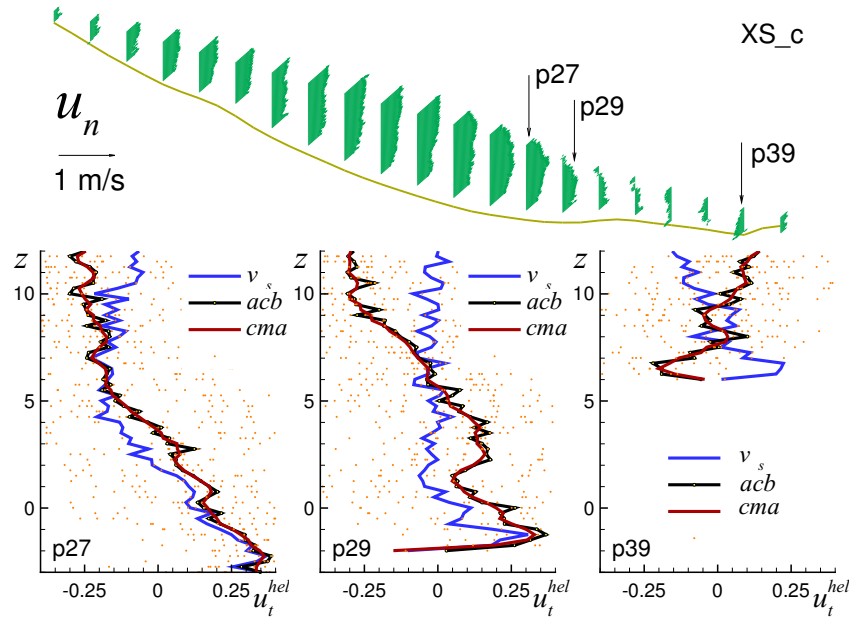
FIGURE 3.8: Top: normal flow component on XS_c. Bottom: reversed v_s and u_t^{hel}, the later as scatter cells (in orange), as average of the coalescing bins (:*acb*, in black), and as center moving average of *acb* (:*cma*, in red).
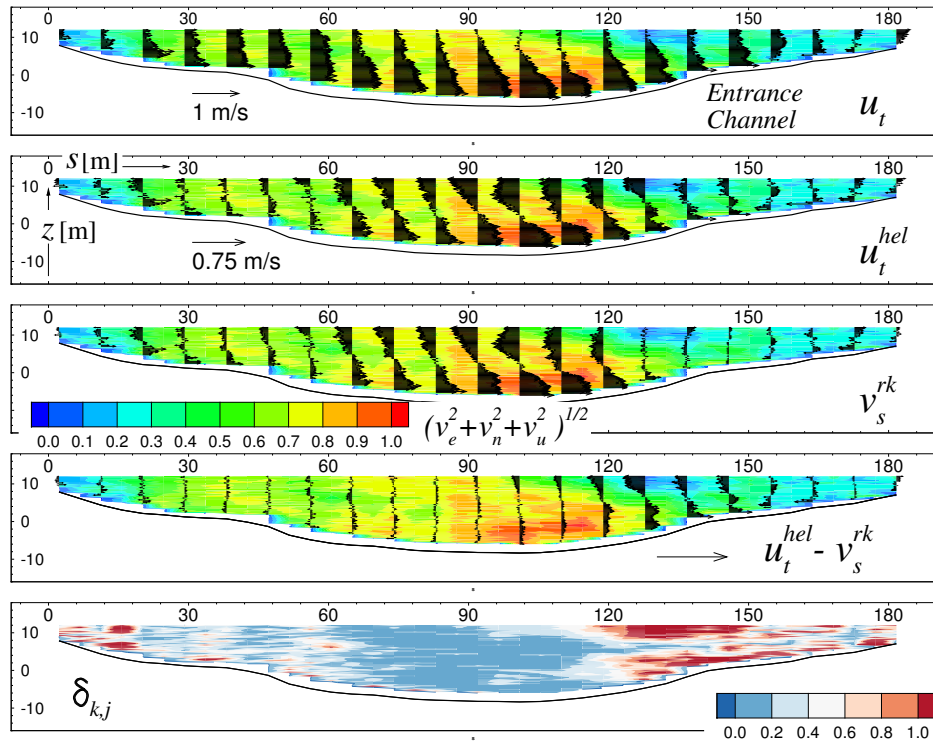
FIGURE 3.9: Crossflow on XS_c at the Access Channel. From top to bottom: u_t, u_t^{hel}, v_s^{rk}, $u_t^{hel} + v_s^{rk}$, in ms^{-1}, and $\delta_{k,j}$.
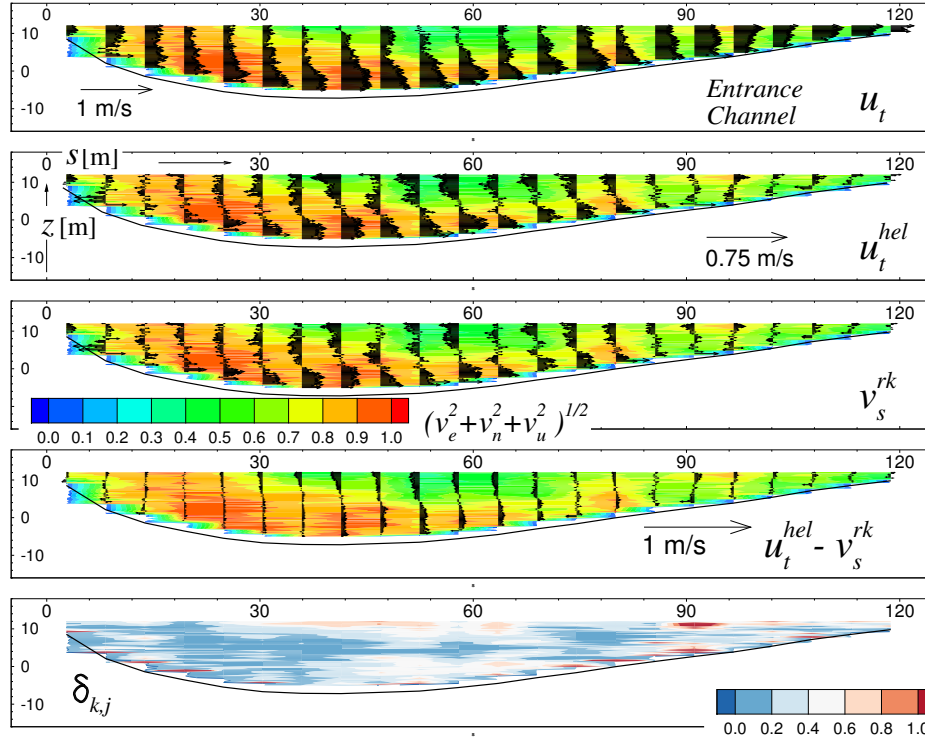
FIGURE 3.10: Crossflow on XS_d at the Access Channel. From top to bottom: u_t, u_t^{hel}, v_s^{rk}, $u_t^{hel} + v_s^{rk}$, in ms^{-1}, and $\delta_{k,j}$.

away from the virtual center of curvature. Figures 3.9-3.11 show a straight application of Rozovskii in tune with (3.9).

Leschziner and Rodi (1979) recognized the outcome of Rozovskii as representing the excess (or deficit) of the radial velocity component relative to the 2DH value. A claim later repeated by Boxall et al. (2003).

Any observer based on mechanistic considerations may judge that the Rozovskii component is enough to capture the proper magnitude of the crossflow. However, in some cases the Rozovskii component is not only insufficient to capture the strength of the secondary current but also inaccurate as the error plots of Figures 3.9-3.11 demostrate. It adds a non-trivial error term all over the water depth, albeit zero on the average.

3.3.1 Identification of Rozovskii elemental error

To expose the error nature of the Rozovskii scheme, Figure 3.12 deploys on the left the two terms of which (3.9) is made of and on the right the straight computation of (3.12), first equation. It is worth to mention that u_t^{hel} and u_n are the basic supply of (3.9), in turn computed with (3.10) and (3.11), respectively, albeit projected onto the cross plane. The composite velocity matches exactly the Rozovskii decomposition deployed in Figures 3.8 and 3.11, profiles 27 and 20, respectively.
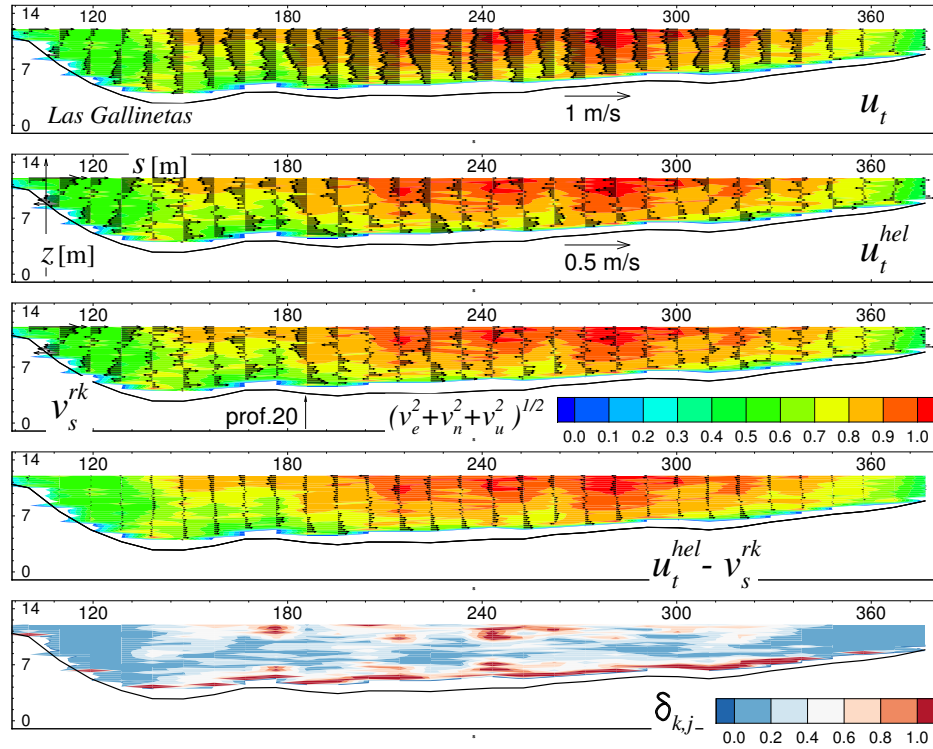
FIGURE 3.11: Crossflow on XS_3 at "Las Gallinetas". From top to bottom: u_t, u_t^{hel}, v_s^{rk}, $u_t^{hel} + v_s^{rk}$, in ms^{-1}, and $\delta_{k,j}$.

The remarkable agreement depicted in Figure 3.12 between the composite expression (3.9) and the Rozovskii raw decomposition, equation (3.12), works as a double cross-checking. One one hand, it ascertains the inherent correctness of u_t^{hel}, both operationally when computed with (3.10), and theoretically since (3.9) relies on decomposing the cross-flow as $u_t = u_t^{hel} + U_t$ (Johannesson and Parker, 1989b; Blanckaert and de Vriend, 2004). On the other hand, and besides reversing u_t^{hel}, it shows that Rozovskii adds an error along the vertical proportional to the excess (deficit) of the streamwise flow velocity component with respect to its depth-averaged value.

3.4 Conclusions

It has long been assumed that whenever the Rozovskii method takes the correct orientation of the cross-stream plane, it computes the excess (or deficit) of the cross-component of flow velocity relative to its respective depth-averaged value. Nevertheless, many researchers acknowledged certain ambiguities when deciding the orientation of the cross-channel plane that defines the downstream and the cross stream component. Rhoads and Kenworthy (1998b) supposedly circumvented this shortcoming of the Rozovskii procedure by projecting their field data onto fixed cross-sections. However, their
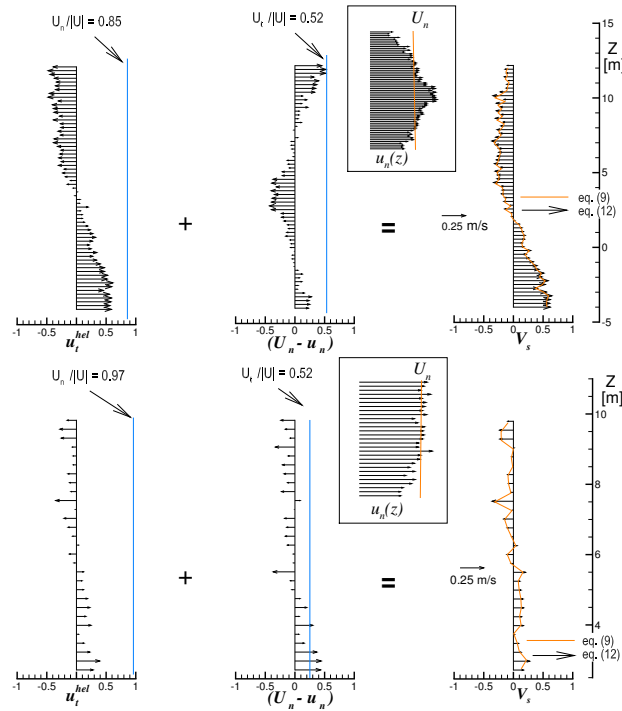
FIGURE 3.12: The Rozovskii projection as a composite of information from its two sources. Top: profile 27 on XS_c at the access channel. Bottom: profile 20 on XS_3 at the "Las Gallinetas" confluence. The horizontal axis is just for referencing the scale factors $(U_n, U_t)/|\mathbf{U}|$.

contribution initiated a controversy that continues to the present days. For that reason, the questioning of the Rozovskii method was of substantial interest in this work.

To test the Rozovskii method, an algorithm based on global coordinates to extract the helicoidal component from 3D raw ADCP data, and then projected to a local cross plane has been developed. The proposed methodology frame the data collected from moving platforms in exactly the same way observers collect their data from fixing frames with static devices.

Contrary to most published works, the proposed procedure relies on a double bookkeeping algorithm that coalesce ADCP neighboring cells data without resorting to any interpolation routines. Both bookkeeping procedures yield identical results, which helped to validate the developed tool for processing field data Then, the inherent deviation of the Rozovskii original rotational scheme was tested with field data coming from two different fluvial settings, one characterized by an aspect ratio $\beta \simeq 13$, and the other by $\beta \simeq 75$.

It has been established that despite the capability of the method to project helical crossflow-looking distributions, its outcome is distorted by a source term that depends on the streamwise velocity. Previous theoretical results predict this peculiar way of

projection by the Rozovskii method, now confirmed on experimental grounds. The extra projection of Rhoads and Kenworthy is not enough to remedy this inherent deficiency.

The error source term is zero once averaged over depth, and it is multiplied by a scale factor that depends on the mean crossflow intensity, $U_t/|\mathbf{U}|$. Consequently, whenever the skewness of the depth-averaged primary flow is small, the added error is eventually not significant, which may explain the longstanding success of the method among practitioners and researchers.

The Rozovskii procedure is, however, simple and powerful enough for a quick detection of secondary currents in river bends and confluences. Nevertheless, the method indeed mixes what it pretends to isolate, which is a pure helical crossflow component dissociated from the streamwise component. As such, it is no more than a quick tool for diagnosing the presence of secondary currents in river bends or confluences.

Chapter 4

Flow pattern at a river diffluence at the alluvial system of the Paraná River

This chapter presents field and numerical data depicting the flow pattern formed at a diffluence of the Colastiné River, Argentina, where one branch accesses the local harbour. The harbour has been in decline since the 1970s due to costly maintenance dredging of the access channel. The objective of this work is thus twofold: to show the persistence of the flow pattern developed at the diffluence despite recent morphological changes seen at the site, and to test a possible solution to the access channel sedimentation problem. Knowledge gained during the execution of the study helped to validate a code developed to process field data captured with two acoustic Doppler current profilers (ADCPs). The results confirm that both branches are prone to developing secondary currents. Simulations show that an engineering intervention downstream of the bifurcation can establish a self-dredging flow reversal along the access channel, turning the actual diffluence into a confluence.

4.1   Introduction

Santa Fe City is located 476 km northwest from Buenos Aires. The city was declared "Puerto Preciso" during the Spaniard rule, forcing all ships sailing the Paraná River to stop by on their way to or from Asunción, Paraguay. It is the furthest inland harbour within Argentina for oceanic vessels. It was moved several times since the city foundation in 1573. In 1886, the city located its harbour on the Colastiné River and moved it further upstream to a new site in 1890 (pts. (a) and (b), respectively, Figure 4.1). Both sites

were flood-prone lowlands. Therefore, an enhanced harbour surrounded by higher lands was built between 1907-1910, on its current location (pt. (c), Figure 4.1).

An access channel was excavated to link the port with the main channel of the Paraná River. The flow expansion created at the bifurcation between the access channel and the Colastiné River outlet induced a continuous sedimentation of the sands carried in suspension, requiring out periodic maintenance dredging of the external reach of the access channel, behind the recently formed mid-channel island (Figure 4.1). The harbour has been in decline since the 1970s due to this additional dredging cost. The situation did not change much with the privatization of the fluvial waterway that links Santa Fe with the Atlantic Ocean through the Paraná and the La Plata rivers. Whereas ships sailing along the waterway pay a toll to the concession company in charge of the maintenance dredging (Lievens, 1997), the cost of having the access channel fully operational is still local matter.

In 1998 studies began to find a new place for the Santa Fe harbour, this time on the main channel of the Paraná River (FICH, 1998). Nevertheless, there is a simple solution to the long standing sedimentation problem of the access channel mouth that has not been tested so far. It is technically feasible to sustain a bed shear stress distribution well above the sedimentation threshold values for sands by reversing the flow direction along the access channel (by closing the mouth of the South Derivation Channel, right next the access channel heading (pt. (d), Figure 4.1)).

The hydrodynamics of the study site is also of significant scientific interest in its own right. Diffluences can steer flow and sediment to either branch controlling the morphological development of the downstream channels (Federici and Paola, 2003). Nonetheless, the development of the downstream branches is achieved through a series of interacting processes that are still poorly understood (Pittaluga et al., 2003; Kleinhans et al., 2008). Moreover, if the planar turn of the bifurcation is sharp enough, cells of secondary circulations may develop in response to the mechanical imbalance between the local elevation of the free surface and the centrifugal force induced by channel curvature. The formation of cross-flow is thus possible if the diffluence branches act as river bends. Whereas this response can be expected in Y-shaped diffluences (Dargahi, 2004), it is far from being evident in T-shaped diffluences. In the latter case, the flow should exhibit regions of acceleration and deflection, with eventual zones of separation and reattachment with a central core of fluid moving along curved streamlines (Miori et al., 2012). Thus, the region of convectively accelerated flow should be close to the typical hydrodynamics behaviour seen along any river bend. Under these circumstances, the abundant theoretical (Rozovskii, 1957; Engelund, 1974; Johannesson and Parker, 1989a) and experimental

research (Bathurst et al., 1979; Dietrich and Smith, 1983) developed for open-curved flows may carry over to the study of diffluences with sharp turns.

The single cell of secondary currents usually found in flumes and in rivers scales with channel width B and water depth H, whose behaviour depends on the aspect ratio $\beta = B/H$ (Yalin, 1992). Rozovskii (1957), Blanckaert and de Vriend (2004), and Kashyap et al. (2012) studied bends in flumes with aspect ratios of 13.33, 3.6, and $5.0 - 12.5$, respectively. However, there exists few field studies to date detailing the structure of helical flows driven by centrifugal forces.

Table 4.1 compiles values of β resulting from the field studies collected by Bathurst et al. (1979) in the river Severn (UK), by de Vriend and Geldof (1983) in the river Dommel (The Netherlands), by Dietrich and Smith (1983) in the Muddy Creek (USA), and by Dinehart and Burau (2005) in the Sacramento river (USA). For the sake of comparison, data taken by Richardson and Thorne (2001) at the Brahmaputra-Jamuna River (Bangladesh), and by Szupiany et al. (2009) at the main channel of the Paraná River (Argentina) are also included. These authors claimed to have detected secondary currents albeit at river confluences rather than in river bends. The field data shows that cross-flow circulation driven by curvature develops whenever $10 \leq \beta \leq 15$.

In tune with the foregoing issues, this chapter is concerned with the flow pattern developed at the diffluence of the Colastiné River when rejoining the Paraná main channel, an aim achieved through field measurements and 2D and 3D numerical simulations. The objective of this work is thus twofold: to show the persistence of the flow pattern developed at the diffluence despite recent morphological changes experienced by the site, and to test a simple solution to the chronic sedimentation problem seen at the access channel mouth.

Knowledge gained during the execution of the study helped to refine and validate a computer code developed to process field data captured with two acoustic Doppler current profilers (ADCP). Both, field and numerical results show that the two branches of the diffluence act like true river bends, and consequently are prone to developing secondary currents. Field data shows this is indeed the case along the right branch, which was the only systematically measured branch. It remains to extract the results from the open-source Telemac system (Telemac-Mascaret Modelling System, 2014), following the field data treatment, in order to assess the predictive code capability to reproduce the observed secondary currents.

The following section describes the study site and the collected data, including a brief description of the in-house software developed to treat the field data. Then, a description on how and why the right downstream branch of the diffluence acts as a river bend is

TABLE 4.1: Some field data from rivers around the world

River	B(m)	H(m)	β
Severn, UK (Bathurst et al., 1979)	12.0	0.90	13.3
Dommel, The Netherlands (de Vriend and Geldof, 1983)	7.0	0.58	12.0
Muddy Creek, USA (Dietrich and Smith, 1983)	5.5	0.50	11.0
Brahmaputra, Bangladesh (Richardson and Thorne, 2001)*	450.0	6.00	75.0
Sacramento, USA (Dinehart and Burau, 2005)	130.0	12.00	10.8
Paraná main channel, Argentina (Szupiany et al., 2009)*	850.0	15.00	57.0
Colastiné, Argentina (this study)	130.0	10.00	13.0

* *confluences*, whose hydrodynamics is not necessarily equivalent to those observed on river bends (Rhoads and Kenworthy, 1998a)

FIGURE 4.1: Location of the study site (encircled). Past, present and proposed future locations for the Santa Fes harbour (in yellow). Satellite imagery courtesy of INPE (Instituto Nacional de Pesquisas Espaciais, Brazil).

presented. Finally, a qualitative comparison between simulated results and observed cross-flow data is given next, to close with the proposed engineering solution to the access channel sedimentation problem.

TABLE 4.2: Fieldwork parameters: z_w: water stage above datum at Santa Fe harbour, Q: access channel discharge, V: vessel bin size and Δz : ADCP sampling interval

Date	$z_w(m)$	$Q(m^3 s^{-1})$	$V\ (m/s)$	$\Delta z(m)$	$\Delta t(s)$
2004[a]	11.25	856±98	0.72	0.90	10.00
2006[a]	11.51	917±101	0.67	0.50	5.00, 10.00
2007[a]	12.16	663±116	1.36	1.10	10.00
2008[a]	10.78	622±119	1.15	0.75	10.00
2009[a]	13.27	1083±126	0.65	0.90	10.00
2010[b]	12.78	1085±63	1.52	0.25	0.59
2012[b]	10.57	595±14	1.15	0.25	0.59

a.Sontek RiverSuveyor 1000 kHz
b. TRDI Ro Grande 1200 kHz

4.2   Materials and Methods

4.2.1   Study site

The incoming flow from the Colastiné experiences a sharp turn at the access channel inlet (Figure 4.2a), which makes it prone to centrifugal effects and, therefore, susceptible to developing secondary currents. Table 4.2 summarizes the main parameters either collected or setup during the fieldworks: the river discharge Q and free-surface elevation z_w corresponding to low-medium flow conditions, the vessel velocity V, and the ADCP sampling volume and time, Δz and Δt, respectively.

In the occasion of the field campaign of 2004, the existing mid-channel bar was submerged albeit the water depth was too shallow for sailing over it. On the contrary, the river stage was higher during the fieldwork of 2006 making it possible to collect data over the sand bar. Figure 4.2(b) shows the river water levels on the field trip dates, and during the Landsat imagery dates used to fill the late evolution of the riverbanks.

The field site is within the alluvial system of the Paraná River, a large low gradient sandy river with a free-surface slope ranging between 3 and 5 cm per kilometer (i.e. $[3 - 5] \times 10^{-5}$). The Colastiné is an anabranch of the Paraná River with riverbanks composed of a $4-6$ m layer of clay and silt overlying coarse sands (Iriondo, 2007). It is a typical meandering river with an approximated average water depth, channel width, and discharge of 6 m, 600 m, and 1700 $m^3 s^{-1}$, respectively. About 80-85 % of the Colastiné and Paraná sediment transport is wash load made of silts and clays barely found in measurable quantities in the bed (Amsler et al., 2005). The rest is bed-material made of fine and medium sands predominantly carried in suspension. Figure 4.2(c) depicts several particle size distribution of bed material collected at the study site. The samples

are characterized by an average geometric mean size and standard deviation $D_g = 221 \mu m$ and $\sigma_g = 1.74$, respectively.

Figure 4.2(a) summarized the morphology variations of the site in the last 100 years according to data retrieved from old navigation charts and recent Landsat imagery. The accretion rate of the wedged-shaped floodplain created between the former Colastiné course and the newly excavated access channel was about 28 m/year between the years 1913-1928. By contrast, the wedged evolved into a tongue-shaped floodplain at the slower rate of 12 m/year in the years 1928-1986 and remained stable since then. The tracked riverbanks displacements yielded an average accretion rate of 19 m/year for the head of the mid-channel island while the "horizontal bar" of the original T-shaped diffluence has remained almost unchanged since 1913, with an accretion rate of 4 m/year at most. The formation of the tongue-shaped right floodplain was part of larger scale processes attributed to the climate variability of the twentieth century (Amsler et al., 2005).

Consequently, there seems that whereas the riverbanks experienced a long-term adaptation processes, the recent growth of the mid-channel island formed at the bifurcation obeys short-term processes. The rapidly evolving mid-channel island conforms with the local divergent planform of the diffluence. Recent changes in the Colastiné hydrology could have contributed to the island formation. The mean channel width along the Colastiné has decreased an average of 16-21 % in the years 1977-2009 in response to a mean river discharge decline of about 16-26 % (Amsler et al., 2005; Ramonell, 2012). If the mid-channel island formation is the result of the sudden loss of the river transport capacity at the bifurcation, to the river changing hydrology, or a combination of both is beyond the scope of this work. Resolving these processes imply having data across a wide range of spatial and temporal scales, an extremely difficult task due to the required resources as well as the need to count with an accurate record of topographic data.

The typical one-dimensional (1D) description of a river bifurcation consists of three branches linked through a node. In this context, the bifurcation angle is defined by the centerlines of the two downstream branches relative to the upstream channel orientation ($\gamma = \gamma_a + \gamma_b$, Figure 4.2(d)). Figure 4.2(d) sketches the tracked morphology evolution of the bifurcation node since 1913. The newly excavated access channel created a Y-shaped diffluence of the Colastiné River with an initial bifurcation angle $\gamma \simeq 152°$. With time, the Colastiné swiftly moved south towards its current morphology accompanying the evolution of the main channel of the Paraná itself (Amsler et al., 2005). By the mid 1980s, the bifurcation had evolved to an almost T-shaped diffluence with an angle $\gamma \simeq 189°$. The system remained unchanged for years till the turn of the century, when the mid-channel bar formed right upstream of the diffluence eventually began to emerge.
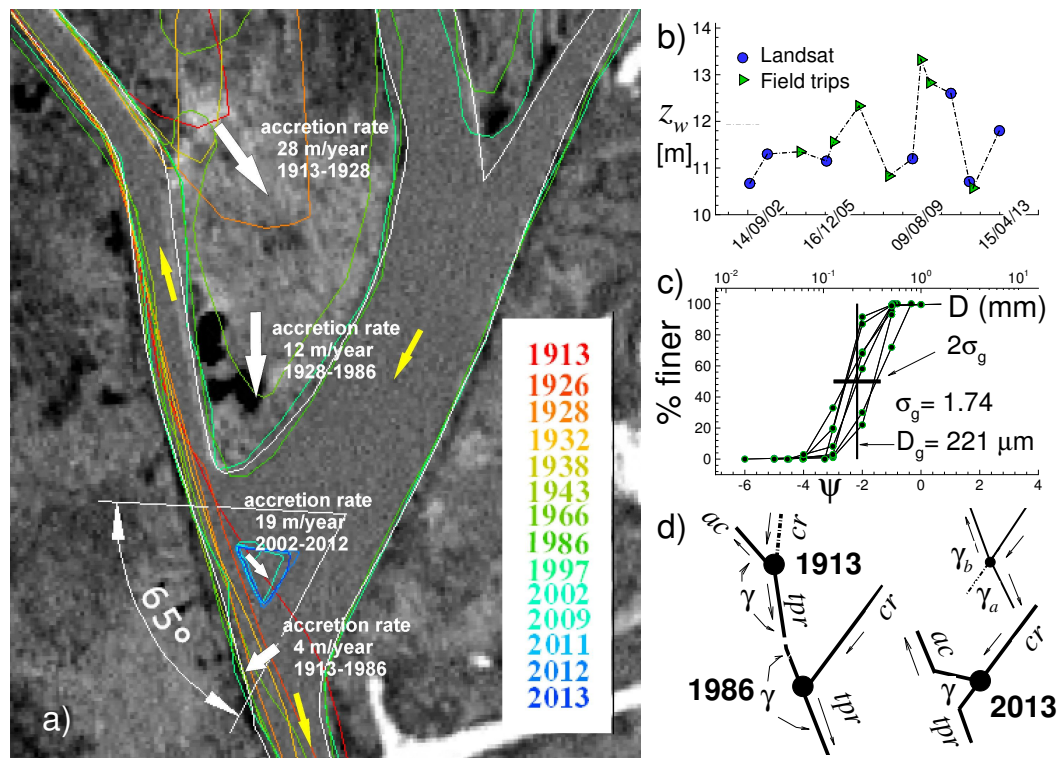
FIGURE 4.2: a) Morphological evolution of the study area, b) water levels with Table 4.2 and Landsat imagery dates, c) grain size distribution, and d) 1D evolution sketch of the bifurcation node since 1913 (*ac*: access channel, *cr*: Colastiné River, *tpr*: to Paraná River). Satellite imagery courtesy of CONAE(National Agency of Space Activities, Argentina).

The mid-channel bar remained under or above water depending on the river hydrology (Figure 4.2b). From 2008 onwards, the sandbar was colonized by vegetation and recently evolved to a mid-channel fluvial island used for livestock grazing by local inhabitants. Nowadays, the hydrodynamics diffluence is driven by the mid-channel island conforming to a Y-shaped bifurcation with a new angle $\gamma \simeq 65°$.

4.2.1.1 A note on bifurcation stability

River bifurcations behave as switches that steer the flow and sediment partitioning into the two downstream branches (Federici and Paola, 2003). Bifurcations are "stable" if both branches remain open through time, and "unstable" whenever one of the two downstream branches tends to be abandoned (Pittaluga et al., 2003). Channels upstream of stable bifurcations are straight, widening towards the bifurcation node. Burge (2006) reported that bifurcations characterized by greater angles may be inefficient for an even distribution of water and sediment between both anabranches. In contrast, bifurcations with smaller angles may remain stable by dividing water and sediment more evenly (Federici and Paola, 2003).

Even though the bifurcation seems to be stable, the external reach of the access channel (behind the mid-channel island) requires periodic maintenance dredging to keep the waterway operational. It is likely that the recent formation of the mid-channel island head that divides sediment and water into the downstream branches can also contribute to the stability of the bifurcation. The accretion rate of the mid-channel island head was about 19m/year in the period 2002-2012, reducing the former bifurcation angle γ from $189°$ to the actual $65°$, close to the stable range of $40° - 60°$ reported by Federici and Paola (2003).

4.2.2 Velocity measurements

Data captured with ADCP are routinely used to study 3D flows, and the trend is to repeat transects along linear routes to resolve weak cross-stream velocities (Dinehart and Burau, 2005). In this work, two different ADCP has been systematically used in the study site; a 1000 kHz RiverSurveyor manufactured by Sontek and a 1200 kHz Workhorse Río Grande manufactured by Teledyne RD Instruments (TRDI). The proprietary software packages *RiverSurveyor* and *ViewADP* for the Sontek ADCP, and *WinRiver* II for the TRDI ADCP were used for data acquisition and integration with positional information from satellite data. However, and due to an ongoing effort to develop a set of in-house routines to process the field data, the present work restricts the analysis regarding the 3D structure of the flow velocity to data captured with the Sontek ADCP, whereas flow discharge data analysis is limited to the TRDI ADCP measurements. A full description of the in-house codes is beyond the scope of this work.

Water velocity and bathymetry data were collected using one of the ADCP in parallel with a differential Global Positioning System (dGPS) receiver with Real-Time Kinematic (RTK) technology. The RTK system, sampling at the rate of two positional points per second, provided accuracies of $±0.02$ m in planar and $±0.04$ m in vertical direction. A second serial port to connect a digital 200 kHz Raytheon single beam echo-sounder was attached to the on-board computer during the surveys.

The down-looking ADCP was mounted on the side of a fiberglass-hull vessel of 6.4 m in length, when a combined bathymetry and flow velocity field survey were carried out using the moving boat methodology (Muste et al., 2004). For most of the field works, the Sontek ADCP was set to a cell size and sampling interval (or ensemble) of 0.75 m and 10 s, respectively, with a boat velocity preferably below 1.5 m/s to obtain reasonably accurate flow measurements (Szupiany et al., 2007). The TRDI was set up to work under water mode 1 with a bin size of 0.25 m and a sampling frequency of one ensemble every 0.59 s (Table 4.2).

Three types of single-beam bathymetry datasets were collected during the field works spanning the years 2004-2012. One set of data, designed to guide data-collection operations, corresponded to survey lines covering the study area with an approximate separation interval of 50 m each. In addition, a separate set of navigation lines, skewed to the approximately equally spaced transects, were planned to provide independent measurements of precision and bias. These skewed lines served later on as an independent basis to test the adequacy of the interpolated digital bed elevation model (DEM). A mean depth of 7 m at the navigation channel, and about 3.5 m at the outlet of the Colastiné River, with a mean channel width of 130 m and 600 m, respectively, were determined during these measurements. A scour hole with a bed elevation of -6.5 m was found on the right branch, a short distance downstream from the point of maximum curvature, in comparison with the ground elevation of about 14 m of the nearby inner bank (Figure 4.3(a)).

The third set of bathymetry data was pick-up along transects aligned with rays departing from a virtual centre of curvature, pinpointed over the land surface on the right -inner-bank side. These rays were drawn in advance to all field works, and the centre of curvature was determined by fitting a circle to the river plan-form of the inner bank. The helmsman then followed the drawn transects as closely as possible by tracking the vessel position in real-time with the dGPS. Nevertheless, in order to verify if the adopted cross-section orientations were supposedly perpendicular to the primary flow direction, two floats made with a 1.8 m long and 5 cm-diameter PVC tube and equipped with Blue-tooth GPS (Garmin 10X) were used to identify depth averaged particle paths at the sharp turn of the navigation channel inlet. Data from the GPS were logged at 2 seconds interval onto a portable computer (with enhanced Blue-tooth communication of up to 100 m reach) by using standard navigation software. The floats were released just $100 - 150$ m upstream of the Colastiné River's outlet on March 18, 2009, prior to the field survey with the TRDI ADCP.

4.2.3 Data analysis

4.2.3.1 Digital bed elevation model - DEM

The ADCP internal compass and tilt sensor (roll/pitch) referred water velocities components in terms of East-North-Up (ENU) coordinates. The collected bed elevation data in ENU coordinates, corrected by the magnetic declination bias, were later converted to Transverse Mercator (TM) coordinates with the formulas given by Snyder (1926), with the new World Geodetic as the reference system (WGS 84). For Argentina's Gauss-Krüger (TM) coordinates, the origin is the intersection of the South Pole with the
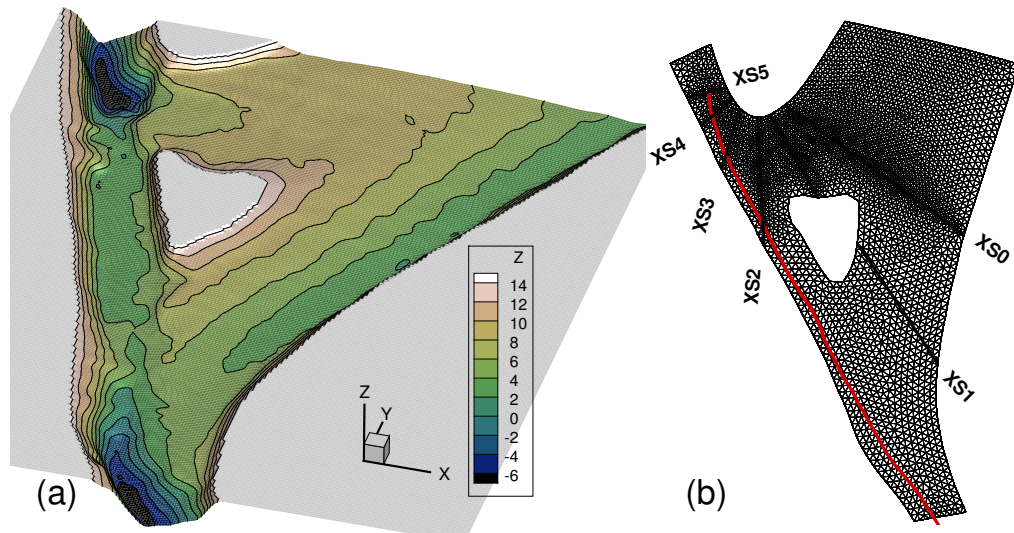
FIGURE 4.3: (a) DEM of the study site (ground elevation in metres), (b) Finite element mesh and surveyed cross-sections (XS) - red line: boat path followed during the water surface elevation survey.

central meridian of each band, and with a northing of zero. This procedure was packed in a module, part of a bundled software written in Fortran 95 to merge field data with point and polyline data from complementary sources (river banks elevations, borderlines around inner islands, etc.). The bundled comprises the SMS (2000), the visualization tool Tecplot (2011), and a set of in-house routines described in Vionnet (2010).

This topographic data manager tool allows to alter the outcome of the interpolation from the scatter data using different criteria, which may guide the user with the continuous assessment of the DEM generation process. An adaptive tessellation of the domain is then constructed with a Delaunay triangulation from the scatter point set. This triangular irregular network, linking each scatter point, allows the interpolation of elevation data using linear base functions onto a regular grid, whose steps-size are defined by the user. The algorithm defines automatically which node of the regular grid is inside or outside the computational domain, information used later to pass a 2D Laplacian kernel to smooth out the resulting bed elevation interpolation. This is because the DEM should represent the bare surface of the river bed with a smooth transition between the bed and riverbanks whenever possible, in order to avoid convergence difficulties nearby the boundaries of the computational domain due to contradictory data between bed elevation and local water depth.

A first DEM was generated with bathymetry data collected only with the echo sounder, whereas the final DEM was produced with data captured with the echosounder between 4 and 5 May 2010 (Table 4.2), and depth data estimated through the four-beam readings of the ADCP TRDI, corrected by roll and pictch with the aid of the VMT (Parsons et al., 2013). Figure 4.3(a) depicts the DEM so obtained.

4.2.3.2 ADCP data

Occasionally, reported results seem to be vague and open to different interpretations depending on the method used to extract secondary currents from the field data (Rhoads and Kenworthy, 1999; Lane et al., 1999). Despite this still ongoing controversy within the scientific community, the vast majority of researchers refer to the so-called Rozovskii method (see Rozovskii, 1957, p.138) to infer secondary motion. The Rozovskii procedure isolates the excess (or deficit) of the transverse velocity component relative to the respective depth-averaged value on any vertical profile. The method accounts for a rotation of the planar velocity vector with respect to the direction of the depth averaged velocity vector. However, the procedure depends upon having zero net secondary discharge at the vertical, a condition normally used to close the mathematical problem posed by the set of governing equations (Engelund, 1974), albeit unrealistic in practical situations.

Dinehart and Burau (2005) proposed a two steps method to isolate secondary currents: first, a bend-crossing plane of velocity vectors from ADCP data is derived, and second, elements of the backscatter intensity planes are used to guide an interactive alignment of the averaged velocity grids previously obtained. They found the bend-crossing plane through a section-straightening procedure, where the velocity ensembles are spatially translated to a straight line defined by a mean crossing line fitted along multiple transects.

The procedure adopted here for post-processing the field data involves two steps: the use of proprietary software in the first place and then in-house routines to get the transverse velocity field. In other words, filtered 3D flow data was first exported into spreadsheet files written in ASCII format with the proprietary program *ViewADP* Sontek (2004) or *WinRiver* II TRDI (2007), and later loaded into a Fortran 95-based software package called *read_aDcp* for further processing and visualization. The procedure *after_read_aDcp* allows users to integrate primary and secondary velocities from one or more surveyed cross-sections with the DEM, in turn generated with the routines described in Vionnet (2010).

The 3D velocity field data is projected with a procedure similar to that proposed by Dinehart and Burau (2005). Secondary currents were computed with (or without) the zero net cross-stream discharge constraint. The code decomposes both the horizontal-two dimensional or depth-averaged (2DH) velocity field, and the full 3D vectors into tangential (along the cross-wise plane) and normal (along the stream-wise plane) components of the absolute velocity relative to the ground, with the addition of the up component for the 3D case. Finally, both the tangential and up components define the

vertical-two dimensional (2DV) representation of the flow field along the projected cross-stream plane, in turn located through an orthogonal least squares fit to all trajectories navigated by the vessel during the surveys.

4.2.4 Numerical solutions

4.2.4.1 Numerical engine

The suite of numerical codes used in this work belongs to the open source Telemac-Mascaret system (Hervouet, 2007; Telemac-Mascaret Modelling System, 2014), currently developed by the research and development department of Electricité de France (EDF) and the Telemac Consortium. The Telemac-3d module solves either the hydrostatic or non-hydrostatic continuity and the time-averaged Navier-Stokes equations with a finite element discretization fully parallelized with the message passing interface paradigm.

The hydrostatic approximation consists on neglecting the vertical acceleration, diffusion and source term in the momentum equations. The non-hydrostatic approximation is based on the pressure decomposition into hydrostatic and hydrodynamic parts, allowing an accurate computation of the vertical velocity, which is coupled with the whole system of equations. The solution steps of the hydrostatic 3D version are: *i*) computation of the velocity field by solving the advection terms; *ii*) determination of a new velocity components by taking into account the diffusion and source terms (intermediate velocity field); *iii*) computation of the water depth from vertical integration of the continuity and momentum equations by excluding the pressure terms; and *iv*) determination of the vertical velocity w from the continuity equation and computation of the pressure step by the Chorin method (Hervouet, 2007).

4.2.4.2 Finite element meshes

The reasons why the finite element method is so successful for studying environmental problems are well-known: local character of the approximation functions, ability to treat natural boundary conditions, and ease in handling complex geometrical domains. However, the generation of an adequate discretization mesh and the estimation of the solution error are in general difficult tasks, particularly over complex 3D domains.

The so-called *a-priori* error estimate decides how the computed results deviate from the exact solution supplying information on convergence rates, but is unable to deliver quantitative or qualitative error information. *A-posteriori* error estimates, based upon

the computed solution, provide more practical accuracy appraisals (Babuska and Rheinboldt, 1978). This estimation seeks to evaluate the error in some specific measure, where the idea is to refine the mesh such that the errors are "equally" distributed over the computational mesh. Nevertheless, this error measure is somehow too abstract and does not provide users with specific features of the solution.

Consequently, the users usually base their final decision on similar, earlier computations. A simple rule of thumb is to increase the number of elements to reduce its average size Δ until the results of successive computations show no perceptible difference.

All triangular finite element meshes used here were produced with SMS (2000) with the embedded DEM and later exported into the binary Telemac format (called selafin (Mourad, 2011)). The meshes were fitted along external and internal boundaries where flow quantities were available (Figure 4.3(b)). The 3D finite element mesh was later obtained by extruding each linear triangle along the vertical direction into linear prismatic columns that exactly fit the bottom and the free-surface. In doing so, each column can be partitioned into nonoverlapping layers, requiring that two adjacent layers comprise the same number of prisms.

4.3   Results

4.3.1   Field data

4.3.1.1   Independent computation of river discharge

Due to intrinsic operational limitations, the ADCP is unable to measure near the bed, banks, and free surface (Simpson, 2001). For example, the Sontek ADCP employed has a profiling range capability of $1.2 - 40.0$ m, and a cell-size ranging between $0.25 - 5.0$ m with a minimum blanking distance of 0.7 m. The distance from the water surface to the center of the first bin was about 1.3 m approximately $[= 0.7$ m (blanking distance) $+ 0.2$ m (probe submergence) $+ \Delta z/2$ (see Table 4.2)]. The blind distance at the top layer and the "contaminated" bottom layer by side-lobe interference rendered between 55 % and 15 % of unmeasured depth for water columns located in shallow and deep zones, respectively. However, as it is shown later, the bulk of moving water scanned by the ADCP was large enough to capture cells of secondary circulation.

The mentioned limitations are overcome by the manufacturer through the utilization of extrapolation methods, which covers from the one-sixth power-law estimation technique to fit the vertical velocity profile within the inner portions of the cross-section to the

ratio interpolation procedure to infer the near-shore flow rates (Sontek, 2004; TRDI, 2007).

Contrary to these techniques, used to infer the flow discharge in real-time situations (Simpson, 2001), an independent calculation based on different assumptions was developed to test the in-house code. This *a-posteriori* estimate is based upon a rather crude approximation of the flow profiles along the gauged area of the cross-section as well as on the ungauged portions (free surface, bed and banks). Nevertheless, if the 3D structure of the loaded velocity field is correctly handled by the in-house code, these new flow discharge estimates should not be far from the values reported by the proprietary software.

It suffices to note that whereas the river discharge measured on May 4-5, 2010 (Table 4.2), estimated with the software *WinRiver* II (TRDI, 2007) was 1085 m^3/s on average with a fractional standard deviation of about 5.8%, the computation with *read_aDcp* yielded a mean value of 1100 m^3/s with a standard deviation of 6.1 %. Sixteen values of discharges measured along cross-sections XS1, XS3, XS4, and XS5 were selected (see Figure 4.3(b) for reference locations). The values measured on cross-section XS2 were ruled out because this transect is affected by recirculating flow nearby the left riverbank. Both results, the estimated with the proprietary software and the approximated with the in-house code have similar frequency distributions, with a median of 1100 m^3/s (see Appendix B).

It is seen that the river discharge values obtained with the in-house code bears favourable technical comparison with the values produced by the proprietary ADCP software. The comparison can be favourable only if the 3D velocity field is correctly uploaded by the code. In brief, the in-house code handles the field data in a manner consistent with the proprietary software and, therefore, it can be deemed appropriated for further processing, e. g. the isolation of secondary currents.

4.3.1.2 Cells of secondary circulation along the right branch of the diffluence

The experience accumulated when studying helical motion (Rozovskii, 1957; Engelund, 1974; Bathurst et al., 1979; Johannesson and Parker, 1989a) can be well suited to understand the present flow behaviour as long as the diffluence branches behave as river bends.

Figure 4.4(a) plots the measured float paths along the diffluence showing a clear flow partition upstream of the two river branches, with a downstream zone where the water is either stagnant or circulating weakly (behind the fluvial island). This pattern is
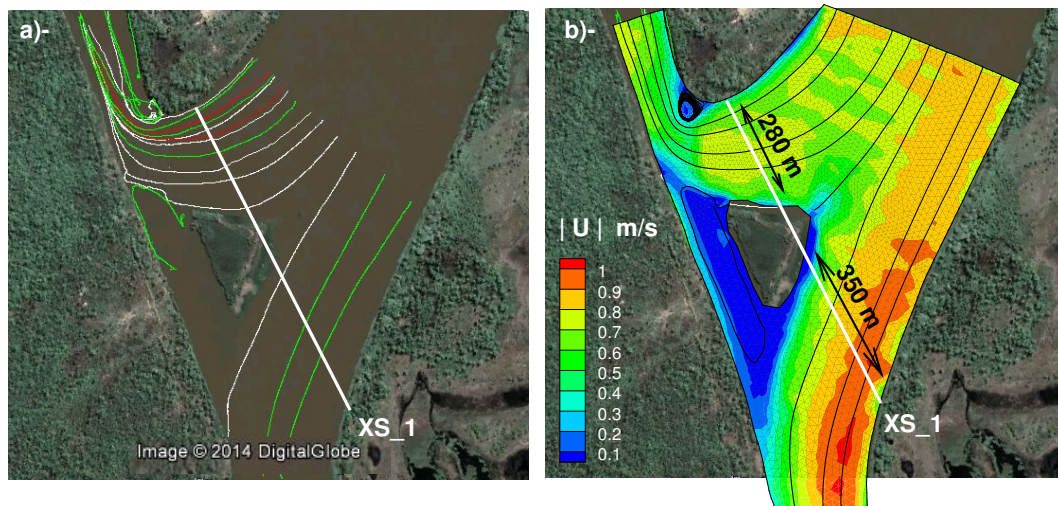
FIGURE 4.4: (a) Float paths, (b) Streamlines of the 2DH results of Telemac-2d. Sourse: Google Earth

reproduced in Figure 4.4(b), which depicts the numerical results of a 2DH calculation obtained with Telemac-2d. There is a clear correspondence between the observed float paths and the computed streamlines of the depth-averaged flow.

Some characteristic flow features along the right branch of the diffluence are observed in Figure 4.4; *i*) the size and shape of the stagnant water zone behind the fluvial island, which bounds the water motion along the right branch in such a way that it looks like an open-water pipe elbow flow, *ii*) the downstream extension of the detached flow behind the vortex of vertical axis formed near the curve apex; an unusual flow situation barely found on the alluvial system of the Paraná River (somehow showing the artificiality of the channel morphology, excavated at the beginning of the twentieth century), *iii*) the convergence of neighboring streamlines as the flow approaches the curve apex, not only in response to curvature effects but also enhanced by an effective cross-section reduction due to the vortex presence. It seems then that the curved flow along the right branch should be prone to the formation of secondary flow. This distinctive flow feature should be embedded in both the numerical results and the field data, where the former depends on the ADCP proprietary software, and to a lesser extent, on the used in-house code.

The proprietary *RiverSurveyor* software Sontek (2004) handles depth-averaged data across the measured transect without further processing. Thus, after conversion of geographical positions to TM (Gauss-Krüger) coordinates, the information can be readily exported onto georeferenced satellite images of the study site for further analysis. Few transects with the 2DH velocity field measured during the 2004 and 2006 field works (see Table 4.2) are depicted in Figure 4.5(a) and Figure 4.6(a). A clear flow separation just downstream of the inner bank apex is observed in both field data, which surely alters the size and shape of the secondary circulation cell.

In order to analyze the 3D structure of the flow field, it was necessary to resort to the in-house code. Upstream of XS2 it is possible to observe two well differentiated flow behaviour. Figure 4.5(b) shows that the streamwise acceleration and deceleration the flow must undergo at the outer and inner banks, respectively, along XS1 are so significant that a net unidirectional flow in the crosswise direction from outer to inner regions must set up for mass continuity reasons.

A word of caution is required here: Figures 4.5(b) and 4.6(b) correctly depict cross-section XS1 from left to right riverbanks where the cumulative distance s starts from zero at the first gauged water column. Data taken on 2006 shows a well defined flow partition above the sandbar (Figure 4.6(b)), in coincidence with the field and numerical data shown in Figure 4.4. A left branch width of about 350 m is consistent in both Figure 4.4(b) and Figure 4.6(b). Thus, Figure 4.5(b) depicts the right branch of XS1 only while Figure 4.6(b) depicts the whole XS1. The difference in the bathymetry shape is because the boat path surveyed on 2004 was closer to the scour hole present at the curve apex.

Finally, the single cell of secondary motion is clearly seen in both Figure 4.5(c) and Figure 4.6(c), captured along XS2 during the field works of 2004 and 2006, respectively. The secondary circulation is rather intense, with transverse velocities on the order of 0.40 m/s, which represents about 40-50% of the primary flow component.

4.3.2 Numerical simulations

4.3.2.1 Boundary conditions and mesh independency test

At the sidewalls, the velocities tangential and normal to the boundary were set equal to zero (no-slip condition). At the outlet boundaries, the normal gradients of the flow velocity were set equal to zero, whereas a free-surface elevation of 10.545 m and 10.526 m at the left and right downstream branches, respectively, were imposed. The inflow boundary was fixed at $Q = 1629$ m^3/s, and located far upstream to avoid affecting the solution in the region of interest. The field measurements yielded a closure error less than 1% in terms of river discharge ($Q_{right} = 595$ m^3/s and $Q_{left} = 1044$ m^3/s). These data were measured during the fieldwork of March 2, 2012.

The generation of adequate meshes with successive halved elements is impossible when unstructured mesh generators are used to discretize the geomorphology depicted in Figure 4.1. Therefore, and in order to circumvent the limitations mentioned in section 2.4.2,
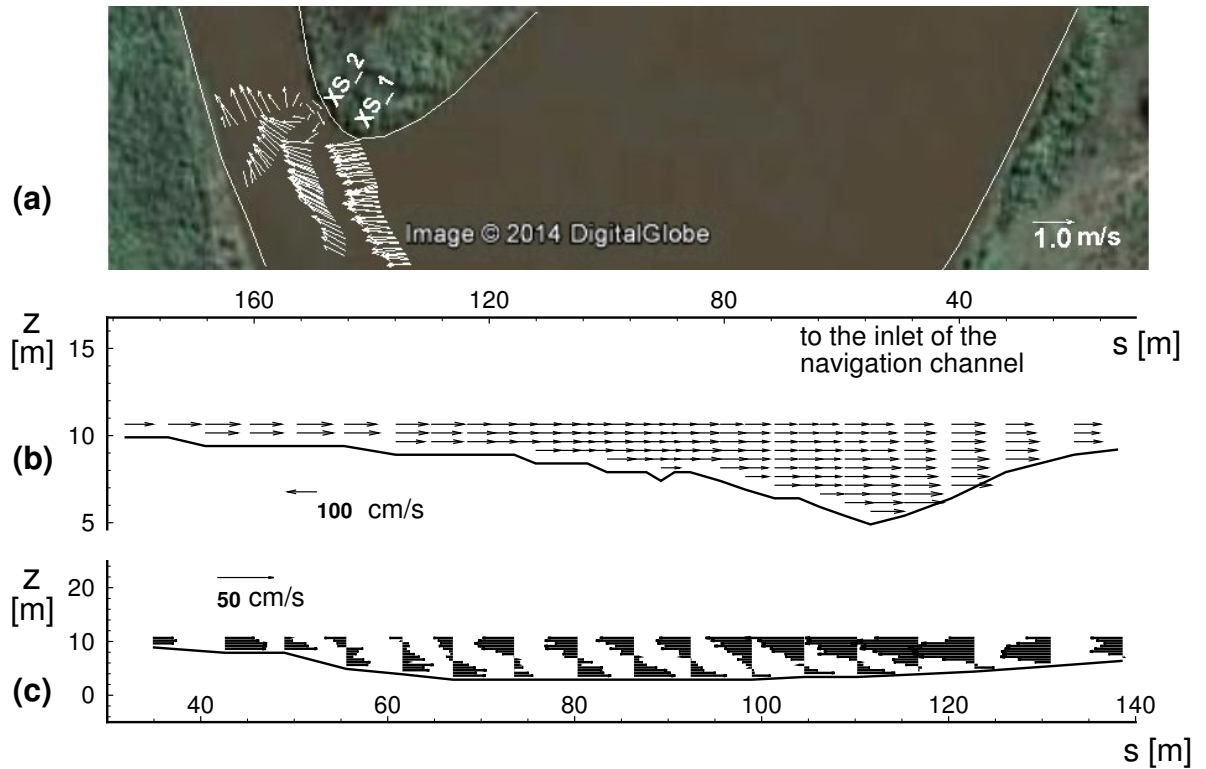
FIGURE 4.5: 2004 Sontek ADCP: (a) *ViewADV* 2DH velocity vectors, Source: Google Earth, (b) *read_aDcp* 2DV velocity field on right branch of XS1 (acces channel discharge: 905 m^3/s), (c) *read_aDcp* 2DV velocity field on XS2.

four meshes were generated with decreasing "mean" element size Δ according to

$$\Delta \simeq \sqrt{\frac{2\Omega}{N_e}} \,, \tag{4.1}$$

where Ω is the area of the computational domain and N_e the number of elements (N_n is the number of nodes (Table 4.3)). The first three meshes extended over the larger domain while the fourth mesh overlapped the shorter computational domain (see Figure 4.1 for details). The objective was twofold; to show that solutions computed on successive meshes display no perceptible difference albeit converging to a final state, and to infer the hydraulic gradient and the proper boundary conditions of the incoming flow into the smaller domain (Figures 4.1 and 4.3(b)).

All computations were performed over unstructured triangular meshes with 5 layers but the finer, where 15 layers were used instead. The adequacy of the results were judged on the basis of the computed flow discharge at the diffluence. Table 4.3 clearly shows that when the discretization is fine enough, the computed results can be considered mesh insensitive. The final flow partition of 585 m^3/s and 1044 m^3/s is well within the uncertainty range around the mean value of the measured river flow rate (see Table 4.3 and appendix B).
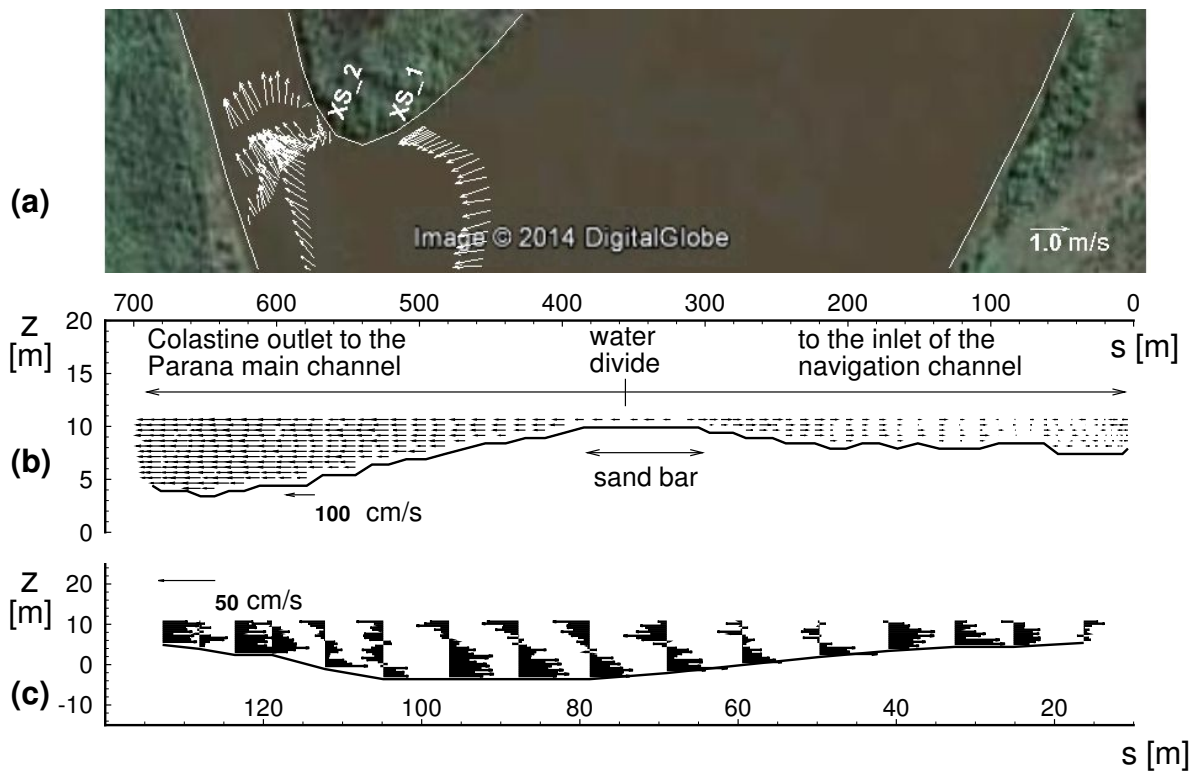
FIGURE 4.6: 2006 Sontek ADCP: (a) *ViewADV* 2DH velocity vectors, Source: Google Earth, (b) *read_aDcp* 2DV velocity field along the whole XS1 (access channel discharge: 967 m^3/s),(c) *read_aDcp* 2DV velocity field on XS2.

For a given initial condition consisting on a constant water surface elevation and velocity components equal to zero, the steady state was reached after about 100000 time steps of 0.1 s, corresponding to a physical time of about 2 hours 46'. When ran on eight processors of a Z600 HP workstation, the typical elapsed time to achieve convergence was on the order of 35'.

The numerical simulations were performed with a roughness-length representation based on the Nikuradse coefficient $k_s = 0.01$ m and with a constant turbulence model with eddy viscosity coefficient $\nu_t = 1.0 \times 10^{-5}$ m$^2/s$. Different values of the hydraulic resistance height k_s were used to adjust the observed water surface slope in the streamwise direction. The adopted value of $k_s = 0.01$ m yielded the best fit between the observed and computed hydraulic gradient (in both computational domains, large and short). The values for ν_t were selected after the recommendations of Vionnet et al. (2004).

4.3.2.2 The 3D flow structure

The right branch of the diffluence exhibits a strong asymmetry of the bed topography. The flow along this branch develops zones of acceleration, stagnation, deflection,

TABLE 4.3: Mesh independency test

Mesh	N_n	N_e	layers	prisms	Δ[m]	Q_l[m^3/s)]	Q_r[m^3/s)]
1	1006	1585	5	7925	74	994	635
2	2354	4083	5	20415	46	1056	573
3	23224	44534	5	222670	15	1041	588
4	3380	6623	15	99345	13	1044	585

Q_l and Q_r stand for Q_{left} and Q_{right}, respectively

separation, and reattachment (Figures 4.4(a), 4.5(a), and 4.6(a)).

Figure 4.7(a) depicts the 3D velocity field along the edges of the computational domain nearby the outflow boundary representing the inlet to the access channel. The numerical solution captures the area of stagnant water behind the island, the vertical axis vortex at the curve apex of the inner bank, and the detached flow downstream of it. The contour map embedded in Figure 4.7(a) reflects the module of the 3D velocity field, in m/s.

The size and location of the vortex shown in Figure 4.7(a) are in fairly well concordance with the drawn float paths and with the ADCP measurements (Figures 4.4(a), 4.5(a), and 4.6(a), respectively). The formation of the separation zone deviates the flow towards the left bank, at the inlet of the access channel. Nonetheless, the size of the detached flow area behind the vortex of a vertical axis seems to be better captured by the 2DH simulation (Figure 4.4(b)) rather than by the full 3D solution. Similar effects have been noted by Lloyd and Stansby (1997) when comparing 2D and 3D shallow-water numerical solutions of the wake formation behind models of conical islands with laboratory measurements.

The longitudinal profile of the free-surface shown on Figure 4.7(b), whose trace is detailed in Figure 4.3(b), reflects part of the flow behavior along the diffluence. The free-surface is flat behind the mid-channel island, in coincidence with the zone of stagnant water, and falls sharply on both extremes towards the inlet of the access channel and the main-channel of the Paraná River. There is a concentrated jump when the water surface, elevated by the centripetal effects on the outer edge of the left branch, meets the area of the flat surface behind the island. This area of flat free-surface behaves like a rigid body since it plays the role of the missing channel wall on the outer bank. There is a clear correspondence between observed data and numerical results.

Figure 4.8(a) shows the numerical results along the selected surveyed cross-sections (XS), numbered from 0 (XS0) at the upstream inlet boundary to 5 (XS5) towards the downstream boundary within the access channel (see Figure 4.3(b) for surveyed XS locations).
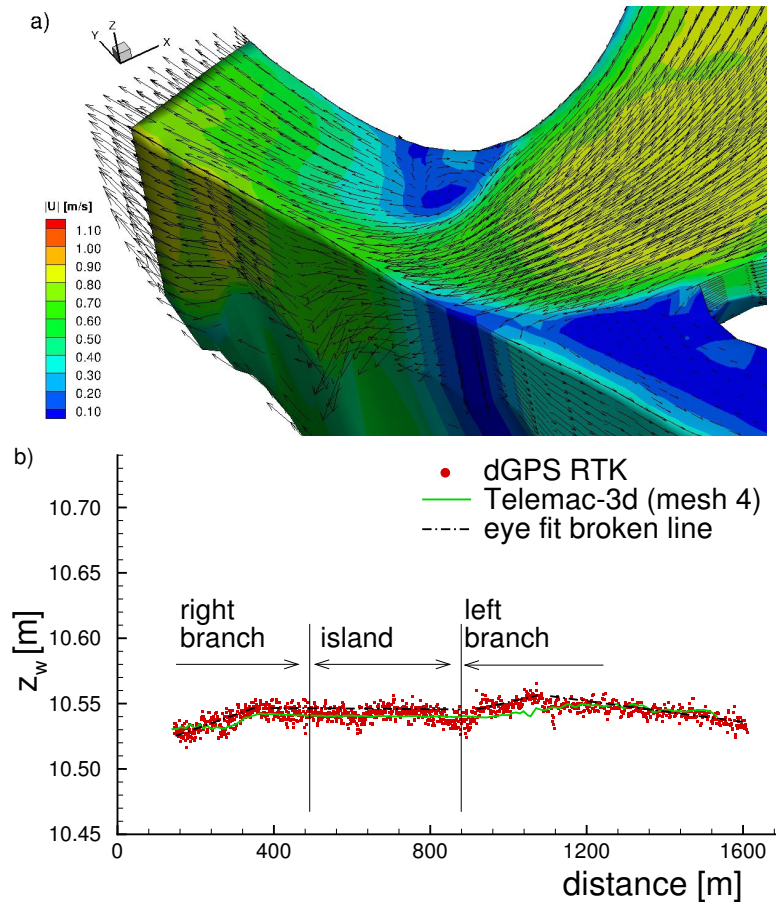
FIGURE 4.7: (a) View of the 3D velocity field (measured discharge at the access channel inlet: [588-602]m^3/s (see Table 4.2), simulated: 585 m^3/s (see Tabla 4.3)); (b) Free-surface along the boat path of Figure 4.3(b).

The XS2, a bit downstream of the diffluence, exhibits a flow pattern compatible with a cell of secondary circulation with transverse velocities on the order of 0.40 m/s, i.e. about 50% of the primary velocity component. Unfortunately, due to limitations of the postprocessing interface, it is not possible at this moment to extract the results from Telemac-3d following the same procedure used to treat the field data. However, and besides an optical effect due to the 3D projection algorithm used to plot the solution, the results along XS2 show a significant net unidirectional flow component in the transverse direction from outer to inner regions. It is the mass conservation constraint that triggers this transverse flow to compensate the accelerated flow that sets up along the inner regions of the bend. The contour values of the flow module points the region of accelerated flow.

Finally, Figure 4.9(a) is a plots of the distribution of the 2DH velocity field obtained from the 3D computations. The solution captures the overall flow pattern inferred from the float paths shown in Figure 4.4(a). Both numerical and field data show a weakly

curved flow field with almost parallel streamlines along the left branch.
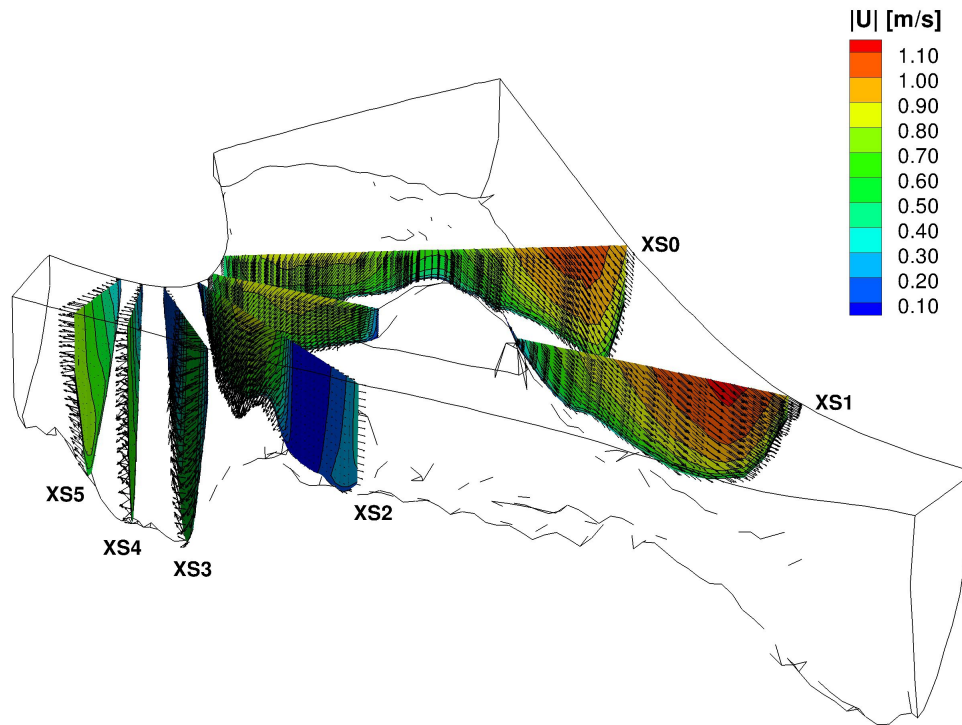
FIGURE 4.8: Computed flow patterns at surveyed XS.

4.3.3 A feasible solution to the sedimentation problem of Santa Fe's harbour

The cost of the maintenance dredging required to keep the access channel operational goes off the current ship toll system ruling the navigation of commercial vessels along the Paraná main channel from Santa Fe to the Atlantic Ocean. This additional cost, afforded by the Santa Fe Province, has put the local harbour in a disadvantageous position since the 1970s. Nevertheless, there is one possible solution that could deliver the basis for a new, cost effective alternative to turning around this disadvantage.

It is technical feasible to close the South Derivation Channel ("Canal de Derivacion Sur", pt. (d), Figure 4.1) in order to reverse the flow direction in the access channel. The partial closure of the South Derivation Channel -an ecological downstream discharge must be kept- can divert enough water to set up an unidirectional flow through the external reach of the access channel. The strength of this unidirectional flow should be able to keep most of the transported sand particles up in suspension. Local people

reported having witnessed the flow reversal phenomena along the access channel during some of the extreme floods experienced by the Paraná River on the twentieth century (Vionnet et al., 2006), albeit there is no record of such inversion.

Figure 4.9(b) sketches the 1D network of the so-called Leyes-Setúbal system, a complex anabranch system of the Paraná main channel. It has its origin nearby the Colastiné mouth and receives part of the Colastiné discharge through the access channel. Due to the lack of systematic discharge records along the Leyes-Setúbal system, it is quite reasonable to assume a mean flow through it on the order of 2400 $m^3 s^{-1}$. Such estimate is the outcome of assuming an average flow velocity between 0.8 and 1 ms^{-1} with an approximated wetted area of 2400-3000 m^2 along the Hanging Bridge cross-section (300 m wide and 8-10 m depth, see Figure 4.9(b) for the bridge XS location). Notwithstanding further hydrological and morphological studies are necessary if the proposed solution is eventually considered, there seems to be enough water available to divert part of it through the access channel.

The constructed numerical model with Telemac-3d is the natural starting point to test the proposed solution. The contour values of the bed shear velocity U_*, computed for the base state (the scenario reported from Figures 4.7 to 4.9(a)), along with 4 testing points located within the study area are detailed in Figure 4.9(a). Point A is located at the access channel mouth, where the strength of the secondary currents is maximum, point B upstream in the Colastiné River, point C in the middle of the external reach of the access channel, and point D downstream, on the thalweg of the bifurcation left branch.

Figure 4.9(a) includes not only the contour values of U_* in the background but also the 2DH velocity vectors distribution on top of it. Table 4.4 summarizes the computed values of U_* in the testing points when the boundary condition at the outflow of the right downstream branch is changed from free to a prescribed flow condition. The negative values of Q stands for the new inflow boundary conditions whereas the positive value of 585 $m^3 s^{-1}$ corresponds to the base scenario. Figure 4.10(a) shows the counterpart of Figure 4.9(a) when the outflow boundary condition at the inlet of the access channel is set to the prescribed inflow value $Q = -1100$ $m^3 s^{-1}$.

The large, low-gradient sandy-bed Paraná River moves its bed material as both bedload and suspended load, albeit suspended load far dominates bedload (Amsler et al., 2005). Strictly speaking, the separation between both transport modes is not a sharp process. Nonetheless, two criteria are widely used to estimate the onset of initiation of motion and initiation of suspension. The criteria used to quantify the onset of motion of grains of a non-cohesive sediment bed, and the onset of significant suspension of bed material

TABLE 4.4: $U_*[\mathrm{ms}^{-1}]$ for the different flow scenarios in the access channel

Q[m³s⁻¹]	585	−500	−700	−900	−1100
A	0.019	0.018	0.027	0.035	0.043
B	0.045	0.047	0.047	0.047	0.047
C	0.004	0.056	0.064	0.073	0.081
D	0.047	0.078	0.082	0.087	0.089
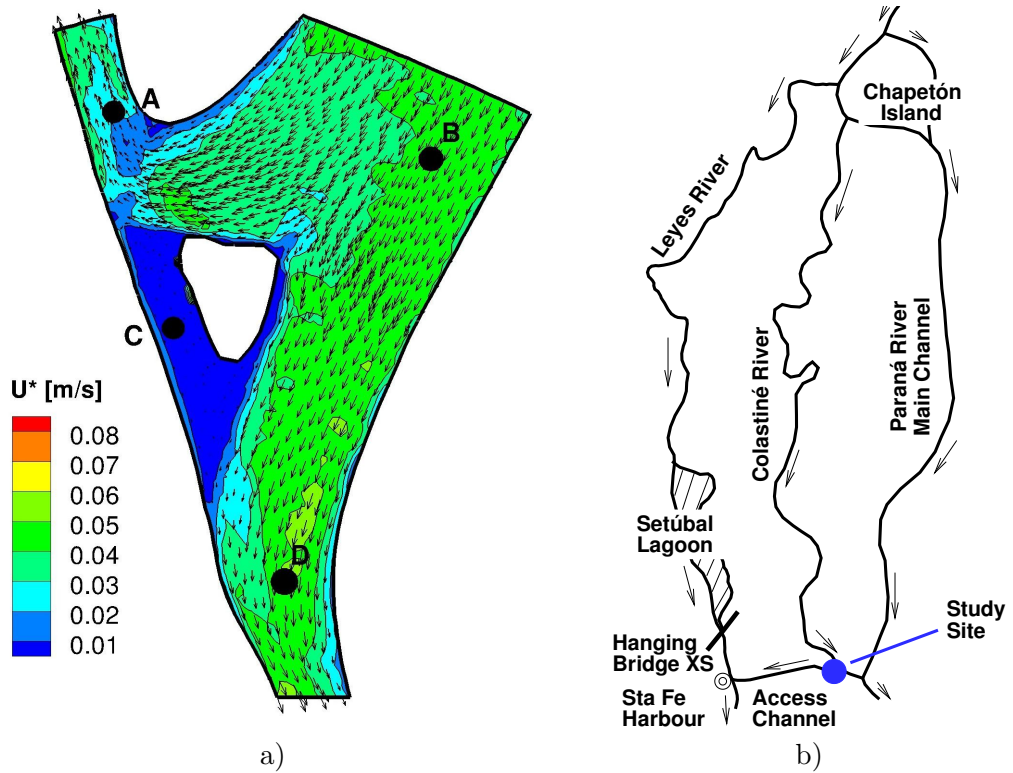
FIGURE 4.9: (a) Distribution of U_* and 2DH velocity field for the base state; b) Sketch of the Leyes-Setúbal system upstream of Santa Fe City.

are the Shields diagram and the Bagnold approximation, respectively. The Shields curve reads

$$\frac{U_*^2}{gRD} = 0.22\mathbf{Re}_{\mathrm{p}}^{-0.6} + 0.06 \times 10^{-7.7\mathbf{Re}_{\mathrm{p}}^{-0.6}} \ , \tag{4.2}$$

after Brownlie (1981), for any river bed composed of grains of characteristic size D and submerged specific gravity R, where $\mathbf{Re}_{\mathrm{p}}$ is a particle Reynolds number defined by the expression

$$\mathbf{Re}_{\mathrm{p}} = \frac{\sqrt{gRD}D}{\nu} \tag{4.3}$$

Here g is the acceleration due to gravity and ν the kinematic viscosity of water that is

approximately 1.0×10^{-6} m^{2}s^{-1} at $20°$ C. The so-called Bagnold criteria, a standard rule of thumb commonly accepted to define the onset of significant suspension, is defined by

$$\frac{U_*}{W_s} \simeq 1 \ , \tag{4.4}$$

where W_s is the particle fall velocity, usually computed as an empirical function of the grain diameter, the acceleration due to gravity, and the kinematic viscosity of water.

Now, the prevailing sediment transport modes along the four testing points can be inferred from a diagram of U_*^2/gRD vs. $\mathbf{Re}_{\mathrm{p}}$. Figure 4.10(b) depicts the threshold curves defined by equations (4.2) and (4.4) with few isolated points summarizing the flow conditions of Table 4.4, for a particle size range that goes plus-minus one standard deviation from the geometric mean size $D_g = 221\mu$ m (Figure 4.2(c)). This range covers almost 70 % of all sediment sizes sampled at the study site, under the assumption that the grain distribution can be well approximated with a Gaussian function.

The points encircled in Figure 4.10(b) represent the dominant sediment transport modes for the base flow situation along the testing locations. The prevailing conditions at point C are of no sediment motion for both ends of the sediment size range considered. Any particle within that size range that reaches the neighbourhood of C either as bedload or suspended load is going to remain nearby without moving any further. On the other testing sites, the prevailing transport mode is suspended for the lower range of sediment size and mixed for the upper range.

However, the situation changes drastically when the flow along the access channel is reversed, notably in point C. All sediment particles within the tested range is going to be transported mostly in suspension except in the vicinity of point A, where bedload would still be dominant. The situation improves around point D and there are no signs of changes upstream of the diffluence, in the vicinity of point B. The prevailing bedload transport condition around point A would deactivate if the actual right branch is closed up to the mid-channel island. The low values of U_* (Figure 4.10(a)) between the actual right riverbank and the mid-channel island clearly shows that the future left branch -under the flow reversal scenario- would be part of an unstable diffluence (or part of an evolving confluence). It seems only a matter of time before the river ends up closing the branch. Consequently, the eventual closure of both the South Derivation Channel and the actual right branch of the diffluence surely warrant the setup of a self-dredging flow turning the actual diffluence into a stable confluence node.
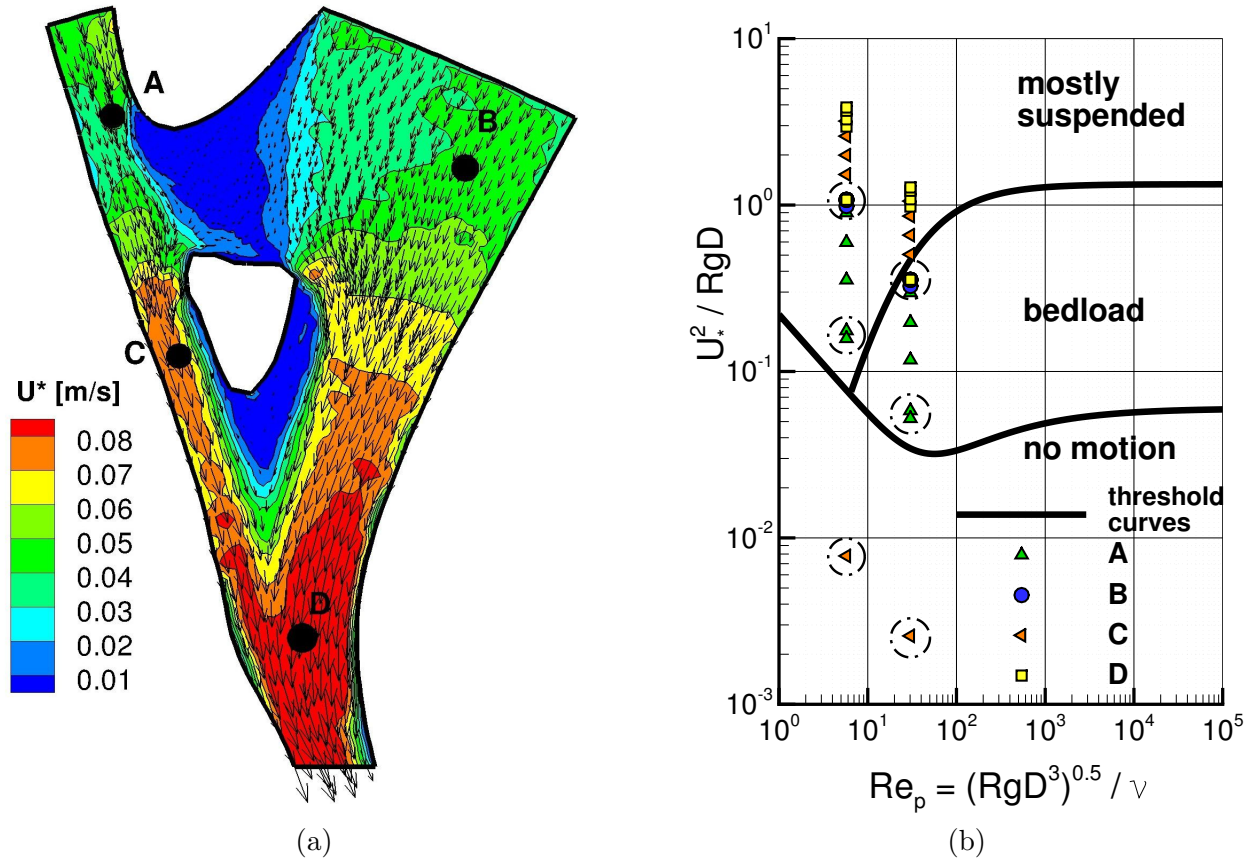
FIGURE 4.10: a) Distribution of U_* and 2DH velocity field for $Q = -1100\text{m}^3\text{s}^{-1}$; b) Shield's diagram; the encircled points represent the dominant sediment transport modes for the base flow situation summarized in Table 4.4 (first column) for the size range [127-384] um of bed particles.

4.4 Conclusions

Float paths produced on the study site, and numerical results obtained with Telemac, confirm the presence of a central core of convectively accelerated flow bounded by curved streamlines along both branches of the diffluence. The flow along the left branch is smooth, weakly curved, whereas the flow along the right branch exhibit regions of flow stagnation, separation and reattachment.

Field data captured with the Sontek ADCP, and processed with an in-house code show that the right branch contains a well defined central cell of secondary currents. Although absent here, TRDI ADCP data show the same secondary motion. The helicoidal flow formed along the right branch keeps a scour hole at the access channel mouth. There, the channel sharp turn provokes the separation of the incoming boundary layer and,

therefore, the formation of a vertical axis vortex at the curve apex. All these features are well captured by the 2D and 3D numerical solutions, including the observed free-surface deflection along the diffluence head whose "piecewise" shape is in tune with the expected flow behaviour.

River discharge data processed with the in-house software is consistent with the proprietary ADCP software, a required validation step before inferring the presence of secondary currents.Unfortunately, a unified algorithm to isolate cross-flow from a skewed discharge produced with either numerical or field data are still lacking. In particular, no unbiased algorithm is yet available to project the 3D computed velocity field onto selected cross-sections. The mentioned limitation hampers the users to judge the capability of Telemac-3d to capture secondary currents along river bends. The group is developing the user interface to extract the numerical data from Telemac-3d to project them onto any cross-section with the same algorithm embedded in the software developed to treat field data.

According to the produced field measurements, the hydrodynamics of the studied bifurcation has remained essentially unaltered during the observation period. Initially, it was possible to spot zones of stagnant water around the sand-bar driving the flow along circular streamlines, a role later occupied by the emerged mid-channel island. However, and despite the recent changes seen during the study period, the reconstructed morphology of the site along a century-long record establishes the stability of the riverbanks surrounding the bifurcation node at the access channel mouth. The node initially conformed to a Y-shaped bifurcation, later evolved to a T-shaped, and recently underwent a transitional stage towards a Y-shaped node with a bifurcation angle γ close to the stability range reported by Federici and Paola (2003). How much of this convergence is due to recent changes of the Colastiné River hydrology, or to a natural process, is beyond the scope of this paper.

Finally, the numerical outputs for the flow reversal scenario along the access channel show that the chronic sedimentation problem experienced by the Santa Fe City harbour is solvable. The closure of both the South Derivation Channel and the actual right branch of the diffluence surely warrant the setup of a self-dredging flow (such that most transported sediment carry in suspension) turning the actual diffluence into a stable confluence node.

While the local authorities decided to move the harbour to the point marked (e) in Figure 4.1, FICH (1998) recommended doing so nearby point (f). The reasons why the local harbour authorities ignored to explore the South Derivation Channel closure in occasion of the FICH (1998) studies are not clear to the authors. Around 2008, part

of the harbour facilities had been turned into a commercial complex gathering a hotel-casino with a shopping mall. Nevertheless, the commercial complex is far away from the loading/unloading areas. The closure of the South Derivation Channel could provide not only the required self-dredging flow along the access channel but also several hundreds of meters for ship docking and additional space for good's storage.

Chapter 5

Conclusions

5.1 Conclusions

In the last decades, theoretical as well as experimental research have emerged on circular open-channel flows with the hope of uncovering part of the mechanisms responsible for river meandering. Whilst identification of secondary flows may be straightforward in open-channels with regular geometry and slowly varying plane curvature, it is not so in the case of natural meandering streams, whose boundaries are loose and irregular. Indeed, due to the continuously changing planform and variable bed topography, the hydrodynamics of a natural meandering stream is rather complex. The flow field is strongly three-dimensional (3D), and in each cross-section of the meandering stream a cross-flow develops. Thus, on the basic flow there is a superimposed flow in the transverse direction which occupies the large part of the cross section, whose formation is often understood in terms of the mechanical imbalance between the local elevation of the free surface and the centrifugal force induced by channel curvature.

As it was enunciated on the objectives set forth for this thesis, a great effort has been devoted to the collection of highly accurate field data that supposedly contains helical flow behavior. It was therefore of paramount importance to verify the capability of the most popular used method among practitioners and researches to filter the sought flow behavior from raw data.

This thesis analysed the treatment of field-based observations captured with two ADCPs in order to isolate secondary circulation from primary skewed flows; the comparison of methods able to filter helical motion with two theoretical descriptions of the process, the confirmation of the theoretical predictions with field data, and finally a comparison between results generated by Telemac-3d a hydrodynamics numerical model and field data.

In brief, all these topics were embraced in three different albeit related chapters:

i. Chapter 2: on the Rozovskii method to isolate secondary circulation from a skewed flow,

ii. Chapter 3: a global-referenced grid method to isolate secondary circulation from a skewed flow, and

iii. Chapter 4: flow pattern at a river diffluence at the alluvial system of the Paraná River.

The referred method, quite popular among practitioners and researches, is a simple procedure named after Rozovskii (1957), where the cross-stream component is computed with respect to the mean flow direction at each vertical, forcing by definition a zero net discharge in outward and inward directions. As a consequence, the secondary flow strength is determined locally at each individual vertical velocity profile instead of defining it on the entire cross-section.

It was though that whenever the Rozovskii method takes the correct orientation of the cross-stream plane, it computes the excess (or deficit) of the cross-component of flow velocity relative to its respective depth-averaged value. However, the method indeed computes a sequence of discrete planes oriented perpendicular to the local direction of the depth-averaged velocity field. Moreover, since the secondary flow structure is not necessarily perpendicular to the mean vector direction at each faceted plane, the ambiguities surrounding the cross-plane orientation have long puzzled researchers and practitioners

Rhoads and Kenworthy (1998a) assumed that part of the method shortcomings could be circumvented by projecting their field data onto fixed cross-sections. However, their contribution ignited a controversy that continues to the present days. For that reason, the questioning of the Rozovskii method was of substantial interest.

It was therefore the purpose of this thesis to contribute to the elucidation of the controversy with the implementation of two simple close flow solutions that exhibit cross-flow behavior. It was then established that despite the Rozovskii procedure is able to decompose the flow field in a helicoidal component and an zero depth-averaged error term, the cross-flow has distortion along the vertical entirely proportional to the streamwise velocity component.

Thus, eventhough the Rozosvskii method delivers vertical cross-flow-looking distributions, the profile indeed blends the sought crosswise velocity component with the unwanted streamwise velocity component. Nevertheless, and on the good side, the method

is able to indentify the presence of secondary currents, if any, at extremmly low cost (in terms of the computing power required).

An alternative method to treat the field data and to "project" the cross-flow was developed accordingly. The procedure adopted for post-processing the field data involved two steps: the use of proprietary software in the first place and then in-house routines to get the transverse velocity field. In other words, filtered 3D flow data was first exported into spreadsheet files written in ASCII format with proprietary programs, and later loaded into a fortran 95-based software package called *read_aDcp* for further processing and visualization.

The procedure *after_read_aDcp* allows users to integrate primary and secondary velocities from one or more surveyed cross-sections with the DEM, in turn generated with the routines described in Vionnet (2010). The 3D velocity field data is projected with a procedure similar to that proposed by Dinehart and Burau (2005). Secondary currents are computed with (or without) the zero net cross-stream discharge constraint. The code decomposes both the horizontal-two dimensional or depth-averaged (2DH) velocity field, and the full 3D vectors into tangential (along the cross-wise plane) and normal (along the stream-wise plane) components of the absolute velocity relative to the ground, with the addition of the up component for the 3D case.

Both the tangential and up components define the vertical-two dimensional (2DV) representation of the flow field along the projected cross-stream plane, in turn located through an orthogonal least squares fit to all transects navigated by the vessel during the surveys.

The treatment of field data performed in Chapther 3 with the proposed procedure was highly consistent with the theoretical conclusions of Chapter 2, i.e., Rozovskii adds to the helical component an error term proportional to the streamwise velocity. On the contrary, the algorithm based on *ENU* coordinates isolates extremely well the secondary circulation. It is worth to mention that the implemented procedure relies on two separated though equivalent algorithms, one "dissipative" since data is lost as it goes on and the other "conservative" where all and energy single depth-cell data is kept in memory. Moreover, the data processing is highly consistent with the discharges values delivered by the proprietary software. All these assurances guaranted the quality and consistency of the presented results, which allowed the estimation of the cross-sectionally distribution of the Rozosvskii relative error.

Finally, Chapter 4 revisits the study area where field data have been consistently collected all along these thesis years. There, the thesis presented field and numerical data depicting the flow pattern formed at a diffluence of the Colastiné River, where one

branch accesses the local harbour. The harbour has been in decline since the 1970s due to costly maintenance dredging of the access channel. The objective of the Chapter was therefore twofold: to show the persistence of the flow pattern developed at the diffluence despite recent morphological changes seen at the site, and to test a possible solution to the access channel sedimentation problem.

Knowledge gained during the execution of the study helped to validate a code developed to process field data captured with two acoustic Doppler current profilers (ADCPs). The results confirm that both branches are prone to developing secondary currents. Simulations show that an engineering intervention downstream of the bifurcation can establish a self-dredging flow reversal along the access channel, turning the actual diffluence into a stable confluence. Last but not least, the experimental data presented in Chapter 4 was collected with a Sontek ADCP, showing the consistency of the projected cross-flows with those captured with the TRDI ADCP. Since the postprocessing procedures were essentially the same for both data sets, it may be concluded that the presented results are, among other issues, device independent.

Four key aspects are novel in this work: *i*) the extension of the classical Engelund solution, *ii*) the established theoretical result showing that Rozosvskii is indeed an ill-conditioned method, *iii*) the development of an alternative projection method to treat ADCP data (consistent with the theoretical framework discussed before), and *iv*) the engineering solution showing that by no means is necessary to relocate the Santa Fe harbour at the incredible cost of 180 millions of USD.

Appendix A

Supplemental material

A.1   Conceptual model

The single cell of cross-stream circulation is well understood. However, it is appropriated to highlight first the salient aspects of known works on curved open channel flows (Rozovskii, 1957; Engelund, 1974). Subtle aspects can be found in more elaborated works (Johannesson and Parker, 1989a; Blanckaert and de Vriend, 2003).

The long wave approximation reduces the fluid motion in vertical direction z to a mechanical balance between gravity and pressure, yielding the hydrostatic pressure distribution $g + \rho^{-1} \partial p / \partial z \simeq 0$, where g is the acceleration of gravity, ρ the fluid density, and p the fluid pressure. Then, the cross-stream circulation cell can be explained in terms of a local imbalance between the centrifugal force and the pressure gradient in transverse direction. With reference to Figure A.1, if (r, θ, z) are the cylindrical coordinates in radial, azimuthal, and upward directions, respectively, the radial velocity component, u_r, occurs in planes perpendicular to the primary-flow component, u_θ, and is originated by the centrifugal acceleration u_θ^2 / r due to channel curvature.

Then, and according to Engelund (1974), the reduced set of equations governing the flow on curved open channel is

$$\frac{\partial (r u_r)}{\partial r} + \frac{\partial u_\theta}{\partial \theta} = 0 \tag{A.1}$$

$$-g \frac{\partial z_w}{\partial r} + \frac{u_\theta^2}{r} + \epsilon \frac{\partial^2 u_r}{\partial z^2} = 0 \tag{A.2}$$

$$gS + \epsilon \frac{\partial^2 u_\theta}{\partial z^2} = 0 , \tag{A.3}$$

where z_w is the elevation of the free surface above datum, ϵ is the eddy viscosity coefficient -assumed constant- and S is the longitudinal channel bed slope which satisfies the
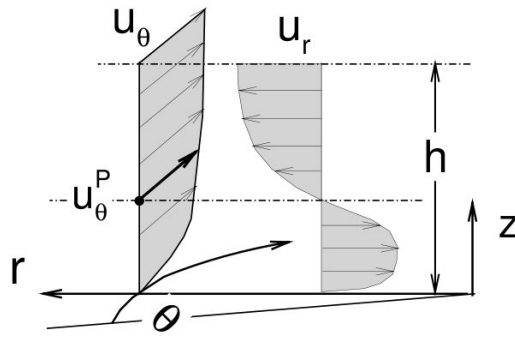
FIGURE A.1: Sketch of curved open-channel flow.
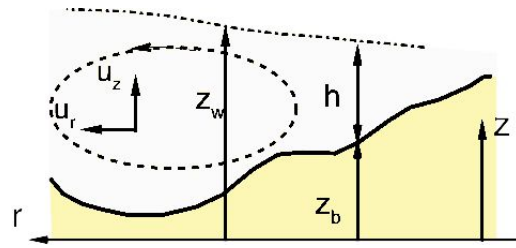
FIGURE A.2: The super-elevation phenomena.

geometric constraint $Sr = S_0R$, where $S = -dz_b/rd\theta$ such that S_0 represents the slope along the channel centre at $r = R$. Here, z_b is the bed elevation above datum.

Direct integration of Eq.(A.3) yields a parabolic distribution for u_θ, resolved by Engelund (1974) after assuming a free-slip velocity at the bed level. Then, since the stream-wise velocity component, u_θ, varies from zero or nearly so at the bed to a maximum value at or near the surface, centrifugal effects are greater near the surface and less intense toward the bed. It is seen from Eq.(A.2) that the centrifugal force is mostly counterbalanced by the radial pressure gradient, which has been assumed to be dominated by a hydrostatic balance. Therefore, the radial pressure force is manifested as a local hydraulic gradient in radial direction, $\partial z_w/\partial r$, giving rise to the well-known transverse elevation phenomenon of the free surface (Figure A.2).

It is clear that the balance of both forces can hold only for a certain single element, situated somewhere close to the central portion of the water column and moving with a velocity equal to, say, u_θ^P (Rozovskii, 1957; Falcon, 1984). For particles moving near the upper portion of the water column with velocity $u_\theta > u_\theta^P$, the centrifugal force will be greater than the hydrostatic pressure gradient. These particles will be conveyed in radial direction, away from the centre of curvature. On the contrary, particles situated in the lower portion of the water column, for which $u_\theta < u_\theta^P$, will be moving toward the centre of curvature (Figure C-4). From continuity considerations, a non trivial vertical velocity

component u_z will develop simultaneously with the radial component, and the velocity field will acquire a complex 3D helical flow pattern round the river bend (Engelund, 1974; Bathurst et al., 1979).

The aforementioned description is due to (Rozovskii, 1957), and later reviewed by (Engelund, 1974) and (Johannesson and Parker, 1989a). A difficulty arises whenever the cross-stream is to be captured in the field, where the turbulent flow is far from being uniform and the bed geometry is irregular.

A.2   About curved flows

The flow of water in open-channel bends has attracted the consideration of scientists and engineers for many years. It turns out that the appearance of a transverse slope and of transverse circulation gives rise to considerable changes in the velocity structure of a stream at a river or channel bend. Owing to the redistribution of velocities over its width, there appear in the stream zones with increased velocity, where erosion of the bottom takes place, and zones with decreased velocities, where the deposition of sediment occurs. Transverse circulation gives rise to transverse displacement of sediment, and as such, its knowledge is relevant for the proper design of water intakes, dredging and bank protection works.

For a broad stream (whose width is much larger than its average depth), the walls (banks) of the channel only direct the stream and cause bending of the streamwise flow. Influence of the stream's friction against the banks is only manifested in a comparatively narrow strip near both sides of the channel, whereas it is practically unnoticed in the rest of the cross section. It is therefore relevant to estimate the order of magnitude of the various terms -or mechanisms- entering into the governing equations in order to find a simpler, albeit solvable system that retain the salient features of curved flows.

A word of caution is required here; a brief compilation of the main results posted by Rozovskii (1957) and Engelund (1974) are given in this report, and textual citations from their work were occasionally extracted but not explicitly marked. Care should be exerted in case part or all the following material is submitted for publication elsewhere.

A.2.1 Governing equations

The equations of motion for an incompressible fluid, averaged in the sense of Reynolds and written in cylindrical coordinates (r, θ, z), are:

$$\frac{\partial u_r}{\partial t} + \mathbf{u} \cdot \nabla u_r - \frac{u_\theta^2}{r} = -\frac{1}{\rho}\frac{\partial p}{\partial r} + \nu_t \left(\nabla^2 u_r - \frac{u_r}{r^2} - \frac{2}{r^2}\frac{\partial u_\theta}{\partial \theta} \right) \tag{A.4}$$

$$\frac{\partial u_\theta}{\partial t} + \mathbf{u} \cdot \nabla u_\theta + \frac{u_r u_\theta}{r} = -\frac{1}{\rho r}\frac{\partial p}{\partial \theta} + \nu_t \left(\nabla^2 u_\theta + \frac{2}{r^2}\frac{\partial u_r}{\partial \theta} - \frac{u_\theta}{r^2} \right) \tag{A.5}$$

$$\frac{\partial u_z}{\partial t} + \mathbf{u} \cdot \nabla u_z = -\frac{1}{\rho}\frac{\partial p}{\partial z} - g + \nu_t \nabla^2 u_z \tag{A.6}$$

$$\nabla \cdot \mathbf{u} = \frac{1}{r}\frac{\partial (r u_r)}{\partial r} + \frac{1}{r}\frac{\partial u_\theta}{\partial \theta} + \frac{\partial u_z}{\partial z} = 0 \;, \tag{A.7}$$

where $\mathbf{u} = (u_r, u_\theta, u_z)$ is the velocity vector with components in (r, θ, z) directions, respectively (Figure A.3), p is the pressure, ρ is the fluid density, g is the acceleration due to gravity, and ν_t is the eddy viscosity, assumed here constant. Above, the advective and the Laplace operators are given by

$$\mathbf{u} \cdot \nabla \equiv u_r \frac{\partial}{\partial r} + \frac{u_\theta}{r}\frac{\partial}{\partial \theta} + u_z \frac{\partial}{\partial z} \tag{A.8}$$

$$\nabla^2 \equiv \frac{1}{r}\frac{\partial}{\partial r}\left(r \frac{\partial}{\partial r} \right) + \frac{1}{r^2}\frac{\partial^2}{\partial \theta^2} + \frac{\partial^2}{\partial z^2} \;, \tag{A.9}$$

respectively. If it is possible to assume that in case of bend of enough length, the stream tends to some stable state in which the velocity distribution in all sections is the same and independent of the coordinate θ, and if it is further assumed that the vertical component of velocity is rather small in comparison with u_θ and u_r, which is a valid assumption in case of broad channels (i.e., away from the channel banks, $u_z \simeq 0$), the restriction of continuity reduces to

$$\frac{1}{r}\frac{\partial (r u_r)}{\partial r} \simeq 0 \rightarrow u_r = \frac{const}{r} \tag{A.10}$$
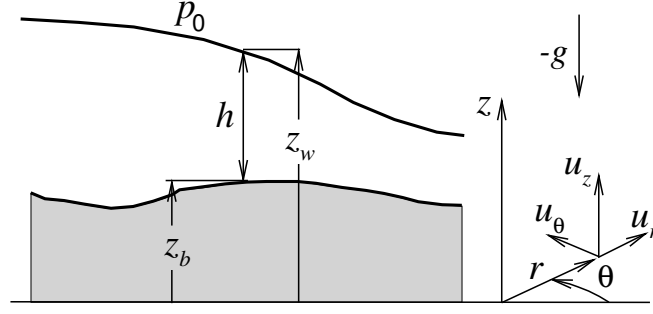
FIGURE A.3: Reference system for flow in open channel bends.

$$u_r \frac{\partial u_r}{\partial r} - \frac{u_\theta^2}{r} = -\frac{1}{\rho}\frac{\partial p}{\partial r} + \nu_t \left[\frac{1}{r}\frac{\partial}{\partial r}\left(r\frac{\partial u_r}{\partial r} \right) + \frac{\partial^2 u_r}{\partial z^2} - \frac{u_r}{r^2} \right] \quad \text{(A.11)}$$

$$u_r \frac{\partial u_\theta}{\partial r} + \frac{u_r u_\theta}{r} = -\frac{1}{\rho r}\frac{\partial p}{\partial \theta} + \nu_t \left[\frac{1}{r}\frac{\partial}{\partial r}\left(r\frac{\partial u_\theta}{\partial r} \right) + \frac{\partial^2 u_\theta}{\partial z^2} - \frac{u_\theta}{r^2} \right] \quad \text{(A.12)}$$

$$0 \simeq -\frac{1}{\rho}\frac{\partial p}{\partial z} - g \quad \text{(A.13)}$$

The last equation leads to a hydrostatic pressure distribution for a constant pressure p_0 acting above the free surface, since upon integrating with respect to z, and with reference to Figure A.3, the following result is obtained

$$\int_p^{p_0} dp = -\rho g \int_z^{z_w} dz$$
$$p = p_0 + \rho g \left(z_w - z \right) \quad \text{(A.14)}$$

Consequently, the lateral and longitudinal pressure gradient can be estimated, under the assumption that $z_w = h(r) + z_b(\theta)$, where z_w and z_b are the free surface and bed elevations above datum and h is water depth, as

$$-\frac{1}{\rho}\frac{\partial p}{\partial r} = -g\frac{\partial z_w}{\partial r} = -gS_r \quad \text{(A.15)}$$

$$-\frac{1}{\rho r}\frac{\partial p}{\partial \theta} = -\frac{g}{r}\frac{\partial z_w}{\partial \theta} = gS_\theta \quad \text{(A.16)}$$

Above, S_r and S_θ are the lateral and longitudinal slope of the free surface, both defined positive and given by

$$S_r = \frac{\partial z_w}{\partial r} \quad , \quad S_\theta = -\frac{1}{r}\frac{\partial z_w}{\partial \theta} = -\frac{\partial z_w}{\partial l} \quad \text{(A.17)}$$

Now, and since the motion can be considered approximately two-dimensional, the drop in free surface level Δz_w along the flow for all concentric circles is one and the same, while the length of a particle path $\Delta l = r\Delta\theta$ increases with the radius r. Therefore, the longitudinal slope can be expressed by the formula

$$S_\theta = \frac{I_\theta}{r} \ , \quad I_\theta = -\frac{\Delta z_w}{\Delta\theta} \tag{A.18}$$

where I_θ is the drop of the free surface per unit angle of turning. For a two-dimensional flow, the value of I_θ is one and the same for all streamlines. Later on, some caution will be exerted with the sign of S_θ, and correspondingly of u_θ

A.2.2 Reduced set of governing equations

Under the assumption of gentle turning, it is possible to derive an expression for the uniform flow in longitudinal direction defined in terms of the so-called friction velocity

$$u_*^2 = ghS_\theta \tag{A.19}$$

The mean flow velocity is then known to be given by

$$\frac{u_m}{u_*} = \frac{1}{\sqrt{c_F}} = c_Z \ , \tag{A.20}$$

where c_F and c_Z are the friction and Chezy coefficients, respectively. Since

$$u_m = \frac{1}{h}\int_{z_b}^{z_w} u_\theta dz = c_Z u_* \ , \tag{A.21}$$

the following dependence should be expected for u_θ

$$\begin{aligned} u_\theta \quad &\sim \quad c_Z\sqrt{ghS_\theta} \\ &\sim \quad c_Z\sqrt{\frac{ghI_\theta}{r}} \ , \end{aligned} \tag{A.22}$$

known as the Kozhevnikov's formula, according to Rozovskii (1957), page 93.

In order to evaluate the size of each term of the governing equation, it is convenient to introduce the following dimensionless variables

$$y = \frac{r}{h_0} \ , \ \zeta = \frac{z - z_b}{h_0} \ , \ u = \frac{u_\theta}{U} \ , \ v = \frac{u_r}{U} \ , \tag{A.23}$$

for same given depth and fluid velocity reference values, h_0 and U, respectively. Then, upon their introduction into the system of simplified equations of motion, (A.11)-(A.12),

the following set is obtained

$$r - \text{direction} \quad : \quad v\frac{\partial v}{\partial y} - \frac{u^2}{y} = -\frac{1}{\text{Fr}^2} \, S_r + \frac{1}{\text{Re}} \left[\frac{1}{y}\frac{\partial}{\partial y}\left(y\frac{\partial v}{\partial y}\right) + \frac{\partial^2 v}{\partial \zeta^2} - \frac{v}{y^2} \right] \quad \text{(A.24)}$$

$$\theta - \text{direction} \quad : \quad v\frac{\partial u}{\partial y} + \frac{uv}{y^2} = \frac{1}{\text{Fr}^2} \, S_\theta + \frac{1}{\text{Re}} \left[\frac{1}{y}\frac{\partial}{\partial y}\left(y\frac{\partial u}{\partial y}\right) + \frac{\partial^2 u}{\partial \zeta^2} - \frac{u}{y^2} \right] \, , \text{(A.25)}$$

where the dimensionless coefficients Fr and Re are known as the Froude and the Reynolds numbers, respectively, the latter based upon the eddy viscosity coefficient instead of the kinematic -or molecular- viscosity

$$\text{Fr} = \frac{U}{\sqrt{gh_0}} \quad , \quad \text{Re} = \frac{Uh_0}{\nu_t} \tag{A.26}$$

If the scales were properly chosen, the relevance of each term should be reflected by the coefficient in front of it. For example, the Paraná River is characterized by Fr~ 0.1, and Re$\sim 150 - 200$, considering $U \sim 1 \ ms^{-1}$ and estimating the eddy viscosity with the aid of the expression

$$a = \frac{u_* h_0}{\nu_t} \quad , \quad a \simeq 13.04 \tag{A.27}$$
$$\nu_t = 0.077 u_* h_0 \simeq 0.1 u_* h_0$$

where proper values of h_0 and S_θ for that river are $h_0 \simeq 10 \ m$ and $S_\theta \simeq 5 \times 10^{-5}$. It follows that $u_* = \sqrt{gh_0 S_\theta} \simeq 0.07 \ ms^{-1}$. Consequently, each term will compete within the balance of forces according to the following weight

$$\text{inertia} \quad \sim \quad O(1)$$
$$\text{gravity} \quad \sim \quad O(10^2)$$
$$\text{diffusion} \quad \sim \quad O(10^{-2}) \, ,$$

where the big Oh notation indicate order of magnitude. It is clear then that the flow is driven by gravity, with an increasing competition between inertia and turbulent diffusion to a lesser extent, albeit with a weaker contribution from the latter. It is therefore relevant to decide which term within each mechanism is dominant, taking into account the dependence with r of $u_r \sim r^{-1}$ and $u_\theta \sim r^{-1/2}$, i.e.

$$v \sim y^{-1} \, , \ u \sim y^{-1/2} \tag{A.28}$$

Starting thus with the equation of motion in $r-$direction

$$
\begin{aligned}
v\frac{\partial v}{\partial y} \quad &\sim \quad y^{-1}\left(-y^{-2}\right) = -y^{-3}\\[4pt]
\frac{u^2}{y} \quad &\sim \quad y^{-1}\left(y^{-1/2}\right)^2 = y^{-2}\\[4pt]
\frac{1}{y}\frac{\partial}{\partial y}\left(y\frac{\partial v}{\partial y}\right) \quad &\sim \quad y^{-3}\\[4pt]
\frac{\partial^2 v}{\partial \zeta^2} \quad &\sim \quad y^{-1}\\[4pt]
\frac{v}{y^2} \quad &\sim \quad y^{-3}\,,
\end{aligned}
\tag{A.29}
$$

whereas for the equation of motion in $\theta-$direction

$$
\begin{aligned}
v\frac{\partial u}{\partial y} \quad &\sim \quad \left(y^{-1}\right)\left(-\frac{y^{-3/2}}{2}\right) = -\frac{y^{-5/2}}{2}\\[4pt]
\frac{vu}{y} \quad &\sim \quad y^{-1}\left(y^{-1}\right)\left(y^{-1/2}\right) = y^{-5/2}\\[4pt]
\frac{1}{y}\frac{\partial}{\partial y}\left(y\frac{\partial u}{\partial y}\right) \quad &\sim \quad \frac{y^{-5/2}}{4}\\[4pt]
\frac{\partial^2 u}{\partial \zeta^2} \quad &\sim \quad y^{-1/2}\\[4pt]
\frac{u}{y^2} \quad &\sim \quad y^{-5/2}
\end{aligned}
\tag{A.30}
$$

Large values of y are usually attained in broad channels, characterized by the ratio $h_0/B \ll 1$, where B is the channel width. Consequently, and neglecting terms that decrease faster than y^{-2}, the dominant balance of forces in (A.24)-(A.25) is reflected by the following reduced system

$$
0 \quad \simeq \quad \frac{1}{\mathrm{Fr}^2}\,S_\theta + \frac{1}{\mathrm{Re}}\frac{\partial^2 u}{\partial \zeta^2}
\tag{A.31}
$$

$$
-\frac{u^2}{y} \quad \simeq \quad -\frac{1}{\mathrm{Fr}^2}\,S_r + \frac{1}{\mathrm{Re}}\frac{\partial^2 v}{\partial \zeta^2}
\tag{A.32}
$$

A.2.3 Boussinesq solution

A.2.3.1 Reduced system

Going back to physical variables, the reduced system (A.31)-(A.32) is written as

$$0 = gS_\theta + \nu_t \frac{\partial^2 u_\theta}{\partial z^2} \tag{A.33}$$

$$-\frac{u_\theta^2}{r} = -gS_r + \nu_t \frac{\partial^2 u_r}{\partial z^2} \tag{A.34}$$

The transverse velocity component, under the assumption of two-dimensional (2D) flow ($\partial_\theta \to 0$), must satisfy the condition of zero transverse discharge. From continuity

$$
\begin{aligned}
u_z|_{z=z_w} - u_z|_{z=z_b} &= \int_{z_b}^{z_w} \frac{\partial u_z}{\partial z} dz = -\int_{z_b}^{z_w} \frac{1}{r} \frac{\partial (r u_r)}{\partial r} dz \\
&= -\left(\frac{1}{r}\frac{\partial}{\partial r}\right) r \int_{z_b}^{z_w} u_r dz \ ,
\end{aligned}
$$

and given the fact that the vertical component of velocity must approximately satisfy the condition of null particle displacement at both bounding surfaces, bottom and free surface, it follows

$$\int_{z_b}^{z_w} u_r \ dz = 0 \ , \tag{A.35}$$

stating that for a 2D flow, any transverse displacement of mass must be absent from the problem. Boussinesq (1868) was the first to solve the aforementioned system, which is treated next, and hereby called "laminar solution" according to Rozovskii (1957).

A.2.3.2 Laminar solution

If the aforementioned system is subjected to the non-slip condition at the channel bottom, and the stress free condition at the free surface, i.e.

$$u_\theta = u_r = 0 \text{ at } z = z_b \ , \quad \frac{\partial u_\theta}{\partial z} = \frac{\partial u_r}{\partial z} = 0 \text{ at } z = z_w \tag{A.36}$$

For a given column of water, its local water depth is a function of r only, i.e., $h = h(r)$. It is convenient then to introduce the following normalized vertical coordinate

$$\zeta = \frac{z - z_b}{h} \ , \quad \zeta = \zeta(r, \theta) \ , \tag{A.37}$$

such that the reduced set (A.33)-(A.34) becomes

$$0 = gS_\theta + \frac{\nu_t}{h^2}\frac{\partial^2 u_\theta}{\partial\zeta^2} \tag{A.38}$$

$$-\frac{u_\theta^2}{r} = -gS_r + \frac{\nu_t}{h^2}\frac{\partial^2 u_r}{\partial\zeta^2} \ , \tag{A.39}$$

with the boundary conditions (b.c.) modified accordingly

$$u_\theta = u_r = 0 \text{ at } \zeta = 0 \ , \quad \frac{\partial u_\theta}{\partial\zeta} = \frac{\partial u_r}{\partial\zeta} = 0 \text{ at } \zeta = 1 \tag{A.40}$$

The equation of motion in $\theta-$direction is easily integrated w.r.t. ζ

$$0 = A + gS_\theta\zeta + \frac{\nu_t}{h^2}\frac{\partial u_\theta}{\partial\zeta}$$

Applying the b.c. at $\zeta = 1$

$$0 = A + gS_\theta + \frac{\nu_t}{h^2}0 \ \rightarrow \ A = -gS_\theta$$

Integrating again

$$0 = B + A\zeta + gS_\theta\frac{\zeta^2}{2} + \frac{\nu_t}{h^2}u_\theta$$

Applying the b. c. at $\zeta = 0$

$$0 = B + A0 + gS_\theta 0 + \frac{\nu_t}{h^2}0 \ \rightarrow \ B = 0$$

The solution is then

$$u_\theta = \lambda\left(2\zeta - \zeta^2\right) \ , \quad \lambda = \frac{gh^2 S_\theta}{2\nu_t} \tag{A.41}$$

The equation of motion in $r-$direction is also easily integrated w.r.t. ζ, since the transverse slope is not a function of ζ. Squaring the solution for u_θ and plugging it into (A.39), i.e., the equation of motion in $r-$direction,

$$gS_r = \frac{\lambda^2}{r}\left(4\zeta^2 - 4\zeta^3 + \zeta^4\right) + \frac{\nu_t}{h^2}\frac{\partial^2 u_r}{\partial\zeta^2} \tag{A.42}$$

Integrating and applying the b.c. at $\zeta = 1$

$$gS_r\zeta + A = \frac{\lambda^2}{r}\left(\frac{4\zeta^3}{3} - \zeta^4 + \frac{\zeta^5}{5}\right) + \frac{\nu_t}{h^2}\frac{\partial u_r}{\partial\zeta}$$

$$gS_r + A = \frac{\lambda^2}{r}\left(\frac{4}{3} - 1 + \frac{1}{5}\right) + \frac{\nu_t}{h^2}0 \ \rightarrow \ A = \frac{8\lambda^2}{15r} - gS_r$$

Integrating again and applying the b.c. at $\zeta = 0$

$$gS_r\frac{\zeta^2}{2} + A\zeta + B = \frac{\lambda^2}{r}\left(\frac{\zeta^4}{3} - \frac{\zeta^5}{5} + \frac{\zeta^6}{30}\right) + \frac{\nu_t}{h^2}u_r$$

$$gS_r0 + A0 + B = \frac{\lambda^2}{r}0 + \frac{\nu_t}{h^2}0 \rightarrow B = 0$$

Finally,

$$u_r = \frac{gS_rh^2}{2\nu_t}\left(\zeta^2 - 2\zeta\right) + \frac{\lambda^2h^2}{r\nu_t}\left(\frac{8\zeta}{15} - \frac{\zeta^4}{3} + \frac{\zeta^5}{5} - \frac{\zeta^6}{30}\right) \tag{A.43}$$

The restriction of zero transverse flux is used now to determine the transverse slope

$$\int_0^1 u_r \, d\zeta = \left[\frac{gS_rh^2}{2\nu_t}\left(\frac{\zeta^3}{3} - \zeta^2\right) + \frac{\lambda^2h^2}{r\nu_t}\left(\frac{4\zeta^2}{15} - \frac{\zeta^5}{15} + \frac{\zeta^6}{30} - \frac{\zeta^7}{210}\right)\right]_0^1$$

$$S_r = \frac{24}{35}\frac{\lambda^2}{rg} \tag{A.44}$$

Plugging this solution into the expression (A.43) for u_r

$$u_r = \frac{\lambda^2h^2}{r\nu_t}\left(-\frac{16}{105}\zeta + \frac{12}{35}\zeta^2 - \frac{1}{3}\zeta^4 + \frac{1}{5}\zeta^5 - \frac{1}{30}\zeta^6\right)$$

$$= \frac{a^4\nu_t}{4r}\left(-\frac{16}{105}\zeta + \frac{12}{35}\zeta^2 - \frac{1}{3}\zeta^4 + \frac{1}{5}\zeta^5 - \frac{1}{30}\zeta^6\right) \tag{A.45}$$

Note that the transverse slope result can be rewritten as

$$S_r = \frac{24}{35}\frac{g^2h^4S_\theta^2}{4gr\nu_t^2} \tag{A.46}$$

$$= \frac{24}{35}\frac{u_*^4h^2}{4gr}\frac{a^2}{u_*^2h^2} = \frac{6a^2u_*^2}{35gr}$$

$$= \frac{6a^2hS_\theta}{35r} = \frac{6a^2hI_\theta}{35r^2} \, , \tag{A.47}$$

where use of (A.18), (A.19), and (A.26) have been made. Then, for a channel with a rectangular cross-section and flat bottom ($z_b = 0$), it follows that $S_r = dh/dr$

$$\frac{dh}{h} = \frac{6a^2I_\theta}{35}\frac{dr}{r^2} \, , \tag{A.48}$$

whose solution is

$$\ln\frac{h}{h_0} = \frac{6a^2I_\theta}{35}\int_{r_0}^r r^{-2}dr = \frac{6a^2I_\theta}{35}\frac{r^{-2+1}}{-2+1}\Big|_{r_0}^r$$

$$\frac{h}{h_0} = e^{\chi\left(1-\frac{r_0}{r}\right)} \, , \quad \chi = \frac{6a^2I_\theta}{35r_0} \simeq \frac{6a^2}{35}\left(-\frac{\Delta z_w}{r_0\Delta\theta}\right) \tag{A.49}$$

A.2.3.3 Engelund solution Modified

From the reduced system proposed by Engelund (1974) (A.38)-(A.39). Assuming the existence of a self-similar solutions, where the balance of forces are locally valid in the center of the channel section, away from the banks

$$\frac{u_\theta}{U} = F(\zeta) \ , \quad \frac{u_r}{U} = \frac{h}{r}(G(\zeta) + J(\zeta)) \quad , \quad S_r = \alpha\frac{U^2}{gr} = \alpha \ \mathrm{Fr}^2\frac{h}{r} \ , \qquad (\text{A.50})$$

where U is a reference velocity, e.g., the longitudinal flow velocity at the free surface, and α is a shape factor very close to unity. The reduced system proposed by Engelund (A.38)-(A.39) becomes

$$0 \ = \ gS_\theta + \frac{\nu_t}{h^2}\frac{\partial^2 u_\theta}{\partial\zeta^2} \ \rightarrow \ 0 = \frac{gS_\theta h^2}{\nu_t U} + F'' \qquad\qquad (\text{A.51})$$

$$-\frac{u_\theta^2}{r} \ = \ -gS_r + \frac{\nu_t}{h^2}\frac{\partial^2 u_r}{\partial\zeta^2} \ \rightarrow \ \alpha - F^2 = \epsilon(G'' + J'') \ , \ J'' = 0 \ , \ \epsilon = \frac{\nu_t}{Uh} \ , (\text{A.52})$$

subject to the following boundary conditions

$$\frac{\rho\nu_t}{h}\frac{\partial u_\theta}{\partial\zeta}\bigg|_{\zeta=0} = \tau_b \ \rightarrow \ F'(0) = \frac{u_*^2 h}{\nu_t U} \ , \ F(1) = 1, \ \ J'(1) = G'(1) = 0 \ , \ \ J'(0) = \frac{u_*^2 h r_*}{a\nu_t U}$$
$$(\text{A.53})$$

which represent the condition that the shear stress must be equal to the bed shear at bed level, u_θ must attain the free stream velocity at the free surface, i.e., $u_\theta = U$, and u_r must be stress-free at the free surface, respectively. Here $a = 13.04$ (Appendix A.2) and $r_* = \frac{U_{R_b}}{U_*}$.

A word of caution is required here since Engelund (1974) set the origin of his reference frame at the free surface, $z' = 0$, positive downwards, i.e., the bottom is at $z' = h$. Consequently, and with reference to Figure A.4, the conversion between both system can be achieved if a point located at position $z = z_b + b$, or $z' = h - b$, is considered. From here, the equality $b = h - z' = z - z_b$ is obtained. It follows

$$-\frac{z'}{h} \ = \ \frac{z - z_b}{h} - 1$$
$$\zeta' \ = \ 1 - \zeta \quad , \quad \zeta' = \frac{z'}{h} \qquad\qquad (\text{A.54})$$

Integrating now the equation of motion in $\theta-$direction, i.e., Eq.(A.50)

$$F' + \frac{u_*^2 h}{\nu_t U}\zeta = A \ \ ,$$
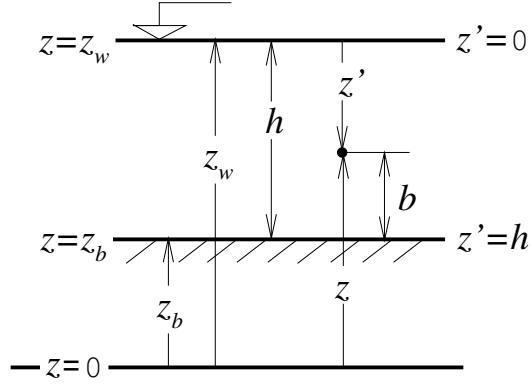
FIGURE A.4: Conversion between Engelund's vertical coordinate and current system.

and after applying the b.c.(A.53), the constant of integration is given by

$$\frac{u_*^2 h}{\nu_t U} = A$$

Integrating the differential equation once again

$$F + \frac{u_*^2 h}{\nu_t U} \frac{\zeta^2}{2} = A\zeta + B \quad ,$$

whereas the b.c. at the free surface provides now the result

$$1 + \frac{u_*^2 h}{2\nu_t U} = \frac{u_*^2 h}{\nu_t U} + B$$

$$B = 1 - \frac{u_*^2 h}{2\nu_t U}$$

Thus

$$F + \frac{u_*^2 h}{\nu_t U} \frac{\zeta^2}{2} = \frac{u_*^2 h}{\nu_t U}\zeta + 1 - \frac{u_*^2 h}{2\nu_t U}$$

$$= \frac{u_*^2 h}{2\nu_t U} (2\zeta - 1) + 1$$

$$F + \frac{u_*^2 h}{2\nu_t U} \left(1 - 2\zeta + \zeta^2\right) = 1 \quad ,$$

and finally

$$F(\zeta) = 1 - \frac{u_*^2 h}{2\nu_t U} (1 - \zeta)^2 \tag{A.55}$$

This solution can be rearranged if Eq.(A.27) is taken into account, with h in place of h_0. Then

$$F(\zeta) = 1 - \beta (1 - \zeta)^2 \quad , \quad \beta = \frac{a\, u_*}{2\, U} \quad , \quad \frac{a}{2} \simeq 6.5 \quad , \tag{A.56}$$

which is the solution given by Engelund (1974) , with $1 - \zeta$ replaced by ζ', as mentioned previously.

Eq.(A.55) represents indeed the velocity defect law. From (A.50), Eq.(A.55) can be rewritten as

$$
\begin{aligned}
\frac{u_\theta}{U} - 1 &= -\frac{u_*^2 h}{2\nu_t U} (1 - \zeta)^2 \\
\frac{u_\theta - U}{U} &= -\frac{u_*^2 h}{2\nu_t U} (1 - \zeta)^2 \\
\frac{U - u_\theta}{u_*} &= \frac{a}{2} (1 - \zeta)^2 \ , \quad a = \frac{u_* h}{\nu_t} \ ,
\end{aligned}
\tag{A.57}
$$

and it can be shown that the value $a = 13.04$ represents the best fit of the parabolic profile to the law of the wall in the upper 90% of the water layer (Vionnet, 2009).

Turning the attention now to the equation of motion in $r-$direction

$$
\begin{aligned}
\epsilon G'' &= \alpha - \left[1 - \beta (1 - \zeta)^2 \right]^2 \\
&= \alpha - 1 + 2\beta (1 - \zeta)^2 - \beta^2 (1 - \zeta)^4
\end{aligned}
$$

Integrating once

$$
\begin{aligned}
\epsilon G' + A &= (\alpha - 1) \zeta + 2\beta \int (1 - \zeta)^2 \, d\zeta - \beta^2 \int (1 - \zeta)^4 \, d\zeta \\
&= (\alpha - 1) \zeta - 2\beta \int t^2 + \beta^2 \int t^4 dt \ , \quad t(\equiv \zeta') = 1 - \zeta \ \rightarrow d\zeta = -dt \\
&= (\alpha - 1) \zeta - 2\beta \frac{t^3}{3} + \beta^2 \frac{t^5}{5} \\
&= (\alpha - 1) \zeta - \frac{2\beta}{3} (1 - \zeta)^3 + \frac{\beta^2}{5} (1 - \zeta)^5
\end{aligned}
$$

The b.c. (A.53) at the free surface yields

$$
\epsilon 0 + A = (\alpha - 1) + 0 + 0 \ \rightarrow \ A = \alpha - 1
$$

Thus

$$
\begin{aligned}
\epsilon G' &= -(\alpha - 1) + (\alpha - 1) \zeta - \frac{2\beta}{3} (1 - \zeta)^3 + \frac{\beta^2}{5} (1 - \zeta)^5 \\
&= -(\alpha - 1)(1 - \zeta) - \frac{2\beta}{3} (1 - \zeta)^3 + \frac{\beta^2}{5} (1 - \zeta)^5
\end{aligned}
\tag{A.58}
$$

Integrating again

$$
\begin{aligned}
\epsilon G + B &= (\alpha - 1) \int t \, dt + \frac{2\beta}{3} \int t^3 \, dt - \frac{\beta^2}{5} \int t^5 \, dt \\
&= (\alpha - 1) \frac{t^2}{2} + \frac{2\beta}{3} \frac{t^4}{4} - \frac{\beta^2}{5} \frac{t^6}{6} \\
&= \frac{(\alpha - 1)}{2} (1 - \zeta)^2 + \frac{\beta}{6} (1 - \zeta)^4 - \frac{\beta^2}{30} (1 - \zeta)^6
\end{aligned}
\tag{A.59}
$$

The constant B is now evaluated after imposing the restriction of zero flux in radial direction, i.e., Eq.(A.35)

$$
\begin{aligned}
\int_{z_b}^{z_w} u_r \, dz &= \frac{1}{h} \frac{hU}{r} \int_0^1 G(\zeta) \, d\zeta = 0 \\
&= -\frac{U}{r} \int_1^0 G(t) \, dt = 0 \\
\int_0^1 G(\zeta) \, d\zeta &= -\int_1^0 G(t) \, dt
\end{aligned}
\tag{A.60}
$$

Consequently,

$$
\begin{aligned}
\epsilon \int_0^1 G \, d\zeta + B &= \frac{(\alpha - 1)}{2} \int_0^1 (1 - \zeta)^2 \, d\zeta + \frac{\beta}{6} \int_0^1 (1 - \zeta)^4 \, d\zeta - \frac{\beta^2}{30} \int_0^1 (1 - \zeta)^6 \, d\zeta \\
0 + B &= -\frac{(\alpha - 1)}{2} \int_1^0 t^2 \, dt - \frac{\beta}{6} \int_1^0 t^4 \, dt + \frac{\beta^2}{30} \int_1^0 t^6 \, dt \\
&= \left. \frac{(1 - \alpha)}{6} t^3 - \frac{\beta}{30} t^5 + \frac{\beta^2}{210} t^7 \right|_1^0 \\
&= \left[0 - \left(\frac{(1 - \alpha)}{6} - \frac{\beta}{30} + \frac{\beta^2}{210} \right) \right] \\
B &= \frac{(\alpha - 1)}{6} + \frac{\beta}{30} - \frac{\beta^2}{210}
\end{aligned}
\tag{A.61}
$$

The radial velocity drift solution is obtained integrating , i.e., Eq.A.52 and after applying the b.c (A.53), finally

$$
J(\zeta) = \frac{2\beta r_*}{a}
\tag{A.62}
$$

The last b.c. used by Engelund (1974) is obtained by considering the influence of a rough bottom. According to Rozovskii (1957) , the condition $S_r = \alpha \frac{U^2}{gr}$ given by (A.50) will not be fulfilled in case of a rough bottom, since from (A.34) the proper balance of

forces acting upon of water column is

$$\frac{1}{h}\int_{z_b}^{z_w} gS_r dz = \frac{1}{h}\int_{z_b}^{z_w}\frac{u_\theta^2}{r}dz + \frac{1}{h}\int_{z_b}^{z_w}\frac{\partial}{\partial z}\left(\nu_t\frac{\partial u_r}{\partial z}\right)dz$$

$$S_r = \frac{1}{gr}\int_{z_b}^{z_w} u_\theta^2\,dz + \frac{1}{\rho gh}\left.\rho\nu_t\frac{\partial u_r}{\partial z}\right|_{z_b}^{z_w}$$

$$S_r = \alpha_0\frac{u_m^2}{gr} - \frac{\tau_{r_0}}{\rho gh}\;, \tag{A.63}$$

where α_0 is a shape factor. Thus, for a rough bottom, the influence of τ_{r_0} can not be neglected. For that case the following b.c. can be used

$$\left.\frac{u_r}{u_\theta}\right|_{z=z_b} = \frac{\rho\nu_t\frac{\partial u_r}{\partial z}\big|_{z=z_b}}{\rho\nu_t\frac{\partial u_\theta}{\partial z}\big|_{z=z_b}} \tag{A.64}$$

In terms of its physical interpretation, the direction of the resistance forces due to the rough bottom acting against the stream must coincide with the direction of bottom velocity (in opposite sense). According to Rozovskii (1957) , this b.c. was originally set forth by Makkaveev (Rozovskii, 1957) , page 49. In terms of the normalized variables given by (A.50), the above b.c. becomes

$$\frac{\frac{Uh}{r}[G(0)+J(0)]}{U\,F(0)} = \frac{\frac{\nu_t}{h}\frac{\partial}{\partial\zeta}\left[\frac{Uh}{r}[G(\zeta)+J(\zeta)]\right]\big|_{\zeta=0}}{u_*^2}$$

$$\frac{G(0)+J(0)}{F(0)} = \frac{\nu_t U}{u_*^2 h}G'(0) = \frac{\nu_t}{u_* h}\frac{U}{u_*}G'(0)$$

$$= \frac{1}{a}\frac{U}{u_*}G'(0)$$

where (A.27) was considered. Now, taken into account (A.56), the above b.c. can be finally written as

$$\frac{G(0)+J(0)}{F(0)} = \frac{1}{2\beta}G'(0)\;,$$

or equivalently

$$\frac{\epsilon[G(0)+J(0)]}{F(0)} = \frac{1}{2\beta}\epsilon G'(0) \tag{A.65}$$

From (A.56), (A.58), and (A.59), the following expressions are easily obtained

$$F(0) = 1-\beta$$

$$\epsilon G'(0) = (1-\alpha) - \frac{2\beta}{3} + \frac{\beta^2}{5}$$

$$\epsilon G(0) = -B + \frac{(\alpha-1)}{2} + \frac{\beta}{6} - \frac{\beta^2}{30}$$

$$J(0) = \frac{2\beta r_*}{a}$$

Consequently, the b.c. (A.65) is now evaluated as

$$2\beta\left(\epsilon[G(0)+J(0)]\right) = F(0)\left(\epsilon G'(0)\right)$$

$$2\beta\left(-B+\frac{(\alpha-1)}{2}+\frac{\beta}{6}-\frac{\beta^2}{30}+\frac{2\beta r_*}{R_e a}\right) = (1-\beta)\left((1-\alpha)-\frac{2\beta}{3}+\frac{\beta^2}{5}\right)$$

$$2\beta\left(-\frac{(\alpha-1)}{6}-\frac{\beta}{30}+\frac{\beta^2}{210}+\frac{(\alpha-1)}{2}+\frac{\beta}{6}-\frac{\beta^2}{30}+\frac{2\beta r_*}{R_e a}\right) = (1-\beta)\left((1-\alpha)-\frac{2\beta}{3}+\frac{\beta^2}{5}\right)$$

$$2\beta\left(\frac{(\alpha-1)}{3}-\frac{\beta}{30}+\frac{\beta^2}{210}+\frac{\beta}{6}-\frac{\beta^2}{30}+\frac{2\beta r_*}{R_e a}\right) = (1-\alpha)(1-\beta)-\frac{1}{5}\beta^3+\frac{13}{15}\beta^2-\frac{2}{3}\beta$$

$$\frac{2\beta}{3}(\alpha-1)-\frac{2}{105}\beta^2(3\beta-14)+\frac{4\beta^2 r_*}{R_e a} = (1-\alpha)(1-\beta)-\frac{1}{5}\beta^3+\frac{13}{15}\beta^2-\frac{2}{3}\beta$$

$$(\alpha-1)\left(1-\frac{1}{3}\beta\right) = \frac{2}{105}\beta^2(3\beta-14)-\frac{1}{5}\beta^3+\frac{13}{15}\beta^2-\frac{4\beta^2 r_*}{R_e a}$$

$$= -\frac{1}{7}\beta^3+\frac{3}{5}\beta^2-\frac{4\beta^2 r_*}{R_e a}-\frac{2}{3}\beta$$

Rearranging

$$\alpha-1 = \frac{-\frac{2}{3}\beta+(\frac{3}{5}-\frac{4r_*}{R_e a})\beta^2-\frac{1}{7}\beta^3}{1-\frac{1}{3}\beta}, \tag{A.66}$$

or

$$\alpha = \frac{1-\beta+(\frac{3}{5}-\frac{4r_*}{R_e a})\beta^2-\frac{1}{7}\beta^3}{1-\frac{1}{3}\beta} \tag{A.67}$$

Eq.(A.67) is actually the result reported by Engelund (1974) except by the factor $\frac{4\beta^2 r_*}{R_e a}$ attributed to the lateral drift $J(\zeta)$. Finally, from (A.4), (A.11) and (A.13), the expression for u_r is

$$\frac{u_r}{U} = \frac{h}{r}\frac{Uh}{\nu_t}\left[-\frac{(\alpha-1)}{6}-\frac{\beta}{30}+\frac{\beta^2}{210}+\frac{(\alpha-1)}{2}(1-\zeta)^2+\frac{\beta}{6}(1-\zeta)^4-\frac{\beta^2}{30}(1-\zeta)^6\right], \tag{A.68}$$

where the expression ϵG has been multiplied by $\epsilon^{-1}=Uh/\nu_t$.

Finally, the coefficient β is related the Chezy resistance coefficient, since from (A.21)

$$u_m = \frac{1}{h}\int_{z_b}^{z_w} u_\theta dz = U\int_0^1 F(\zeta)d\zeta$$

$$= U\int_0^1\left[1-\beta(1-\zeta)^2\right]d\zeta$$

$$c_Z u_* = U(1-\frac{1}{3}\beta),$$

and from the definition of β given by (A.56)

$$c_Z = \frac{6.5\left(1-\frac{1}{3}\beta\right)}{\beta}, \tag{A.69}$$

which is the expression posted by Engelund (1974) , albeit with a misprint (the factor 1/3 is missing). Alternatively, it is better to express the above result in terms of the Chezy coefficient

$$\beta = \frac{1}{\frac{1}{3} + \frac{c_z}{6.5}} \tag{A.70}$$

A.2.4 Engelund slip-velocity method

Ignoring the bed mobility effects existing in any alluvial stream, the bottom of an open-channel behaves as a generating drag boundary that slows down the overlaying flow, thus creating a velocity defect from the "outer velocity" V. Expressing the constant eddy solution of Engelund given by (2.20) in the form

$$\frac{V - U_\theta^0}{U_*^0} = \frac{a}{2} \left(1 - \zeta\right)^2 , \tag{A.71}$$

obtained after invoking (2.10) for $R_0/R \simeq 1$ and replacing β from (2.15), it is thus questionable whether the foregoing velocity defect expression can achieve a good fitting, in the least square sense, with the most widely accepted law of the wall

$$\frac{V - U_\theta^0}{U_*^0} = -2.5 \ln \zeta . \tag{A.72}$$

Consequently, forming the following functional with a as free parameter

$$J(a) = \int\limits_\lambda^1 \left[\frac{a}{2} \left(1 - \zeta\right)^2 - \left(-2.5 \ln \zeta\right) \right]^2 d\zeta , \tag{A.73}$$

the stationarity condition with respect to a, $dJ/da = 0$, leads to the result

$$\begin{aligned} a &= \frac{-5 \int\limits_\lambda^1 \left[(1 - \zeta)^2 \ln \zeta \right] d\zeta}{\int\limits_\lambda^1 (1 - \zeta)^4 d\zeta} \\ &= \frac{-5 \left\{ -\frac{11}{18} + \frac{\left[(1 - \lambda)^3 - 1 \right]}{3} \ln \lambda + \lambda - \frac{\lambda^2}{2} + \frac{\lambda^3}{9} \right\}}{\frac{(1 - \lambda)^5}{5}} \end{aligned} \tag{A.74}$$

Picking arbitrary values for λ (e.g. $\lambda = 0.05$ value fits the upper 95% of the profile), the values listed in Table A.1 are obtained . Therefore, for the value of a corresponding to $\lambda = 0.1$ the slip-velocity at the channel bed $U_\theta^0(Z_b) = v(0)V$ seems to satisfy the following scaling in (A.71).

TABLE A.1: Values of a and the corresponding eddy viscosity magnitude.

λ	0.100	0.050	0.010
a	13.040	13.567	14.605
ϵ_0	$0.077 U_*^0 H_0$	$0.074 U_*^0 H_0$	$0.068 U_*^0 H_0$

$$\frac{V - U_\theta^0(Z_b)}{U_*^0} \simeq 6.5 \tag{A.75}$$

Inferring now V from the logarithmic law of the wall, the following expression to estimate $U_\theta^0(Z_b)$ is obtained (Engelund, 1974; Johannesson and Parker, 1989b)

$$\begin{aligned} r_* &= \frac{U_\theta^0(Z_b)}{U_*^0} \\ &= 2. + 2.5 \ln\left(\frac{H_0}{K_s}\right), \end{aligned} \tag{A.76}$$

where K_s is a typical bed roughness height that characterizes the contribution from skin and bedform resistance. Thus, a constant eddy viscosity model of $\epsilon_0 \simeq 0.077 U_*^0 H_0$ means that the parabolic profile (A.71) fits the upper 90% of the log-law profile.

Finally, it is relevant to relate r_* with the Chezy coefficient, defined by (2.26) and usually estimated with the aid of the Keulegan recommendation (Parker, 2004)

$$C_z = 2.5 \ln\left(\frac{11 H_0}{K_s}\right). \tag{A.77}$$

Thus, combining (A.76) with (A.77) yields r_*

$$r_* = C_z - 4, \tag{A.78}$$

which is the expression used to compute the modified helicoidal flow component $u(\zeta)$ depicted in Figure 2.2.a and the total lateral component $j(\zeta) + u(\zeta)$ plot in Figure 2.2.b.

A.2.5 Flow round a flat plate

The conjugate complex velocity $u - iw$ representing the flow in the $z = x + i\varsigma$ plane round a flat plate of length $4c$, with centre at the origin, and exposed to an inclined free-stream (u_∞, w_∞) with circulation γ (counter-clockwise positive), is

$$u - iw = u_\infty - i\left(w_\infty z + \frac{\gamma}{2\pi}\right)\left(z^2 - 4c^2\right)^{-1/2}, \tag{A.79}$$

where i is the imaginary unit. Then, the uniqueness of $\left(z^2 - 4c^2\right)^{-1/2}$ is achieved by specifying a "cut" along $|x| \leq 2c$ corresponding either to the physical barrier presented

by a plate, or to the velocity discontinuity through a vortex sheet of size $4c$ and strength γ.

As simple as it is to represent the stream function and the velocity field in terms of the conformal transformation to elliptical-coordinates (Batchelor, 1967), it is extremely tedious to do so in Cartesian coordinates. Nonetheless, after some algebra, it is possible to express the velocity field in terms of Cartesian coordinates (x, ς) as (Vionnet, 2011)

$$
\begin{aligned}
u &= u_\infty + \left[w_\infty \left[\varsigma f(x, \varsigma) - x h(x, \varsigma) \right] - \frac{\gamma}{2\pi} h(x, \varsigma) \right] \frac{1}{d(x, \varsigma)}, \\
w &= \left[w_\infty \left[x f(x, \varsigma) + \varsigma h(x, \varsigma) \right] + \frac{\gamma}{2\pi} f(x, \varsigma) \right] \frac{1}{d(x, \varsigma)},
\end{aligned}
\tag{A.80}
$$

where the function h, f and d are defined in (2.40) and (2.41). The limiting case $(u_\infty, w_\infty) = (0, 0)$ and $\gamma \neq 0$ is commonly cited in the literature. Then, it is possible to see that the functions f, h and d reduce, when $\varsigma = 0, |x| \leq 2c$, to

$$
d = (4c^2 - x^2) \;,\;\; f = 0 \;,\;\; h = sgn(\varsigma)\sqrt{4c^2 - x^2},
\tag{A.81}
$$

such that the flow velocity on the upper and lower sides of the vortex sheet has equal magnitude but opposite sign

$$
u|_{\varsigma = \pm 0} = -\frac{sgn(\varsigma)\gamma}{\pi\sqrt{4c^2 - x^2}} \;,\;\; w = 0 \;,\;\; |x| \leq 2c.
\tag{A.82}
$$

It is always possible to pick the value of γ to remove the singularity at either one of the points $z = \pm 2c$ (Batchelor, 1967). However, the composition of the 1D downstream flow velocity with the 2D cross-circular flow, in turn transported by the 1D component, can deliver the sought helical behaviour (see Figure 2.4.b) if the grid used for computing (A.80) avoid the singular points.

Appendix B

Independent computation of river discharge

If the vessel path encloses a region Ω of boundary $\partial\Omega$, characterized by the unit tangent vector $\mathbf{t} = (t_x, t_y) \equiv (\delta x/\delta s, \delta y/\delta s)$ and the negative unit normal vector $\mathbf{n}^- = (-\delta y/\delta s, \delta x/\delta s)$, obtained through a 90° counterclockwise rotation from $\mathbf{t}$, where the positive direction of $\mathbf{t}$ points in the direction of increasing arc-length (s^+) when the path is traversed in the counterclockwise direction (such that the interior of the enclosed region Ω is on the left), a simple relation for the mass continuity can be derived. In the absence of any sources or sinks, the mass conservation constraint for a shallow-water flow of depth-averaged horizontal velocity $\mathbf{U} = (U, V)$ and water layer thickness H reads $\nabla \cdot H\mathbf{U} = 0$, which can be converted into a line integral along four pieces of the boundary $\partial\Omega$: one across the channel going from left to right bank (which provides the sought discharge Q), two along both river banks (equal to zero due to the non-flux condition), and the final one across the channel in reversed direction (equal to $-Q$), i.e.

$$Q = \int_0^B (H\mathbf{U}) \cdot \mathbf{n}^+ \, ds \simeq \sum_{j=1}^n F_j \, \overline{\Delta s_j} \,, \qquad (B.1)$$

where n refers to the number of ensembles or vertical profiles measured by the ADCP along the polyline (transect) of length B (not necessary equal to the channel width), Δs_j the separation distance between the j-th and $j+1$-th ensembles (or profiles) and

$$F_j = (UH \, t_y - VH \, t_x)_j \quad , \quad \overline{\Delta s_j} = (\Delta s_{j-1} + \Delta s_j)/2 \quad , \quad j = 1, \ldots, n \qquad (B.2)$$

Above, Δs_0 and Δs_n are the specified user distance from both river banks to the first and last measured ensemble respectively, and $\mathbf{U} \cdot \mathbf{n}^+ = U_n$ represents the outward normal of the depth-averaged flow component (Figure B.1(a)).

The ADCP setup divides each water column into n_b depth cells, variable along the transect according to the local water depth. In turn, the ADCP determines the magnitude and direction of the flow velocity at each depth cell, whose geographical coordinates ENU equates with the local planar and vertical (x, y, z) coordinates. Therefore, if (u, v, w) are the local planar and vertical velocity components estimated by the ADCP at the barycentric point (x, y, z) of each depth cell, the 2DH flow velocity components adopted here at every ensemble along the transect are

$$U = \frac{\sum_{i=1}^{n_b} u_i}{n_b + 1} \quad , \quad V = \frac{\sum_{i=1}^{n_b} v_i}{n_b + 1} \; , \tag{B.3}$$

which results from imposing the no-slip condition at the river bed. Moreover, the use of the equation (B.3) in (B.2) implicitly assumes that the upper layer of unmeasured water (due to blanking distance and transducer draft) and the bottom layer moves with the mean velocity $\mathbf{U} = (U, V)$ (Figure B.1(a)). The trapezoid rule for approximating the definite integral (B.1) amounts to estimate the lateral unmeasured portions of the cross-section as $Q_{left} = F_1 \Delta s_0 / 2$ and $Q_{right} = F_n \Delta s_n / 2$ (Figure B.1(b)).
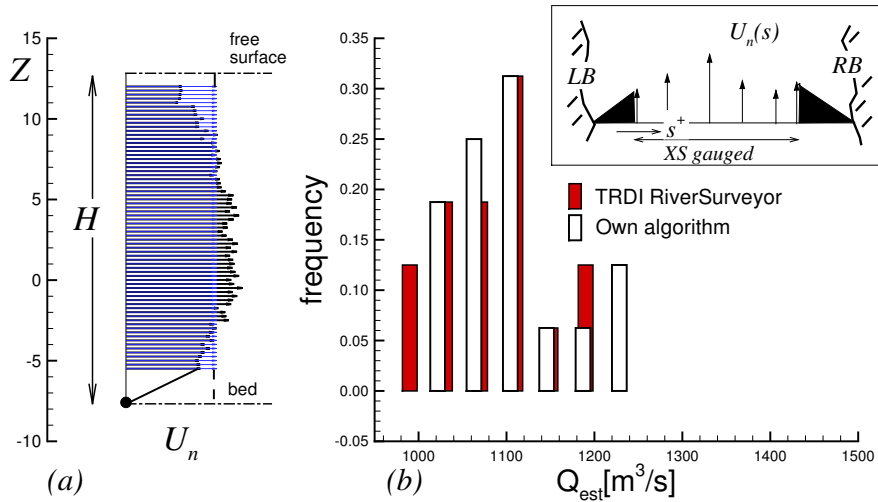
FIGURE B.1: River discharge as computed by *read_aDcp*. a) variable arrows: actual velocity measurements, constant arrows: mean velocity according to equation (B.3) projected in normal direction, b) frequency distribution computed by the proprietary software and by the in-house user interface.

It must be clear that the procedures implemented in the in-house code to approximate the surface-nearest and bed-nearest velocity values within an ADCP profile, and the discharge values near the river banks as well, differ greatly from the one-sixth power-law and the ratio interpolation methods embedded in the proprietary software (Simpson, 2001; Sontek, 2004; TRDI, 2007). Nevertheless, Figure B.1(b) shows that the river discharge values computed with *read_aDcp* and with the proprietary ADCP software compare favourably well as explained in the text.

In any real-time data collection situation, the differential distance traversed by the boat in the elapsed time δt_j is $\delta s_j = V_b \delta t_j$, where V_b is the mean vessel velocity in the time period δt_j. Consequently, the above expression for the river discharge can be rearranged into the scalar triple product

$$Q = \int_0^{T(B)} (\mathbf{U}H \times \mathbf{t}V_b) \cdot \mathbf{k} \, dt \, , \tag{B.4}$$

where $\mathbf{k}$ is the unit vector in the upward direction, t the time, and $T(B)$ the elapsed time required to traverse the transect path along the cross-section. A similar equation comprises the moving-vessel methodology for measuring total discharge using an ADCP (Simpson, 2001; TRDI, 2007). Here, the expression (B.1) is used instead to verify if the actual cross-section data were surveyed from the left bank to the right bank ($Q < 0$), or vice-versa ($Q > 0$).For the latter case, the ADCP surveyed data is reversed, so both left and right banks are correctly located when observing data from upstream to downstream as it is customary in fluvial hydraulics. In the meantime, equation (B.1) also provides an independent estimate of the river discharge.

Appendix C

The Rozovskii method as rotation coordinates

If the Rozovskii method is treated as a strict rotation, some considerations must be taken into account:

- the vector $\mathbf{U_m}$ (2DH) is not necessarily $\perp$ to the XS, i.e, in most situations $\phi \neq \theta + \pi/2$,

- the resultant transformation matrix rotates in counterclockwise direction (θ instead of $-\theta$, (Strang, 1988, p. 122)),

- however, it is possible to see that Eq.(2.46) implied a negative definited cross-velocity, i.e., $V_s < 0$,

- to correct that deficiency, and with reference to Figure C.1, it is posible to set a positive defined V_s in the sense of Rozovskii if $\mathbf{U}$ is projected in directions $\perp$ and $\parallel$ to $\mathbf{U_m}$, or equilently, in directions (s, p), respectively

$$
\begin{aligned}
V_s &= |\mathbf{U}|sin(\phi - \varphi)\,, \\
V_p &= |\mathbf{U}|cos(\phi - \varphi),
\end{aligned}
$$

or equilently,

$$
\begin{aligned}
V_s &= |\mathbf{U}|(sin\phi\,cos\varphi - cos\phi\,sin\varphi)\,, &\text{(C.1)} \\
V_p &= |\mathbf{U}|(cos\phi\,cos\varphi + sin\phi\,sin\varphi). &\text{(C.2)}
\end{aligned}
$$

FIGURE C.1: Rozovskii rotation direction $\perp$ (*s*) and $\parallel$ (*p*) to $\mathbf{U_m}$.

On the other hand, and from Figure C.1

$$
\begin{aligned}
U_x &= |\mathbf{U}|cos\phi = |\mathbf{U}|cos(\delta + \pi/2), \\
U_y &= |\mathbf{U}|sin\phi = |\mathbf{U}|sin(\delta + \pi/2),
\end{aligned}
$$

or equilently,

$$
\begin{aligned}
U_x &= -|\mathbf{U}|sin\delta(< 0), & \text{(C.3)} \\
U_y &= |\mathbf{U}|cos\delta(> 0), & \text{(C.4)}
\end{aligned}
$$

which leads to

$$
\left[\begin{array}{c} V_s \\ V_p \end{array} \right] = \left[\begin{array}{cc} sin\phi & -cos\phi \\ cos\phi & sin\phi \end{array} \right] \left[\begin{array}{c} U_x \\ U_y \end{array} \right]. \tag{C.5}
$$

- The first equation, $V_s = sin\phi\, U_x - cos\phi\, U_y$, **is** exactly Eq.(2.47) of this Thesis.

- Seeing now this whole thing as a rotation, and for the extreme case where $\phi = \theta + \pi/2$, the above matrix defines a rotation in **clockwise** sense, because $sin\phi = sin(\theta + \pi/2) = cos\theta$ and $cos\phi = cos(\theta + \pi/2) = -sin\theta$. This is,

$$
\left[\begin{array}{cc} sin\phi & -cos\phi \\ cos\phi & sin\phi \end{array} \right] \rightarrow \left[\begin{array}{cc} cos\theta & sin\theta \\ -sin\theta & cos\theta \end{array} \right]. \tag{C.6}
$$

which is a matrix that sends the basis vectors $(0,1)$ and $(1,0)$ to $(s\theta, c\theta)$ and $(c\theta, -s\theta)$, respectively (Strang, 1988, p. 122)), interpreted with respect to the base $(0,1)$ and $(1,0)$). However, if the Rozovskii transformation is taken as new coordinates, the transformation maps (x, y) into (s, p) as intended.

Note:

$$
V_s = \left[\begin{array}{l} |\mathbf{U}|sin(\phi - \varphi) > 0 \\ |\mathbf{U}|sin(\varphi - \widehat{\phi}) < 0 \end{array} \right. \tag{C.7}
$$

Bibliography

Amsler, M. A., C. G. Ramonell, and H. A. Toniolo (2005). Morphologic changes in the paraná river channel (argentina) in the light of the climate variability during the 20th century. *Geomorphology 70*, 257–278.

Ashworth, P. L., S. J. Bennet, J. L. Best, and S. J. McLelland (1996). *Coherent Flow Structures in Open Channels*. Chichester, England: Wiley and Sons Ltd. ISBN:0-471-95723-2.

Babuska, I. and W. C. Rheinboldt (1978). Error estimates for adaptive finite element computations. *SIAM J. on Numerical Analysis 15*(4), 735–754.

Batchelor, G. K. (1967). *An Introduction to Fluid Dynamics*. London: Cambridge University Press.

Bathurst, J. C., C. R. Thorne, and R. D. Hey (1977). Direct measurements of secondary currents in river bends. *Nature 269*(5628), 504–506.

Bathurst, J. C., C. R. Thorne, and R. D. Hey (1979). Secondary flow and shear stress at river bends. *J. Hydraul. Div. 105*(10), 1277–1295.

Best, J. L. and A. G. Roy (1991). Mixing layer distortion at the confluence of channels of different depth. *Nature 350*(6317), 411–413.

Blanckaert, K. and H. J. de Vriend (2003). Nonlinear modeling of mean flow redistribution in curved open channels. *Water Resources Res. 39*(12), 1375–1388.

Blanckaert, K. and H. J. de Vriend (2004). Secondary flow in sharp open-channel bends. *J. Fluid Mech. 498*, 353–380.

Blanckaert, K. and W. H. Graf (2004). Momentum transport in sharp open-channel bends. *J. Hydr. Engrg. 130*(3), 186–198.

Blanckaert, K., I. Schnauder, A. Sukhodolov, W. van Balen, and W. Uijttewaal (2009). Meandering: Field experiments, laboratory experiments and numerical modeling. *RCEM2009*, 863–875. Vionnet et al. (eds), Taylor & Francis Group, London.

Boussinesq, J. (1868). Mémoire sur l´influence du frottement dans les mouvements réguliers des fluids. *Journal de Mathématiques Pures et Appliquées 2e série 13*, 377–424.

Boxall, J. B., I. Guymer, and A. Marion (2003). Transverse mixing in sinuous natural open channel flows. *J. Hydraul. Res. 41*(2), 153–165.

Brownlie, W. R. (1981). Prediction of flow depth and sediment discharge in open channels. Report KH-R-43A, W. M. Keck Laboratory of Hydraulics and Water Resources, California Institute of Technology, Pasadena, California, USA.

Burge, L. M. (2006). Stability, morphology and surface grain size patterns of channel bifurcation in gravel-cobble bedded anabranching rivers. *Earth Surf. Process. Landforms 31*, 1211–1226.

Carrasco, A. and C. A. Vionnet (2004). Separation of scales on a broad, shallow turbulent flow. *J. Hydraul. Res. 42*(6), 630–638.

Chant, R. (2002). Secondary circulation in a region of flow curvature: Relationship with tidal forcing and river discharge. *Journal of Geophysical Research 107*(C9), 3131.

Corney, R., J. Peakall, D. Parsons, L. Elliott, K. Amos, J. Best, G. Keevil, and D. Ingham (2006). The orientation of helical flow in curved channels. *Sedimentology 53*, 249–257.

Coz, J. L., M. Michalkov, A. Hauet, M. Comaj, G. Dramais, K. Holubov, H. Pigay, and A. Paquier (2010). Morphodynamics of the exit of a cutoff meander: experimental findings from field and laboratory studies. *Earth Surf. Processes Landforms 35*.

Cuadrado, D. G. and M. E. Perillo (1997). Principal component analysis applied to geomorphologic evolution. *Estuarine, Coastal and Science 44*(4), 411–419.

Daniels, M. D. and B. L. Rhoads (2006). Influence of experimental removal of large woody debris on spatial patterns of three-dimensional flow in a meander bend. *Earth Surface Processes and Landforms 32*, 460474.

Dargahi, B. (2004). Three-dimensional flow modelling and sediment transport in the River Klaralven. *Earth Surf. Process. Landforms 29*, 821–852.

de Vriend, H. and H. Geldof (1983). Main flow velocity in short river bends. *J. Hydraul. Engrg. 109*(7), 991–1011.

de Vriend, H. J. (1981). Velocity distribution in curved rectangular channels. *J. Fluid Mech. 107*, 423–439.

Dietrich, W. E. and J. D. Smith (1983). Influence of the point bar on flow through curved channels. *Water Resources Res. 19*, 1173–1192.

Dinehart, R. L. and J. R. Burau (2005). Averaged indicators of secondary flow in repeated acoustic doppler current profiler crossings of bends. *Water Resources Res. 41.* (W09405, doi:10.1029/2005WR004050).

Drago, E. and M. L. Amsler (1988). Suspended sediment at a cross section of the Middle Paraná River: concentration, granulometry and influence of the main tributaries. In M. P. Bordas and D. E. Walling (Eds.), *Sediment Budgets*, Proc. Symposium held at Porto Alegre, Brazil, 11-15 Dec 1988, pp. 381–396. IAHS Press, Inst. of Hydrology, Wallingford.

Engelund, F. (1974). Flow and bed topography in channel bends. *J. Hydraul. Engrg. 100*(11), 1631–1648.

Falcon, M. (1984). Secondary flow in curved open channels. *Ann. Rev. Fluid Mech. 16*, 179–193.

Federici, B. and C. Paola (2003). Dynamics of channel bifurcations in noncohesive sediments. *Water Resour. Res. 39*(6), 1162–1176. doi:10.1029/2002WR001434.

FICH (1998). Análisis preliminar de alternativas de ubicación de posibles terminales complementarias del Puerto de Santa Fe. Final Rep., Comisión Administr. Prov. Ente Puerto de Santa Fe, FICH-UNL, Santa Fe, Argentina.

Hall, P. (1975). The stability of unsteady cylinder flows. *J. Fluid Mech. 67*, 29–63.

Hervouet, J. M. (2007). *Hydrodynamic of free surface flows. Modelling with the finite element method.* St. Anthony Falls Lab., Univ. Minnesota: John Wiley & Sons, Ltd.

Hickin, E. J. (1978). Mean flow structure in meanders of the Squamish River, British Columbia. *Can. J. Earth Sci. 15*, 1833–1849.

Hooke, R. L. (1980). Shear-stress distribution in stable channel bends. *J. Hydraul. Eng 106*(7), 1271–1272. (Discussion).

Iriondo, M. H. (2007). Chapter 2: Geomorphology. In M. H. Iriondo, J. C. Paggi, and M. J. Parma (Eds.), *The Middle Paraná River: Limnology of a Subtropical Wetland*, pp. 33–52. Berlin Heidelberg: Springer-Verlag.

Jackson, P. R. (2013). Visualizing flow fields using acoustic doppler current profilers and the velocity mapping toolbox. Fact sheet 2013-3028, U.S. Geological Survey, llinois Water Science Center, USA. http://pubs.usgs.gov/fs/2013/3028/.

Jackson, P. R., P. Oberg, N. Gardiner, and J. Shelton (2009). Velocity mapping in the lower Congo River: a first look at the unique bathymetry and hydrodynamics of Bulu Reach, West Central Africa. In C. A. Vionnet et al. (Eds.), *River, Coastal and Estuarine Morphodynamics 2009*, pp. 1007–1014. London: Taylor and Francis Group.

Johannesson, H. and G. Parker (1989a). Linear theory of river meanders. In S. Ikeda and G. Parker (Eds.), *River Meandering*, pp. 181–214. Water Resources Monograph, 12: AGU.

Johannesson, H. and G. Parker (1989b). Secondary flow in mildly sinuous channel. *J. Hydraul. Eng. 115*(3), 289–308.

Kashyap, S., G. Constantinescu, C. D. Rennie, G. Post, and R. Townsend (2012). Influence of channel aspect ratio and curvature on flow, secondary circulation, and bed shear stress in a rectangular channel bend. *J. Hydraul. Eng. 138*, 1045–1059.

Kikkawa, H., A. Kitagawa, and S. Ikeda (1976). Flow and bed topography in curved open channels. *J. of the Hydraulics Division 102*(9), 1327–1342.

Kitanidis, P. K. and J. F. Kennedy (1984). Secondary currents and river-meandering formation. *J. Fluid Mech. 144*, 217–229.

Kleinhans, M. G., H. R. A. Jagers, E. Mosselman, and C. J. Sloff (2008). Bifurcation dynamics and avulsion duration in meandering rivers by one-dimensional and three-dimensional models. *Water Resour. Res. 44*(W08454). doi:10.1029/2007WR005912.

Lane, S. N., K. F. Bradbrook, K. S. Richards, P. M. Biron, and A. G. Roy (1999). Time-averaged flow structure in the central region of a stream confluence: a discussion. *Earth Surf. Process. Landforms 24*, 361–367. (Short communication).

Lane, S. N., K. F. Bradbrook, K. S. Richards, P. M. Biron, and A. G. Roy (2000). Secondary circulation cells in river channel confluence: measurement artefacts or coherent flow structures. *Hydrolog. Process. 14*, 2047–2071.

Leschziner, M. A. and W. Rodi (1979). Calculations of strongly curved open channel flow. *J. Hydraul. Engrg. 105*(10), 1297–1314.

Lievens, A. (1997). The River Plate experience; Maintenance dredging by means of privatisation. *Terra et Aqua 68*(Sept 97), 3–10.

Lloyd, P. and P. Stansby (1997). Shallow-water flow around model conical islands of small side slope. ii: Submerged. *J. Hydraul. Eng. 123*(12), 1068–1077.

Miori, S., R. J. Hardy, and S. N. Lane (2012). Topographic forcing on flow partition and flow structures at river bifurcations. *Earth Surf. Process. Landforms 37*, 669–679.

Morell, M. I., C. A. Vionnet, and P. Tassi (2014). Flow pattern at a river diffluence at the alluvial system of the Paraná River. *Journal of Applied Water Engineering and Research 2*(2), 140–156.

Mourad, F. (2011). personal communication.

Muste, M., K. Yu, and M. Spasojevic (2004). Practical aspects of adcp data use for quantification of mean flow characteristics. part i: moving-vessel measurements. *Flow Meas. Instrum. 15*, 1–16.

Oberg, K. and D. Mueller (2007). Validation of streamflow measurements made with acoustic doppler current profilers. *J. Hydraul. Eng. 133*(12), 1421–1432.

Parker, G. (2004). *1D Sediment Transport Morphodynamics of Rivers and Turbidity Currents.* St. Anthony Falls Lab., Univ. Minnesota: NCED - National Center for Earth-suface Dynamics. ebook; http://vtchl.uiuc.edu/people/parkerg.

Parsons, D. R., J. L. Best, S. N. Lane, O. Orfeo, and R. J. Hardy (2007). Form roughness and the absence of secondary flow in a large confluence-diffluence, río paraná, argentina. *Earth Surf. Processes Landforms 32*, 155–162.

Parsons, D. R., P. R. Jackson, J. A. Czuba, F. L. Engel, B. L. Rhoads, K. A. Oberg, J. L. Best, D. S. Mueller, K. K. Johnson, and J. D. Riley (2013). Velocity mapping toolbox (VMT): a processing and visualization suite for moving-vessel adcp measurements. *Earth Surf. Processes Landforms 38*, 1244–1260.

Pittaluga, M. B., R. Repetto, and M. Tubino (2003). Channel bifurcation in braided rivers: Equilibrium configurations and stability. *Water Resour. Res. 39*(3). doi:10.1029/2001WR001112.

Ramonell, C. (2012). Evaluación de procesos hidro-geomorfológicos del Río Paraná entre los ejes del Arroyo Leyes y Santa Fe-Paraná. Final Rep. Sectei 21-18-10, FICH-UNL, Santa Fe State Gov., Argentina.

Rhoads, B. L. and S. T. Kenworthy (1998a). Time-averaged flow structure in the central region of a stream confluence. *Earth Surf. Process. Landforms 23*, 171–191.

Rhoads, B. L. and S. T. Kenworthy (1998b). Time-averaged flow structure in the central region of a stream confluence. *Earth Surf. Processes Landforms 23*, 171–191.

Rhoads, B. L. and S. T. Kenworthy (1999). On secondary circulation, helical motion and rozovskii-based analysis of time-averaged two-dimensional velocity fields at confluences. *Earth Surf. Process. Landforms 24*, 369–375. (Short communication).

Rhoads, B. L. and A. N. Sukhodolov (2001). Field investigation of three-dimensional flow structure at stream confluences. *wrr 37*, 2393–2410.

Richardson, W. R. and C. R. Thorne (2001). Multiple thread flow and channel bifurcation in a braided river: Brahmaputra-jamuna river, bangladesh. *Geomorphology 38*, 185–196.

Rozovskii, I. L. (1957). Flow of water in bends of open channels (in russian).

Shiono, K., Y. Muto, D. W. Knight, and A. Hyde (1999). Energy losses due to secondary flow and turbulence in meandering channels with overbank flows. *J. Hydraul. Res. 37*(5), 641–663.

Simpson, M. R. (2001). Discharge measurements using a broad-band acoustic doppler current profiler. Open-File Report 01-1 1395, USGS, Sacramento, CA, USA.

SMS (2000). *Surface Modelling system, Users Manual*. Utha, USA.

Snyder, J. (1987). Map projections - a working manual. Profess. Paper 1395, USGS, Washington DC 20402, USA.

Snyder, J. P. (1926). Map projections - a working manual. Professional paper 1395, U.S.G.S., Washington DC 20402.

Sontek (2004). RiverSurveyor System Manual. Software version 4.10, SonTek YSI Inc, San Diego, CA, USA.

Strang, G. (1988). *Linear Algebra and Its Applications* (3rd ed.). Orlando, Florida, USA: Harcourt Brace Jovanovich Inc.

Straub, K. M., D. Mohrig, B. M. Elroy, J. Buttles, and C. Pirmez (2008). Interactions between turbidity currents and topography in aggrading sinuous submarine channels: A laboratory study. *Geological Society of America (bulletin) 12*(3/4), 368–385.

Sukhodolov, A. N. (2012). Structure of turbulent flow in a meander bend of a lowland river. *Water Resour. Res. 48*.

Szupiany, R. N., M. L. Amsler, J. L. Best, and D. R. Parsons (2007). Comparison of fixed- and moving-bessel flow measurements with an adp in a large river. *J. Hydraul. Engrg. 133*(12), 1299–1309.

Szupiany, R. N., M. L. Amsler, D. R. Parsons, and J. L. Best (2009). Morphology, flow structure, and suspended bed sediment transport at two large braid-bar confluences. *wrr 45*.

Tecplot (2011). *Users Manual for Tecplot 360TM Version 2011*. WA, USA.

Telemac-Mascaret Modelling System (2014). Webpage.

Thomson, J. (1876). On the origin of winding rivers in alluvial plains. *Proceedings of the Royal Society 25*, 5–8.

TRDI (2007). WinRiver II. Users Guide, Teledyne RD Instruments, Poway, CA, USA.

Vionnet, C. (2010). River bed topography; interpolation of scatter data. Internal report 01-2010, CENEHA, FICH, UNL, Santa Fe, Argentina.

Vionnet, C. A. (1995). Numerical investigation of the sealing capacity of centrifugal instabilities in shaft seals. *Int. J. Heat and Fluid Flow 16*, 254–262.

Vionnet, C. A. (2009). Quick guide to fundamentals of turbulence in open-channel flows, with an overwiew on 1d sediment transport. Int Report 0109, CENEHA-FICH, U.N.L., Santa Fe, Argentina.

Vionnet, C. A. (2011). Flow in open-channel bends. Internal Rep. 01-2011, Centre for Water and Enviromental Studies - CENEHA, FICH-UNL, Santa Fe, Argentina.

Vionnet, C. A., P. A. Tassi, and J. P. Martin-Vide (2004). Estimates of flow resistance and eddy viscosity coefficients for 2D modelling on vegetated floodplains. *Hydrol. Process. 18*, 2907–2926.

Vionnet, C. A., P. A. Tassi, L. B. Rodríguez, and C. G. Ferreira (2006). Numerical modelling of the catastrophic flooding of Santa Fe City, Argentina. *Int. J. River Basin Management 4*(4), 301–314.

Yalin, M. S. (1992). River mechanics.

Zinger, J. A., B. L. Rhoads, J. L. Best, and K. K. Johnson (2013). Flow structure and channel morphodynamics of meander bend chute cutoffs: A case study of the wabash river, USA. *J. Geophys. Res. Earth Surf. 118*(4), 24682487.

Doctorado en Ingeniería
mención recursos hídricos

Título de la obra:
**On the Rozovskii method
to isolate secondary circulation
from skewed flow**

Autor: Mariana Inés Morell

Lugar: Santa Fe, Argentina

Palabras Claves:

Secondary currents
Rozovskii method
Hydrodynamic diffluence
Telemac-3d
Flows bend